ALL-IN-ONE, MULTIFUNCTIONAL, IMPLANTABLE FIBER-SHAPED BLOOD GAS SENSOR

ZHIZHI WU

MPhil

The Hong Kong Polytechnic University

2025

The Hong Kong Polytechnic University

Department of Applied Biology and Chemical Technology

All-in-one, Multifunctional, Implantable Fiber-shaped Blood Gas Sensor

Zhizhi Wu

A thesis submitted in partial fulfilment of the requirements for the degree of Master of Philosophy

January 2025

CERTIFICATE OF ORIGINALITY

I hereby declare that this thesis is my own work and that, to the best of my knowledge and belief, it reproduces no material previously published or written, nor material that has been accepted for the award of any other degree or diploma, except where due acknowledgement has been made in the text.

_____ (Signed)

Zhizhi Wu_____ (Name of student)

Abstract

During the past decades, the number of surgeries has seen a dramatic increase, from around 187.2 million cases in 2004 to 312.9 cases undertaken in 2012. The dynamic and rapid fluctuations in patients' physiological status underscore the imperative need for real-time monitoring devices capable of providing prompt and accurate feedback on changes in patient conditions. Implantable devices have garnered significant attention in recent years due to their capacity to give continuous[1] and real-time physiological monitoring, enabling the assessment of various vital parameters, including arterial blood pressure and blood gas analysis via arterial lines, intracranial pressure via intracranial pressure monitors, and deep vein thrombosis. The widespread adoption of implantable monitoring devices has not only met the existing clinical demands but also driven the development of more advanced implantable monitoring technologies, fostering a self-reinforcing cycle of innovation and clinical need. However, several limitations often hinder existing implantable monitoring devices, including the need for high patient compliance, compromised stability[2-4], and sensitivity, which can compromise their overall performance and clinical utility.

Patient non-compliance and complex medical interventions can compromise the functionality of implantable monitoring devices. Fiber-shaped devices, inspired by arterial lines, offer a promising solution due to their minimal interface and high stability[5, 6]. However, ensuring these devices' structural and signal stability during implantation in flexible tissues and organs is crucial to obtaining accurate and reliable data. Researchers have succeeded in fiber-shaped transistors for electrochemical sensing, fiber-based strain sensors, and fiber-based capacitive sensors. However, achieving a balance between stability, biocompatibility, and multifunctionality remains a significant challenge in developing implantable monitoring devices.

Here, we introduce a novel, multi-functional electrochemical fiber-shaped blood sensor, denoted as TIEFS (transducer-interlayer-EGaIn fiber sensor), featuring a simple design. The sensor exhibits high sensitivity towards sodium ions, with a detection limit of 147 mV/decade due to the incorporation of a capacitive interlayer comprising polytetrafluoroethylene/perfluoropolyether/multi-walled carbon nanotubes (PTFE/PFPE/CNTs) that enhances the detected signal through improved capacitance. Notably, the fiber's three separate conductive channels enable the simultaneous detection of sodium and potassium concentrations without significant electrical crosstalk. The TIEFS demonstrates stable sensing performance under various conditions, including bending and soaking in solution for 7 days, and exhibits a high resolution of 100 μm for potassium detection, as well as a low signal drift of 0.9678 mV/h. Furthermore, we successfully demonstrated the feasibility of implantation by testing the sensor's performance in detecting sodium and potassium concentrations in Sprague-Dawley (SD) rats and human blood. The TIEFS is promising for clinical applications due to its simple fabrication process and high stability, making it a potential candidate for future biomedical applications.

Acknowledgment

First of all, I would like to express my most incredible gratitude to my supervisor, Professor Zijian Zheng, for giving me the opportunity to pursue an MPhil degree at PolyU. Meanwhile, I would like to thank his wise guidance and support during this research project. His knowledge, wisdom, and patience highly helped me become a better MPhil student. Prof. Zheng was always enthusiastic and generous whenever I asked for help on this project.

In addition, I would like to thank all the group members for their kindness and support. They are Dr. Qiyao Huang, Dr. Xian Song, Dr. Chi Zhang, Dr. Yichun Ding, Dr. Sze Wing, Miya, Ng, Dr. Yufeng Luo, Dr. Yanpeng Guo, Dr. Yingsi Wu, Dr. Junhua Zhou, Dr. Huimin Wang, Dr. Jingjing Fu, Dr. Yufei Zhang, Dr. Youchao Qi, Dr. Yongqiang Yang, Dr. Hanyi Nan, Dr. Lulu Zu, Dr. Can Guo, Dr. Xinyan Li, Dr. Leni Zhong, Dr. Fan Chen, Dr. Wancheng Yu, Dr. Hengyi Li, Dr. Wenli Jiao, Dr. Yueying Zhuang, Mr. Zijian Chen, Miss Jiehua Cai, Mr. Lingtao Fang, Miss Yuqing Shi, Mr. Xiaohao Ma, Miss Shujing Wen, Mr. Lixi Chen, Mr. Jinxing Jiang, Mr. Jiaheng Liang, Miss Huiming Wang, Mr. Zhibo Li.

I would also like to thank the technical help from the Department of Applied Biology and Chemical Technology, UMF-Materials Research Centre, University Research Facility in 3D Printing, and Guangdong Provincial People's Hospital. Finally, the financial support from the Hong Kong Polytechnic University is well acknowledged.

Table of Contents

Abstract **3**

Ac**knowledgment** **5**

Table of Contents **6**

List of Figures **8**

List of Tables **14**

List of Abbreviations **15**

Chapter 1 Introduction **16**

1.1 Background and Challenges 16

1.2 Research Objectives 18

1.3 Significance and Values 18

1.4 Outline of the Report 19

Chapter 2 Literature Review **21**

2.1 Blood Gas Analysis 21

2.1.1 History of Blood Gas Analysis 21

2.1.2 Commercial Equipment 22

2.1.3 Analytes in Blood Gas Analysis 24

2.2 Implantable Biosensors 25

2.2.1 Device Structure and Working Mechanism of Electrochemical Biosensors 25

2.2.2 Material Requirement of Implantable Biosensors 27

2.2.3 Conductive Materials 35

2.3 Fiber-Shaped Biosensors 45

2.3.1 Working Mechanism of Biosensors 45

2.3.2 Planar and Fiber-shaped Biosensors 46

2.3.3 Fabrication Methods of Fiber-shaped Biosensors 49

Chapter 3 Methodology **53**

3.1 Materials 53

3.2 Fabrication 54

3.2.1 Fabrication of Multi-Channel Conductive Fiber 54
3.2.2 Fabrication of Three-Electrode Fiber 55
3.2.3 Fabrication of Sensing Electrodes 56
3.3 Characterization 58
Chapter 4 Fabrication and Characterization of EGaIn-Filled Fiber (EFiber) 59
4.1 Morphology of Hollow Fiber 59
4.2 Mechanical Properties of Hollow Fiber 60
4.3 Electrical Property of EFiber 62
Chapter 5 Fabrication and Characterization of Multifunctional Implantable Fiber-shaped Sensor 64
5.1 Structure of Fiber-shaped Sensor 64
5.1.1 Overview of Fiber-shaped Sensor 64
5.1.2 Transducer Layer 65
5.1.3 Interlayer 69
5.2 Capacitive Performance of Transducer-Interlayer-EGaIn Fiber (TIEFiber) 75
5.3 Sensing Performance of Fiber-shaped Sensor (TIEFS) 79
5.4 Multi-functional Fiber-shaped Sensor (TIEFS) 86
Chapter 6 Conclusion 95
References 97

List of Figures

Figure 2.1.1 The development of commercial blood gas analyzers (BGA)……..22

Figure 2.2.1 A schematic of a biosensor with electrochemical transducer…….27

Figure 2.2.2 The stages of inflammation that occur after implantation of a medical device/biosensor……...……28

Figure 2.2.3 Photographs of (A-E) fabrication process and morphology of SNR. (F) Representative SEM image of SCs cultured on T-SNR films for 3 d.…….……29

Figure 2.2.4 Structure of (A) PLA; (B) PGA; (C) PLGA; (D) PCL…….30

Figure 2.2.5 (A) A scheme of PLA-based pH sensor for hypoxia monitoring; (B) The synthesis process and working mechanism of PLA-PGA sensor via cold plasma surface modification. (C) The PCL-based, transparent, flexible dopamine biosensor……..31

Figure 2.2.6 Structure of (A) Polydimethylsiloxane; (B) Phenyl polysiloxane; (C) Vinyl polysiloxane; (D) Fluoropolysiloxane……32

Figure 2.2.7 (A) An implanted wireless sensor for restenosis detection. (B) A stented artery during restenosis progression and the resulting change of arterial wall strain…….33

Figure 2.2.8 Structure of (A) PEVA; (B) PU……33

Figure 2.2.9 The comparison between the PU-based glucose sensor and commercial device……...…34

Figure 2.2.10 (A) Schematic illustration of the microvascular flow measurement system. (B) Sensing components in a flow probe……...……...…35

Figure 2.2.11 Schematic representation of Au microneedles-based glucose biosensor37

Figure 2.2.12 (A) Scheme of the implantable antenna utilizing Titanium Nitrate. (B) Measured link budget analysis of implanted antenna in vivo. (C) Scheme of Ag deposition. (D) SEM images of AgNPs ……38

Figure 2.2.13 (A) The comparison of Young's modulus between liquid metals and other materials. (B) The relationship between conductivity at maximum strain and strain. (C) The liquid metal is proven to be able to stretch to 600% strain…….40

Figure 2.2.14 (A) Scheme and fabrication method of μLME. (B) Resistance of μLMEs of various linewidths at different tensile strains. (C) Spatiotemporal properties for the μLME array. ……..…….……...……41

Figure 2.2.15 Structures of fullerene, CNTs, and graphene……..……42

Figure 2.2.16 (A) Scheme of the wireless blood pressure sensor. (B) The relationship between impedance change and blood pressure. (C) The change of impedance gained with time varied.……...43

Figure 2.2.17 Diagram of (A) single-walled CNTs (SWCNTs); (B) multi-walled CNTs (MWCNTs); CNT configurations of (C) zigzag; (D) armchair; (E) chiral……44

Figure 2.2.18 (A) The scheme of CNTs-based implantable biosensors (SSFs) with multiple monitoring functionalities. (B) The in vivo glucose sensing performance of the SSFs implanted in rats……...……45

Figure 2.3.1 (A) Schematic representation of an electrochemical biosensor. (B) Component of biosensors…..……46

Figure 2.3.2 (A) The schematic view of the OECT biosensor. (B) Fluorescence images of coronal brain slices with implanted fiber-shaped OECTs for 7 d and the control group without implants……...48

Figure 2.3.3 (A) The experimental photos and (B) FEA results of MWP at the distance of 0 mm, 6 mm, and 12 mm stretch……..……49

Figure 2.3.4 Schematic illustration of wet-spinning process……50

Figure 2.3.5 (A) The fabrication process and morphology of the TPU strain fiber sensor. (B) The effect of heat treatment on the structure of the TPU fiber. (C) The electrical conductivity under heat treatment for 30 minutes under different temperatures……...51

Figure 3.2.1 Optical images of Noztek XCalibur Filament Extruder……54

Figure 3.2.2 The schematic illustration of the hot extrusion process……54

Figure 3.2.3 Schematic and composition of TIEFS. Insert at the right is a cross-sectional schematic view of TIEFS……...58

Figure 4.1.1 (A) Three-channel hollow TPU fibers with diameters from 2 mm to 150 μm. (B) Cross-sectional view of three-channel fiber. (C) Optical image of three-channel fiber..…...…….59
Figure 4.2.1 (A) Stress-strain comparison between hollow fibers made of TPU, SEBS, and solid fibers made of SEBS. (B) Stress-strain loop of SEBS. (C) Stress-strain loop of TPU (D) Young's modulus comparison of the bear hollow fiber (Fiber), the bear three-channel fiber with one channel filled with liquid metal (EFiber), transducer-EGaIn fiber (TEFiber), and transducer-interlayer-EGaIn fiber (TIEFiber).…….60
Figure 4.3.1 (A) Conductivity of the hollow TPU fiber under stretching to 700%. The end of the test for the test fixture is off, and the length of the wires is limited. (B) Zoomed-in image of the conductivity of the hollow TPU fiber under stretching to 125%. (C) The conductivity change under more than 2000 times of 6-fold elongation, hundreds of times of 7.5-fold elongation, and 500 times of 9.5-fold elongation……...63
Figure 5.1.1 (A) The structure of TIEFS. (B) The cross-sectional view of TIEFS. (C) The overview of three electrodes on TIEFS……..65
Figure 5.1.2 The three-dimensional conductive network. Blue lines on the left and the right circles indicate the carboxylated multi-walled carbon nanotubes. The gray rounds indicate liquid metal EGaIn……..66
Figure 5.1.3 (A) The optical image of PLA/CNTs composite membrane. (B) The effect of the weight ratio of CNTs on the resistance. (C) The difference in hole diameter and the ratio of the distance from the hole to the edge of the membrane to the hole diameter among different weight ratios of CNTs, referred to as the 'hole-to-edge ratio difference '. (D) The resistance change under stretching of the TEFiber with different weight ratios of CNTs. 2:1, 4:1, 6:1, and 10:1 refer to the weight ratio of PLA to CNTs. ….…..……67
Figure 5.1.4 The sodium sensing performance of TEFS with different weight ratios of CNTs. 2:1, 4:1, 6:1, and 10:1 refer to the weight ratio of PLA to CNTs……69
Figure 5.1.5 (A) The morphology comparison of the interlayer, transducer, and the combination of interlayer with transducer. (B) Zoomed-in morphology of interlayer. (C)

Zoomed-in morphology of transducer. (D) Zoomed-in morphology of interlayer + transducer.……..……...……70

Figure 5.1.6 The bending test of TEFS. (A, C) Morphology of TEFS before bending. (B, D) Morphology of TEFS after bending……...71

Figure 5.1.7 The bending test of TIEFS. (A, C) Morphology of TIEFS before bending. (B, D) Morphology of TIEFS after bending……..72

Figure 5.1.8 (A) The morphology of TEFS before scratching. (B) The morphology of TEFS after scratching with #5000 to # 80 sandpapers. (C) The morphology of TIEFS before scratching. (D) The morphology of TIEFS after scratching with #5000 to # 80 sandpapers……..……..73

Figure 5.1.9 (A) The tensile strength of fiber, EFiber, TEFiber, and TIEFiber. (B) The resistance changes of ETFiber, TEFiber, and TIEFiber under bending and elongation. (C) The change of resistance of EFiber, TEFS, and TIEFS under bending. (D) The change of resistance of TEFS and TIEFS under scratching.……..74

Figure 5.1.10 The contact angle between water and (A) interlayer; (B) transducer without interlayer; (C) transducer with interlayer. …….……..75

Figure 5.2.1 (A) The electrical circuit of TEFS (up) and TIEFS (down). R_{LM}: the resistance of liquid metal. R_{Tr}: the resistance of the transducer. R_{ISM}: the resistance of ion selective membrane. R_{CT}: the resistance of charge transfer. C_{EDL}: the capacitance of the electrical double layer. R_{Int}: the resistance of interlayer. C_{Int}: the capacitance of interlayer. (B) The CV curve of TEFiber and TIEFiber. (C) Nyquist plot of the electrical circuit of TIEFiber. (D) The Bode magnitude and phase angle plot of the electrical circuit of TIEFiber. .…….…….76

Figure 5.2.2 (A) The capacitance of TIEFiber with different masses of CNTs. (B) The capacitance value of IEFiber and TIEFiber. (C) The sensitivity of sodium TIEFS with different masses of CNTs.……78

Figure 5.3.1 (A) The sensitivity of sodium TIEFS to sodium concentration ranged from 120 mM to 160 mM. (B) Corresponding calibration plot of sodium TIEFS……..79

Figure 5.3.2 (A) The resolution of sodium TIEFS to sodium concentration ranged from 120 mM to 122 mM. (B) The corresponding calibration plot of sodium TIEFS. (C) The resolution of potassium TIEFS to potassium concentration ranged from 5 mM to 5.4 mM. (D) The corresponding calibration plot of potassium TIEFS. ……...…80

Figure 5.3.3 (A) The sodium sensor sensitivity of recent works. 1: our work. 2: ***Sci. Rep.,*** 2024, **14,** 11526. 3: ***Electroanalysis,*** 2019, **31,** 239-245. 4: ***Sens. Actuators B Chem.,*** 2021, **331,** 129416. 5: ***Nat. Electron.,*** 2022, **5,** 694–705. 6: ***Anal. Chem.,*** 2020, **92,** 4647-4655.7: ***ACS Appl. Mater. Inter.,*** 2017, **9**, 35169-35177. (B) The selectivity of sodium TIEFS. (C) The sensitivity of glucose TIEFS to glucose concentration ranged from 0 μM to 250 μM. (D) Corresponding calibration plot of glucose TIEFS……...81

Figure 5.3.4 (A) The repeatability of sodium TIEFS to sodium concentration ranged from 122.5 mM to 132.5 mM. (B) The reproductivity of sodium TIEFS to sodium concentration ranged from 120 mM to 140 mM……82

Figure 5.3.5 (A) The sensitivity of sodium TIEFS under bending to sodium concentration ranged from 120 mM to 140 mM. (B) The sensing performance of sodium TIEFS before and after 10, 50, and 100 bending times.……84

Figure 5.3.6 (A) The long-term sensing stability of sodium TIEFS and TEFS for 120 mM sodium aqueous solution in 15h. (B) The long-term sensing performance of sodium TIEFS before and after 3 and 7 days of soaking into sodium solution to sodium concentration ranged from 80 mM to 180 mM.……85

Figure 5.3.7 Sensor performance of recent works. CCF: ***Electroanalysis,*** 2016, *28*, 1267-1275. Na-ISE: ***ACS Sens***. 2020, 5, 2834–2842. AU-NMs: ***Anal. Chem.*** 2019, 91, 6569–6576. PPVN: ***Chem. Eng. J.*** 2023, 454, 140473. Weaved: ***Adv. Funct. Mater.*** 2018, 28, 1804456. CSSY: ***Adv. Funct. Mater,*** 2022, 32, 2200922. SWCNT: ***Electroanalysis*** 2023. 35. e202200121. NCGP: ***Anal. Chem.*** 2021, 93, 16222–16230……....86

Figure 5.4.1 (A) The sensitivity of sodium TIEFS under bending to sodium concentration ranged from 120 mM to 140 mM. (B) The impedance change between the reference electrode and the working electrode with different 'interelectrode

distances ', which refers to the distance between the two electrodes of sodium TIEFS. (C) The simultaneous sensing to sodium and potassium aqueous solution of TIEFS...88

Figure 5.4.2 (A) The H&E stain of the implanted area of SD rats after 7 days of implantation. Insert image shows the area before implantation. (B) The MTT test of TIEFS. (C) The hemolysis assay of TIEFS. (H) The histological evaluation of SD rats' tissue after 7 days of implantation.…….....90

Figure 5.4.3 Multi-functional TIEFS is implanted into SD rats for sodium and potassium sensing..……...…….....91

Figure 5.4.3 (A) Long-term simultaneous sensing of sodium TIEFS and potassium TIEFS in mice blood. (B) The simultaneous sensing of sodium and potassium to rats' blood of TIEFS. (C) Corresponding calibration plot of TIEFS. (D) The sensing results in 9 different samples of human blood of TIEFS and commercial devices.....93

List of Tables

Table 2.1.1 Current commercial blood gas analysis equipment……..23

Table 2.1.2 List of main indicators and their normal range in blood gas analysis…..25

Table 2.2.1 Heterogeneous electron transfer rate constant (k_0), real electroactive area (AEA), and roughness factor (ρ) of the gold planar electrode and the gold microneedles-based electrode before and after the electrodeposition of h-PG and Au-MWCNTs…36

Table 3.2.1 The weight value of different components for the interlayer……....55

Table 3.2.2 The weight value of PLA and CNT for transducer solution……..56

Table 5.4.1 The sensing result of sodium and potassium from multi-functional TIEFS and commercial equipment……...95

List of Abbreviations

TIEFS: transducer-interlayer-EGaIn fiber sensor

TEFS: transducer-EGaIn fiber sensor

TIEFiber: transducer-interlayer-EGaIn fiber

TEFiber: transducer-EGaIn fiber

EFiber: EGaIn-filled fiber

TPU: Thermoplastic urethane

PLA: Polylactic acid

PTFE: Polytetrafluoroethylene

PFPE: Perfluoropolyether

Chapter 1 Introduction

1.1 Background and Challenges

The pursuit of advanced diagnosis devices always stands in the front of biomedical innovation, especially in critical care[7] and surgical monitoring[8]. Monitoring blood content (such as oxygen, carbon dioxide, sodium, glucose, and pH) matters significantly in analyzing a patient's respiratory and metabolic functionality[9]. Traditionally, blood gas analysis is performed through arterial blood sampling, a process that, despite its accuracy, is invasive, intermittent, and often stressful for the patient[10]. This method's inherent limitations underscore the urgent need for alternative approaches that offer continuous, real-time monitoring capabilities.

The booming emergence of flexible wearable devices in recent years has marked a significant shift in the landscape of patient monitoring. These devices, which range from surface patches[11] to implantable sensors[12], promise a new era of healthcare where continuous monitoring outside the clinical setting is feasible and practical. However, the application of such technologies to blood gas monitoring, especially in an implantable format, still needs to be explored. This gap is particularly pronounced in surgical and critical care environments, where real-time blood gas analysis could dramatically enhance patient management and outcomes.

The critical importance of real-time monitoring in blood gas analysis stems from the dynamic nature of the human body's respiratory and metabolic processes for the rapid fluctuation of parameters in response to physiological changes, medical interventions, or the onset of complications[13]. In surgical settings, the ability to monitor these changes in real-time could provide clinicians with invaluable insights, enabling timely adjustments to ventilation, oxygen therapy, and other critical interventions. Similarly,

in critical care, continuous blood gas monitoring could facilitate the early detection of adverse events, guiding interventions to prevent the escalation of patient conditions.

Despite the apparent demand for innovative solutions, developing implantable sensors for multiplexed blood gas monitoring faces significant challenges. Current research in fiber-shaped electrochemical biosensors has primarily focused on single-analyte detection, with limited exploration into multifunctional designs. This focus has resulted in a scarcity of solutions capable of addressing the multifaceted requirements of blood gas analysis, including the simultaneous monitoring of multiple indicators, long-term stability in the physiological environment, and minimal invasiveness.

The challenge is further compounded by the stringent performance criteria for biosensors, which must exhibit high selectivity, sensitivity, and rapid response times for each analyte[14]. Additionally, the biosensors must be biocompatible, flexible, and durable enough to withstand the physiological conditions within the body over extended periods[5]. Achieving these criteria necessitates a multidisciplinary approach, combining advances in materials science, nanotechnology, and electrochemical sensing techniques. Developing novel materials and fabrication methods capable of integrating multiple sensing elements within a single fiber is crucial. These materials must facilitate the selective detection of each target gas and ensure the sensor's overall structural integrity and performance.

In conclusion, developing fiber-shaped implantable electrochemical biosensors for blood gas monitoring represents a challenging medical technology frontier. Addressing this application's complex demands requires technical innovation and a deep understanding of the physiological context in which these sensors will operate. Success in this endeavor has the potential to revolutionize patient monitoring in critical care and surgical settings, offering a new level of insight into patient physiology and significantly improving clinical outcomes.

1.2 Research Objectives

To address the abovementioned problems, this project aims to develop a multifunctional and implantable fiber-shaped sensor to monitor the real-time fluctuation in blood. The following are the detailed objectives of this project:

i) To develop fiber-shaped sensing electrodes with multi-channel configuration through a continuous spinning strategy,

ii) To assemble the multifunctional fiber-shaped biosensors by utilizing the multi-channel fiber-shaped sensing electrodes,

iii) To study the electrochemical and mechanical properties of the fiber-shaped biosensors,

iv) To investigate the implantability of the fiber-shaped biosensors and evaluate their applications in blood gas sensing.

1.3 Significance and Values

To date, the realm of implantable blood monitoring devices is witnessing a meteoric rise, positioning themselves as the avant-garde in the domains of flexible electronics and healthcare innovation. The advent of fiber-shaped, multifunctional blood monitoring sensors heralds a new era, promising to revolutionize how medical practitioners can swiftly and conveniently assess the physiological status of their patients. This groundbreaking technology facilitates the immediate and efficacious evaluation and intervention of patient conditions, thereby forestalling any potential worsening of their health status.

Moreover, the single fiber design of these devices significantly minimizes the wound, a pivotal advancement in medical procedures. The inherent flexibility of these biosensors markedly diminishes the risk of inflicting damage on adjacent tissues during the implantation process. This attribute enhances the overall safety and comfort of patient care and plays a crucial role in expediting the healing process.

In essence, the development of these fiber-shaped, multifunctional blood gas monitoring sensors is a testament to the strides in medical technology. It underscores a commitment to improving patient outcomes by integrating innovative, less invasive, and more efficient healthcare solutions. As such, these devices stand at the forefront of a transformative movement in patient care, embodying the pinnacle of medical ingenuity and the promise of a healthier future.

1.4 Outline of the Report

The report is organized as follows:

Chapter 1 introduces the background and challenges of the research. The research objectives are demonstrated as well.

Chapter 2 gives a comprehensive review of fiber-shaped implantable blood monitoring devices. Firstly, the blood gas analysis is introduced, followed by the emerging implantable biosensors, which include the requirement for implantation and the sensing mechanisms. Finally, the fiber-shaped implantable biosensors are briefly introduced.

Chapter 3 covers the materials, fabrication methods, instruments, and characterization techniques used in the research.

Chapter 4 and Chapter 5 presents the results and discussions of the research work, including the morphology and electrical properties of multi-channel fiber conductors and electrodes, electrical and mechanical performance of the fiber-shaped biosensor.

Chapter 6 elucidates the conclusion of the work and the perspectives for future research and application of fiber-shaped sensors.

Chapter 2 Literature Review

This part mainly focuses on the overview of blood gas analysis and the current status of research on implantable biosensors, especially fiber-based biosensors for blood monitoring.

2.1 Blood Gas Analysis

2.1.1 History of Blood Gas Analysis

Hippocrates, the great founder of Western medicine, indicated that good health resided in a proper balance, including blood, which relies on generating life-giving heat within the left ventricl[15]. This hypothesis gives the foundation of blood analysis. Until 1956[16], after the wreak havoc of poliomyelitis, doctors in Copenhagen realized the importance of blood monitoring in the care of critically ill patients. Since the mid-1960s, most intensive care institutions have had locally placed equipment for fast blood gas analysis. Doctors usually extract blood samples from the indwelling arterial tube and bring them to the analysis laboratory, load the samples onto the device, and read out the results printed out from the analysis device[17]. This method is regarded as the most convenient and reliable analysis tool in intense care and surgeries, though the sample transport requires a hurry and cautious conduction. Therefore, blood gas analysis seems to be the most prevalent diagnostic tool in surgical care[18].

Doctors can obtain various information, including cardiac condition and acid-base status, from arterial, jugular, and mixed venous samples.[9, 19]. Understanding and using blood gas analysis enables medical personnel to explain respiratory, circulatory, and metabolic disorders. Arterial blood gas analysis is often prescribed by clinicians in

emergency medicine, intensive care, anesthesiology, and pulmonary medicine and may also be used in other clinical Settings[20].

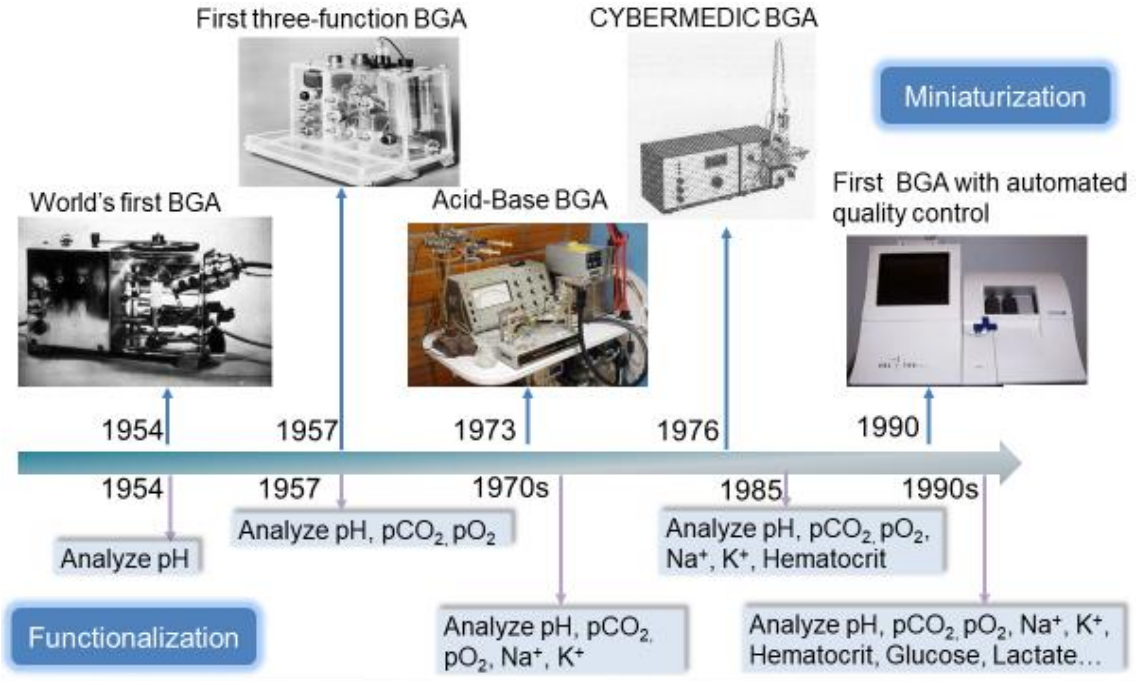

Figure 2.1.1 The development of commercial blood gas analyzers (BGA).

2.1.2 Commercial Equipment

A blood gas analyzer (BGA) is a prevalent tool for doctors to analyze the whole-body status of patients. It is significant to obtain immediate laboratory results from BGA for doctors to take fast and accurate interventions for patients.[21]. The blood gas analyzer (BGA) measures not only blood gas but also electrolytes and metabolites such as glucose and lactic acid and adds total hemoglobin or hemocytometer, providing vital information for clinicians to diagnose various metabolic and respiratory diseases to speed up the diagnosis of emergencies and follow-up treatment[22-26]. The current commercial blood gas analysis equipment and its performance are listed in Table 1. Most of the bulk equipment is not used for real-time analysis, which prolongs the turnaround time and leads to fragmentation of analysis. As a result, patient samples are often measured using different analytical methods and different types of equipment,

and clinicians usually use reported results interchangeably without being aware of potential pitfalls. For example, the ABL Flex 90 is declared to produce a lower lactate concentration result than the actual value[27]. The relatively long turnaround time would also increase the inaccuracy of analysis. Premier™ 5000, a kind of new system[28], tends to report wrong analysis results with the presence of blood clots.

Brands	**Real-time or not**	**Reaction time**	**Sensitivity (e.g., Na^+)**
RAPIDLab® 1200 **Siemens**	N	1 min	1 mmol
Cobas b 123 **Roche**	N	2 min	1 mmol
i-STAT **Abbott**	Y	2 min	1 mmol
ABL800 FLEX **Radiometer**	N	1 min	1 mmol
XP300 **Sysmex**	N	1 min	1 mmol
GEM Premier 5000 **Werfen**	N	Several mins	/
DC101 **Wondfo Biotech**	N	1 min	1 mmol

Table 2.1.0-1 Current commercial blood gas analysis equipment.

Numerous studies consider the effect of the BGA in prehospital emergency medicine. For example, Prause[29] et al. utilized AVL OPTI CC to study lactate analysis for acidosis detection. They concluded that lactate measuring is an effective indicator of acidosis, which provides valuable information. Schober[30] utilized i-STAT in helicopter emergency medical service (HEMS) and proved that the i-STAT is feasible in the HEMS setting. An association between BGA abnormities at the start of CPR and worse clinical outcomes is proven to existence[31]. However, the portable i-STAT shows high and unpredictable gaps between end-tidal and arterial CO_2 values among anesthetized

and intubated people[32]. Even worse, the i-STAT only works among a few patients with chronic obstructive pulmonary disease who received a telemedical treat-and-release strategy with respiratory insufficiency[33].To summarize, though providing great convenience, the commercial BCA still faces challenges, such as being easily affected by the method and time of sample collection and the testing temperature[34].

2.1.3 Analytes in Blood Gas Analysis

BGA involves measuring and calculating the partial pressure of solutions, hematological parameters, and associated gases in electrolytes in a patient's blood sample. BGA can measure different indicators, including information related to gas like partial pressure of oxygen and carbon dioxide, pH, metabolic, and electrolytes such as potassium and sodium[13, 35, 36]. BGA can not only analyze arterial blood but also venous and capillary blood. However, different parameters and reference ranges must be considered when using venous blood to treat BGA[37].

The values of the indicators are closely related. The human body's regulation of hydrogen ion concentration is affected by the respiratory system and the metabolic system[38]. For example, when the concentration of CO_2 increases in blood by the respiratory system, the water in plasma (H_2O) dissociates to H^+ and hydroxide ions (OH^-).

An acceptable normal range of ABG values and electrolytes is the following[39, 40]. What is worth noting is that the range of normal values may vary among different age groups in different districts with various genes.

Indicator	**Normal Range**
pH	7.35 - 7.45

PaO_2	75 - 100 mm Hg
$PaCO_2$	35 - 45 mm Hg
HCO_3	22 - 26 mEq/L
Base excess/deficit	-4 to +2
SaO_2	95 - 100%
Na^+	135 - 145mmol/L
K^+	3.5 - 5.5mmol/L
Glucose	4.4 - 6.1mmol/L
Lactate	0.5 - 1.7 mmol/L

Table 2.1.2 List of main indicators and their normal range in blood gas analysis[39, 40].

2.2 Implantable Biosensors

2.2.1 Device Structure and Working Mechanism of Electrochemical Biosensors

Sensors register a physical, chemical, or biological change and convert that into a measurable signal[41]. In biosensing, extracting information from biological systems by measuring electrical properties is predominantly electrochemical. Although biosensing devices incorporate various identifying elements, electrochemical detection techniques mainly rely on enzymes due to their specific binding capabilities and biocatalytic activities[42-44]. Other biometric elements include antibodies, nucleic acids, cells, and microorganisms. Immunosensors, for instance, use antibodies, antibody fragments, or antigens to detect binding events in bioelectrochemical reactions[44, 45].

In biological electrochemistry, the reactions under study typically result in a measurable current (amperometry), a measurable potential or charge accumulation (potentiometry), or a detectable change in the conductive properties of the medium between electrodes (conductance method). Additional electrochemical detection techniques include the

impedance method, which measures impedance (resistance and reactance)[46, 47], and the field effect method, which employs transistor technology to measure the current generated by the gate potential effect.

Since reactions are generally detectable only near the electrode surface, the electrode's characteristics are crucial to the performance of electrochemical biosensors. The electrode's material, surface finish, and size significantly influence its detection capabilities. Electrochemical tests often consist of a reference electrode, a counter electrode, and a working electrode. The reference electrode is working as a stable potential. The counter electrode provides a stable current when necessary. The working electrode detects the change of potential or current from the reaction area. These electrodes must be electrically conductive and stable. Depending on the analyte, common materials used for electrodes include platinum, gold, carbon (such as graphite), and silicon compounds[48, 49].

To understand how a biosensor works, one must consider the principles of electrochemical measurement. The biosensor detects changes in electrical properties, which are then translated into readable signals. Graphical representations often illustrate the relationship between the electrical signal and the concentration of the analyte, providing a visual understanding of the sensor's performance.

The working principle of a biosensor involves several key steps (Figure 2.2.1):
Biological sensing element: The biological recognition element (e.g., enzyme, antibody) interacts specifically with the target analyte.
Transducer: This interaction causes a change in the electrical properties, such as current, potential, or impedance.
Signal Processing: The transducer converts this change into an electrical signal.
Output: The signal is processed and displayed, often as a graph or digital readout.

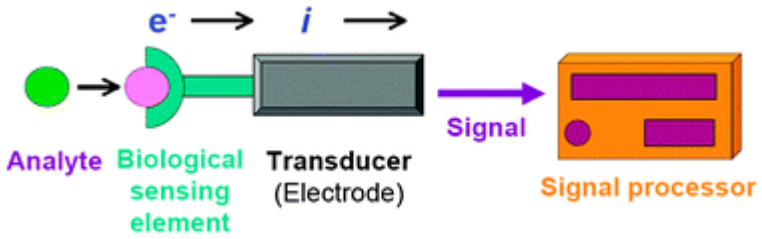

Figure 2.2.1 schematic of a biosensor with an electrochemical transducer[50].

2.2.2 Material Requirement of Implantable Biosensors

The booming prosperity of biosensors comes from the glucose biosensor based on an oxygen electrode created by Leland Clark in 1962[51]. This ingenious creativity was based on the Clark oxygen electrode developed in 1959. The enzyme-based oxygen electrode obtained high selectivity due to the highly distinctive binding with reaction substrates.

Compared with other monitoring devices, biosensors have many advantages, like monitoring the metabolites and electrical signals and helping the body recover. Furthermore, some kinds of implantable devices are prone to deliver drugs inside the body[52]. Different from ex vivo biosensors, there are some requirements and challenges for implantable biosensors since live tissues and organs in vivo surround them. The most significant challenge is to increase the flexibility of devices until they are fit for the suppleness of the surrounding tissues or organs. The mechanical mismatch would not only easily damage the surrounding tissues and exert additional tension[53, 54] but also cause friction inside the devices, thus decreasing device service life, stability, and functionality of devices[55-57]. Therefore, to suppress the mechanical damage caused by implantable devices, flexible matrices like polyimide, polyethylene terephthalate, and polyethylene naphthalateis[58] are highly required to replace the rigid silicon[59].

The biocompatibility of materials is also of paramount significance, which includes two parts: the biological functionality (whether the device would perform well inside the

body or not[60]) and the biosafety (whether the device would cause additional tissue reaction, inflammation, cancer, cytotoxicity, necrosis or not[61, 62]).

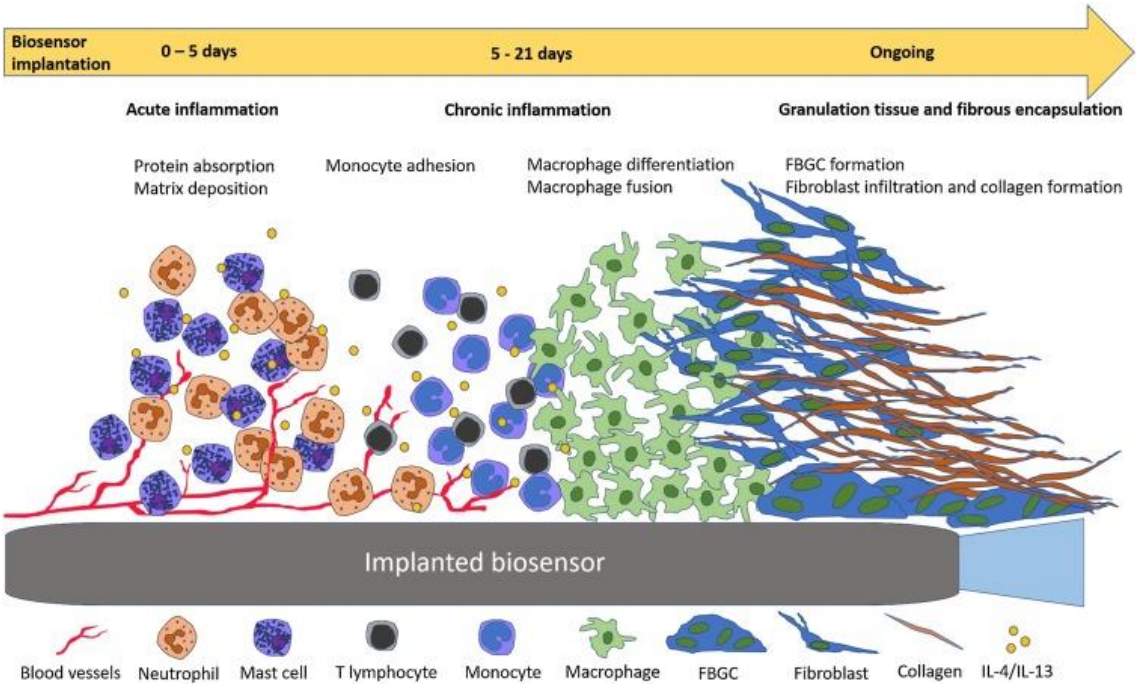

Figure 2.2.2 The stages of inflammation that occur after implantation of a medical device/biosensor. [62].

The implantation of biosensors tends to induce a kind of tissue reaction called foreign body reaction (FBR)[63], which results from the biological contamination around the biosensors. Proteins like albumin, fibrinogen, and complement related to acute inflammations are incredibly prone to attach to the surface of the biomaterials, causing biofouling[64-67]. During the inflammatory response, macrophages release many pro-fibrotic factors that form a fibrous wall around the device. The fiber wall and macrophage combine to create a barrier around the device, resulting in impaired device function[66, 68]. The phenomenon of biofouling is affected by the type of implanted materials[69]. Natural materials are widely used for their inborn biocompatibility. Zhang et al. fabricated silk nanoribbon films with enriched silk II structure[70] capable of self-powered implantable biosensor SNR films. MTT assay was performed to evaluate the cell toxicity of SNR films. The cells exhibited evenly adhesive growth, with typical filamentous and stretched morphology, indicating the sound biocompatibility of SNR

film. Furthermore, the in vivo monitoring potential was verified by testing the sensing performance of SNR film inside adult Sprague-Dawley rats. Fibrin and collagen[71] are also promising natural materials in implantable biosensors with great potential.

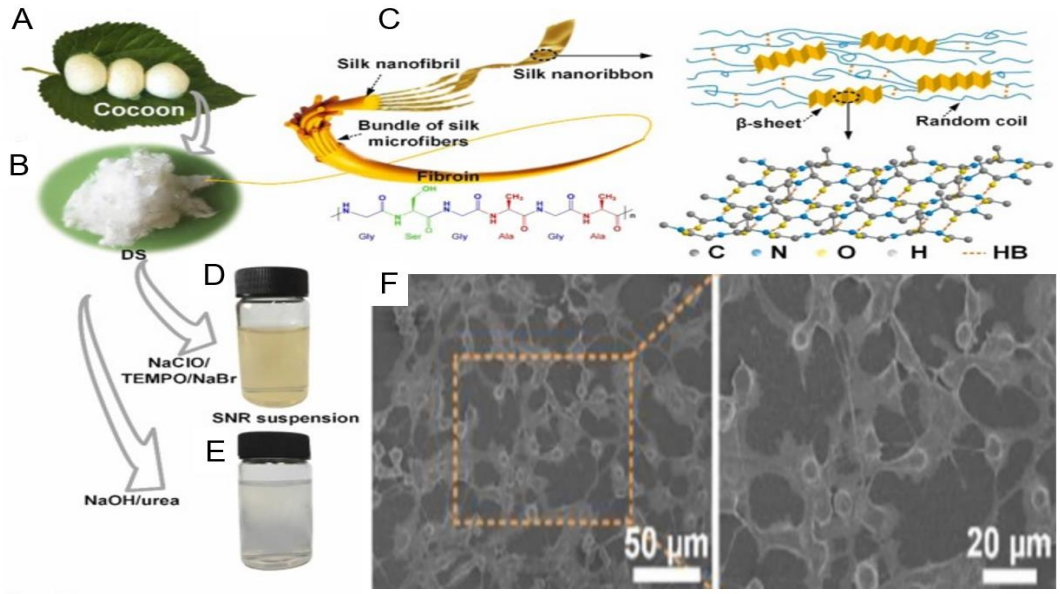

Figure 2.2.3 Photographs of (A-E) fabrication process and morphology of SNR[70]. (F) Representative SEM image of SCs cultured on T-SNR films for 3 d.

Polymer-based materials are also prevalent in implantable devices. Generally, polymers are divided into biodegradable materials like poly(lactic acid) (PLA), poly(glycolic acid) (PGA), poly(lactic-co-glycolic acid) (PLGA), and poly(caprolactone) (PCL) and non-biodegradable materials such as poly(siloxanes), poly (ethylene vinyl acetate) (PEVA), and polyurethanes (PU).

Biodegradable polymers can be broken down into natural components such as water and carbon dioxide in the body, thereby reducing pollution and waste generation[72], causing a massive trend in the healthcare sector. Moreover, the natural breakdown ability allows biodegradable polymers to be turned into drug delivery and in-vivo testing devices without requiring additional steps to remove them from the body[73].

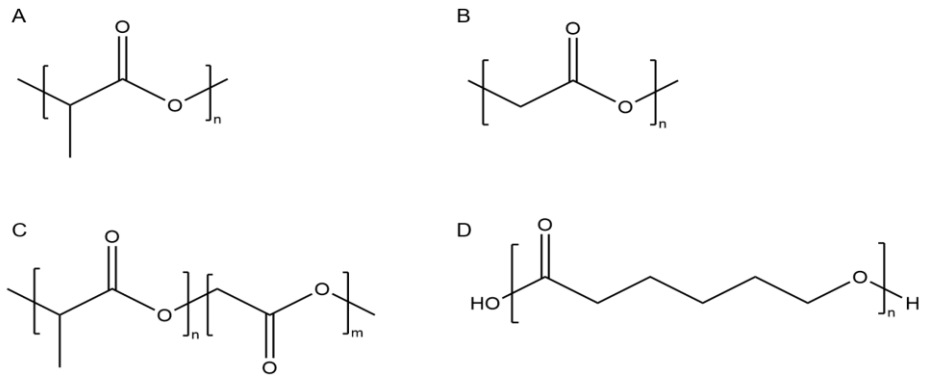

Figure 2.2.4 Structure of (A) PLA; (B) PGA; (C) PLGA; (D) PCL.

PLA is a kind of widely used polymer that can be produced by plants and animals[73], including several branches like pure poly(-L-lactic acid) (PLLA), pure poly(-D-lactic acid) (PDLA), and poly(-D, L-lactic acid) (PDLLA)[74]. A low-cost, miniaturized implantable electrochemical pH sensor for hypoxia monitoring was developed based on PLA in 2021[75].

PGA can promote tissue rejuvenation and cell proliferation, and PGA-based implantable sensors can monitor physiological signals and promote the growth of surrounding tissues and new tissue assimilation. In addition, because PGA[76] nanoparticles can provide controlled drug release, they have a wide range of applications in the field of drug delivery. Fu et al.[77] lessened the bending stiffness of PGA and PLA via the cold plasma surface modification method for the acupoint catgut-embedding therapy applications.

With a low melting point[78] and a long degradation cycle[79], PCL is a polymer with a semi-crystalline structure[80], and its structural repeat unit has five non-polar methylene groups, so it can not only be completely degraded, but the degradation cycle can vary from several months to several years depending on the molecular weight of the polymer. PCL is rich in ether bonds and carbonyl groups, which can be combined with multi-functional isocyanates and chain extenders to produce high-performance polyurethanes

with excellent adhesion to various substrates[81]. In addition, PCL can tolerate a variety of processing methods, such as 3D printing[82], hot extrusion[83], etc. Modification of PCL can also enhance the mechanical properties of the material. Huang's group developed PCL-based, implantable electrochemical biosensors with flexibility and transparency for dopamine monitoring in 2018[84].

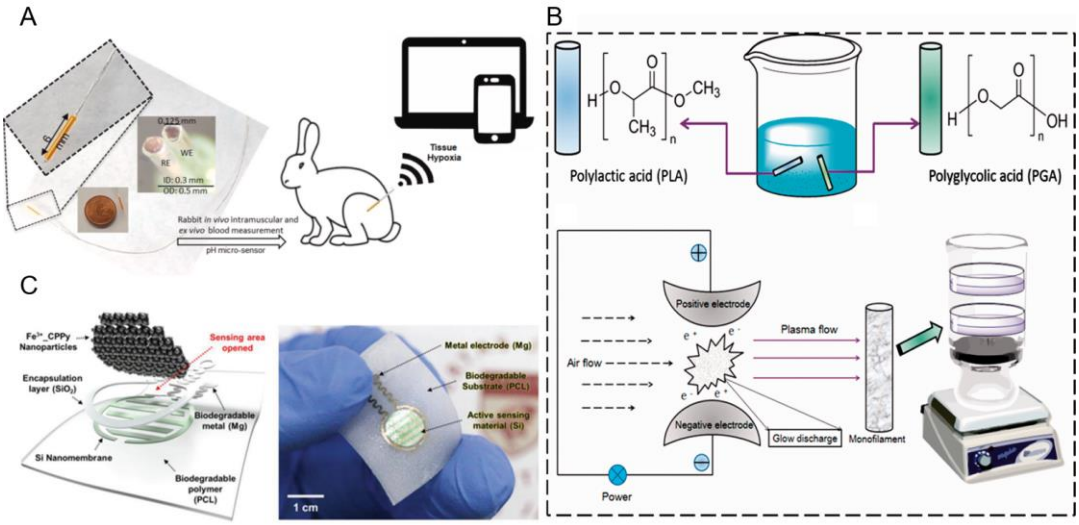

Figure 2.2.5 (A) A scheme of PLA-based pH sensor for hypoxia monitoring[75]; (B) The synthesis process and working mechanism of PLA-PGA sensor via cold plasma surface modification[76]. (C) The PCL-based, transparent, flexible dopamine biosensor[84].

Non-biodegradable synthetic polymers often have a longer working life than biodegradable materials, making them suitable substrates for medical devices that can be implanted or monitored over a long period. These polymers tend to have more potent mechanical properties and higher chemical inertness. They can also function in standard form under relatively more demanding conditions[85]. Polyethylene and polyurethane, for example, are often used to produce joint replacements, which need high mechanical properties while maintaining flexibility[86].

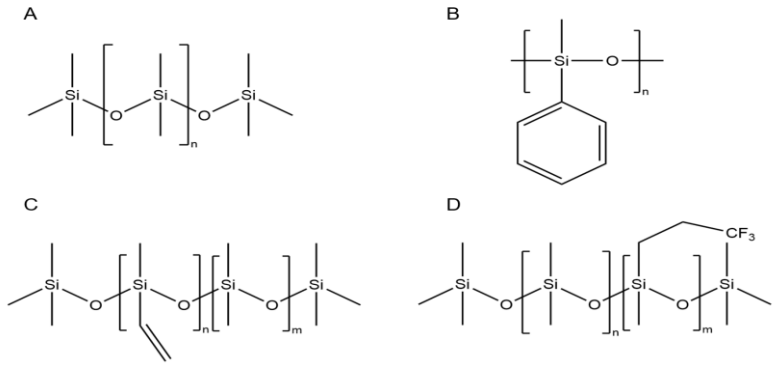

Figure 2.2.6 Structure of (A) Polydimethylsiloxane; (B) Phenyl polysiloxane; (C) Vinyl polysiloxane; (D) Fluoropolysiloxane.

Polysiloxanes are a class of organic compounds composed of silicon and oxygen atoms and various side chains. The side chains include fatty groups such as methyl and aromatic groups and functional groups such as vinyl groups. Different side chains determine the multiple properties of polysiloxanes. For example, polydimethylsiloxane (PDMS) with methyl groups as side chains is the most common polysiloxane type, with excellent chemical stability, electrical insulation, thermal stability, low toxicity, and biocompatibility. It is a transparent, soft material widely used in medical devices, cosmetics, lubricants, and waterproof coatings. A polydimethylsiloxane (PDMS)-based, fully implantable, batteryless soft platform for wireless monitoring of restenosis in real time was produced by printing in 2022[87].

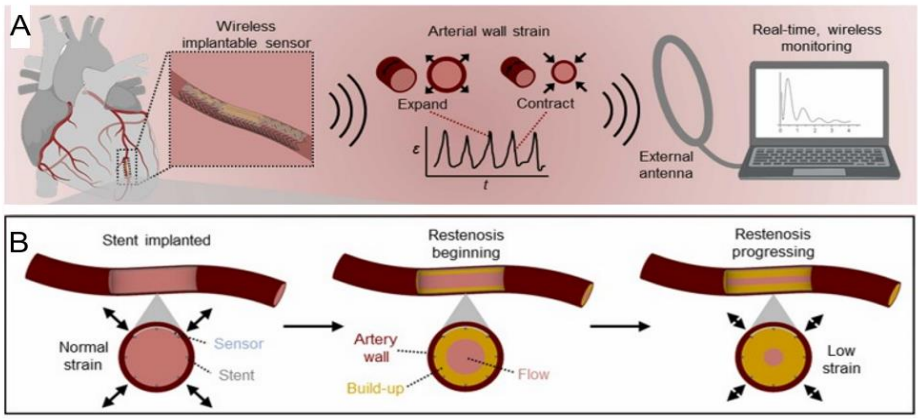

Figure 2.2.7 (A) An implanted wireless sensor for restenosis detection. (B) A stented artery during restenosis progression and the resulting change of arterial wall strain[84, 87].

Compared to PDMS, phenylpolysiloxanes[88] with phenyl as a side chain group have a stronger ability to remain soft at low temperatures and better resist ultraviolet light and ozone. This material is commonly used in applications requiring low-temperature resistance and anti-aging properties, and it is also proper for implantable devices such as injectable lenses[89]. Vinyl polysiloxanes have good crosslinking ability and can be cross-linked by heating or using catalysts to form a network structure with higher mechanical strength and chemical stability[90]. Fluoropolysiloxane has excellent chemical resistance[91], oil resistance, and high-temperature resistance. These materials are commonly used in environments that require resistance to strong acids and alkalis, ensuring high stability in volatile bioenvironments[92].

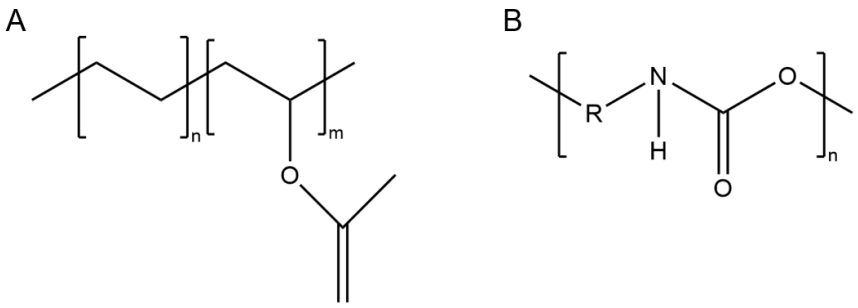

Figure 2.2.8 Structure of (A) PEVA; (B) PU.

Polyvinyl acetate (PEVA) is a copolymer of ethylene and vinyl acetate monomer approved by the FDA, which is widely used in the medical field[93, 94]. The composition of vinyl acetate (VA) affects the melting point and crystallinity of PEVA. By adjusting the composition of VA, PEVA can be prepared to meet the needs of various medical devices such as biological embedding. PEVA is also widely used in blood vessel applications because of its excellent mechanical properties, stability, and ability to resist thrombosis[95].

Polyurethane (PU) has excellent biocompatibility and is often used in artificial organs[96], medical devices[97], orthopedic implants[98], and drug delivery systems[99]. In addition, improved PU can be used to prepare cardiovascular grafts using new tissue engineering techniques[100]. The mixture of polyurethane and hydroxyapatite can provide good adhesion, improve swelling and cell viability, and effectively induce bone formation in stent implantation[101]. Moussy et al.[102] developed a long-term flexible implantable glucose biosensor based on an epoxy-enhanced polyurethane membrane. In this project, the researchers demonstrated that the biosensor implanted in rants could perform well after 56 days of implantation and accurately track the variation of glucose concentration.

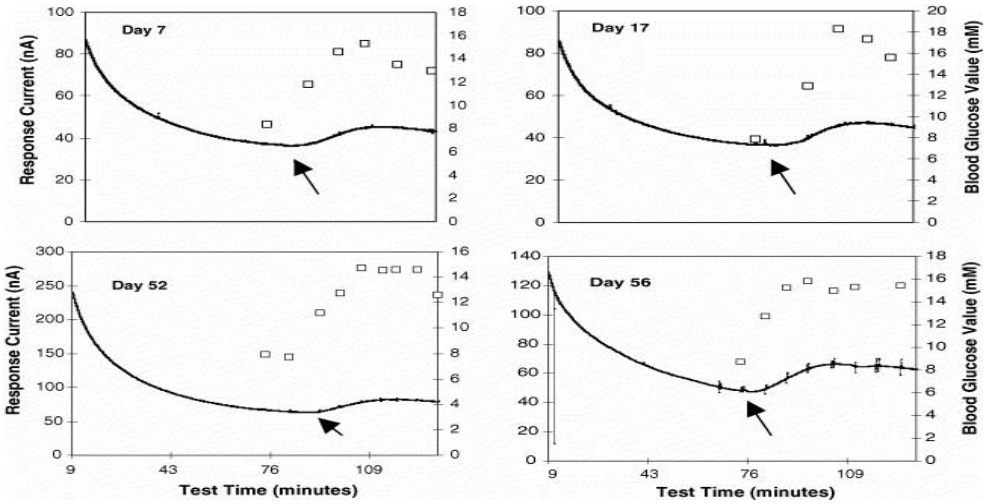

Figure 2.2.9 The comparison between the PU-based glucose sensor and commercial device[102].

Other polymers, such as polyimide, are also used in implantable biosensors. John. A. Rogers' group[12] developed a wireless, miniaturized blood flow sensing system that exploits a sub-millimeter scale based on polyimide substrate with high biocompatibility and stable functionality.

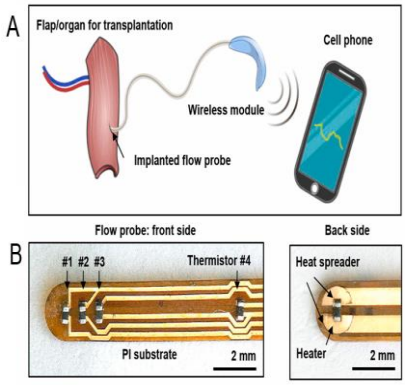

Figure 2.2.10 (A) Schematic illustration of the microvascular flow measurement system. (B) Sensing components in a flow probe[12].

2.2.3 Conductive Materials

As one of the most essential components of biosensors, conductive materials can be used as interfaces and signal transmission in electrochemical sensing. The conductivity and stability of the conductive material directly affect the signal-to-noise ratio, sensitivity, service life, and service conditions of the sensor. When selecting conductive materials, it is often necessary to consider whether the conductive material is in direct contact with the object to be measured. Suppose the conductive part is exposed to the surrounding environment; the conductive material needs to resist the corrosion from chemicals and biofouling from proteins in the biological environment while maintaining good electrical conductivity and having high biocompatibility. For implantable flexible sensors, the conductive material must also have mechanical properties that match the rest of the device. Otherwise, mechanical mismatches make it easy to disintegrate or malfunction the device. In addition, due to the frequent need to

undergo scratching and deformation, conductive materials must also have a tight connection with the substrate to maintain stable electrical properties. This section will introduce the applications of metals, carbon materials, and composites in implantable biosensors according to the types of conductive materials.

2.2.2.1 Metals

Metals, with their distinctive properties, play a pivotal role in the development and functionality of implantable biosensors. These properties include excellent electrical conductivity, biocompatibility, mechanical strength, and corrosion resistance, making metals an ideal choice for such advanced medical devices. The inherent characteristics of metals allow them to facilitate accurate and reliable monitoring of physiological parameters, which is crucial for patient health management.

Electrode	**$k_0/10^{-3}$ cm s^{-1}**	**A_{EA}/cm^2**	**p**
Au planar electrode	1.1 ± 0.1	0.08 ± 0.01	60.36 ± 0.31
Au planar electrode/h-PG	3.0 ± 0.8	1.12 ± 0.02	56.0 ± 0.8
Au planar electrode/Au-MWCNTs	2.7 ± 0.9	1.24 ± 0.02	39.5 ± 0.6
Au microneedles	5.8 ± 0.2	2.02 ± 0.18	10.1 ± 0.6
Au microneedles/h-PG	56.2 ± 0.5	2.02 ± 0.18	1032.1 ± 2.3
Au microneedles/Au-MWCNTs	16.3 ± 0.4	60.36 ± 0.31	301.6 ± 1.6

Table 2.2.1 Heterogeneous electron transfer rate constant (k_0), real electroactive area (AEA), and roughness factor (ρ) of the gold planar electrode and the gold microneedles-based electrode before and after the electrodeposition of h-PG and Au-MWCNTs[103].

Metals are primarily suitable for implantable biosensors because of their exceptional electrical conductivity. This property is vital for efficiently transmitting electrical signals generated in response to biological interactions within the body. For instance,

metals like gold (Au) and platinum (Pt) are widely used in electrodes and electrical contacts within biosensors due to their high conductivity and stability in biological environments[103-105]. These metals ensure that the biosensors can detect minute changes in the physiological condition, enabling early diagnosis and monitoring of health conditions. Gold nanoparticles are known to be easily tailored with different characteristics according to the needs. Most chemical recognition elements, such as DNA adaptors and protein receptors, have been linked to gold nanoparticles to enable the selectivity of biosensors[106, 107]. Antiocha et al.[108] proposed the first high-porous gold-based microneedle capable of minimally invasive glucose monitoring in artificial interstitial fluid (ISF). This method involves the electrodeposition of gold onto the microneedle arrays, which exhibits expanded linear range (0.1 – 10 mM), high sensitivity (50.86 $\mu A \cdot cm^{-2} \cdot mM^{-1}$), stability (20% of signal loss after 30 days), selectivity and short reaction time within 3s.

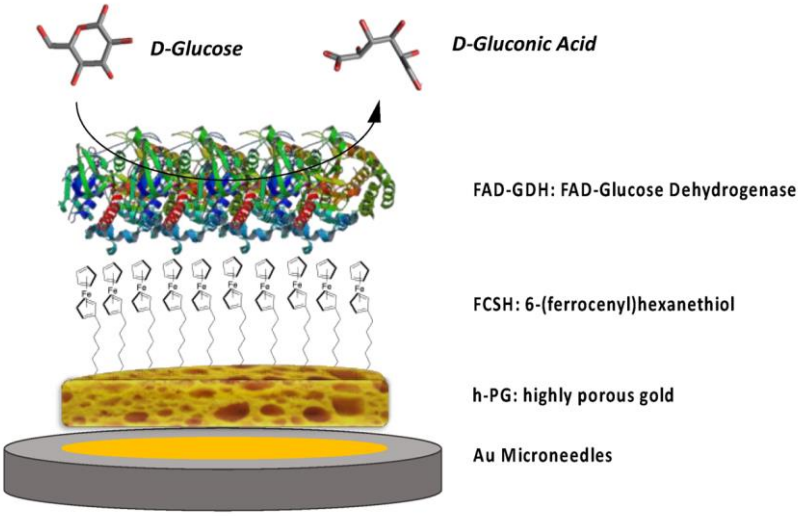

Figure 2.2.11 Schematic representation of Au microneedles-based glucose biosensor[109].

Moreover, biocompatibility is another critical factor that underscores the suitability of metals for implantable applications. Metals such as titanium (Ti) and its alloys are known for their excellent compatibility with human tissue, minimizing the risk of adverse reactions, such as inflammation or rejection[110]. This property ensures that the

implantable biosensors can remain within the body for extended periods without causing harm or discomfort to the patient. In addition, titanium and titanium alloys have excellent mechanical strength, which makes them widely used in biological implants to avoid stress shielding and the associated bone resorption[111]. In particular, the electrochemical oxidation product of titanium, the thin passivated oxide layer, has high corrosion resistance, ensuring titanium's long-term stability and safety of titanium in the body[112]. An implantable antenna utilizing titanium nitrate (TiN) was fabricated for subcutaneous implantation, capable of monitoring blood glucose, alcohol content, various vitamins, and L-lactate[113]. Silver is also compatible with implantable biosensors for the inherent broad antimicrobial spectrum[114]. Specifically, silver nanoparticles (SNPs) are reported to have anti-virus, anti-inflammation, and anti-biofilm activities and enhance wound healing[115]. In 2019, silver nanoparticles were printed onto the PI to fabricate wireless, stretchable, implantable biosensors for cerebral aneurysm hemodynamics monitoring[116].

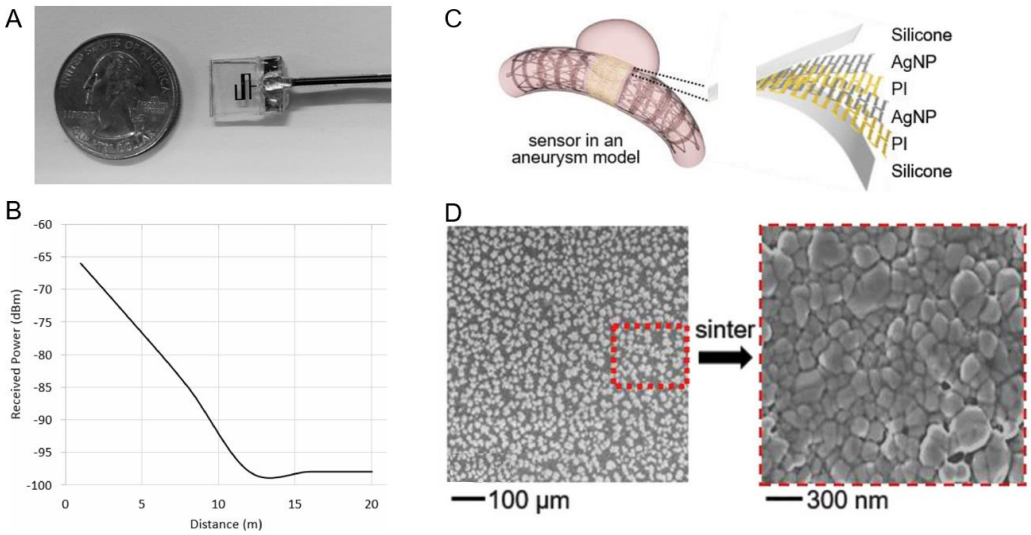

Figure 2.2.12 (A) Scheme of the implantable antenna utilizing Titanium Nitrate[113]. (B) Measured link budget analysis of implanted antenna in vivo. (C) Scheme of Ag deposition. (D) SEM images of AgNPs[116].

In addition to electrical conductivity and biocompatibility, metals exhibit superior mechanical strength and corrosion resistance. These characteristics are essential for the durability and longevity of implantable biosensors, as they must withstand physiological stresses and corrosive environments within the human body. Metals like stainless steel and titanium alloys are particularly valued for their strength and resistance to corrosion, making them suitable for long-term implantation[117].

Despite the numerous advantages that metals offer in the context of implantable biosensors, there are also some limitations and challenges associated with their use. One significant concern is the potential for metal ion release[118], which can occur due to corrosion or wear over time. The release of metal ions into the body can lead to cytotoxicity, allergic reactions, or even chronic inflammation, posing risks to patient health. For instance, nickel and chromium, found in certain stainless steel alloys, are known to elicit allergic responses in some individuals. This necessitates careful selection and processing of metal materials to minimize ion release and ensure long-term biocompatibility[119]. Another limitation is the stiffness of metals, which can be significantly higher than surrounding biological tissues. This mismatch in mechanical properties can lead to stress shielding, where the metal implant bears most mechanical loads, potentially leading to bone resorption or soft tissue damage around the implant site. This issue highlights the need for ongoing research into metal alloys with mechanical properties more closely matched to those of human tissues[120].

Apart from traditional elemental metals with high electrical conductivity but worrying stiffness, the rising star–liquid metals are calling growing attention from researchers in implantable biosensors, especially those requiring softness. The mainstream of liquid metals used in implantable biosensors is gallium (Ga), indium (In), tin (Sn), and their alloys[120]. The melting point of eutectic gallium indium alloy (EGaIn) is 15.4 ^{o}C[121], ensuring their fluidity in ambient temperature. Besides, Young's modulus of liquid metal is as low as 1-10 Pa, 10^7 times less than steel[122]. Besides, liquid metals such as

Ga-based and Bi-based are proven to have sound biocompatibility[123]. Therefore, the near-infinitely stretchable, conductive, safe liquid metals are widely used in tremendous biological applications like reconnection agents in nerve injury[124] and reversible molding bone cement[125].

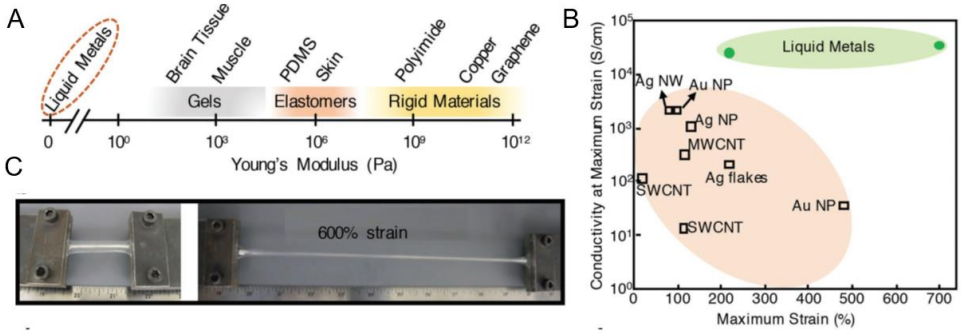

Figure 2.2.13 (A) The comparison of Young's modulus between liquid metals and other materials. (B) The relationship between conductivity at maximum strain and strain. (C) The liquid metal is proven to stretch to 600% strain[126].

Specifically, the application of implantable biosensors is also booming. A kind of stretchable liquid metal microelectrodes (μLME) capable of in vivo monitoring of chronic diseases was fabricated in 2023[127]. The microelectrodes with extremely high stretchability can withstand 300% tension with negligible electrical conductivity loss. The electrical performance remains normal even after 500 times stretching. Furthermore, the authors demonstrated the successful application of implantable monitoring.

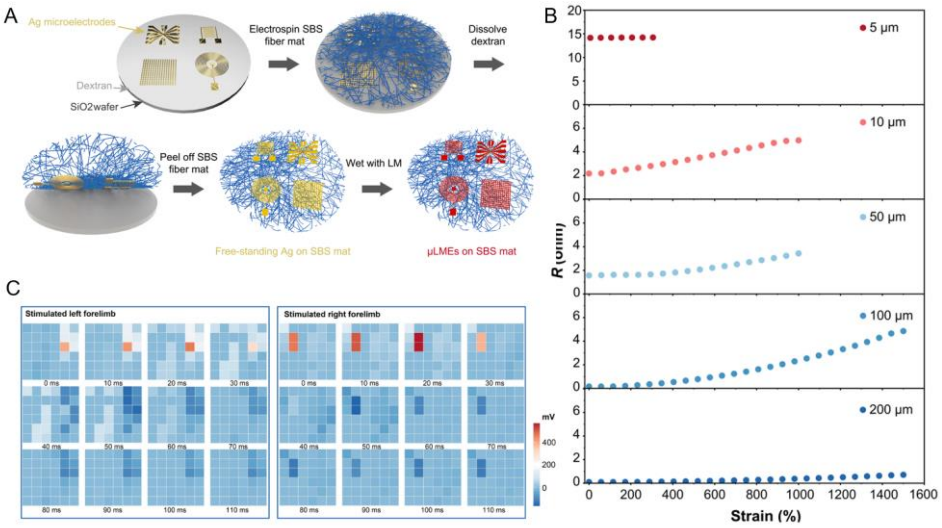

Figure 2.2.14 (A) Scheme and fabrication method of μLME. (B) Resistance of μLMEs of various linewidths at different tensile strains. (C) Spatiotemporal properties for the μLME array[127].

2.2.2.2 Carbon-based Nanomaterials

Carbon-based nanomaterials have a large surface-to-volume ratio, which enriches the exposure of most of the atoms[128]. This unique characteristic makes carbon-based materials capable of being easily modified and connected to various kinds of sensing elements. Besides, their unprecedented high conductivity enables them to be integrated into implantable biosensors with high sensitivity and selectivity. The vast family of carbon-based nanomaterials, including carbon nanotubes (CNTs), graphene, carbon dots (CDs), carbon nanofibers (CNFs), is widely used in medical-related realms like biosensors[129], nanoelectronics[130], tissue engineering[131], and drug delivery[132]. Here, we will mainly discuss the applications of graphene and CNTs in implantable biosensors.

Graphene is the parent of all types of graphite structures; it can be wrapped into 0D fullerenes, rolled into 1D nanotubes, and stacked into 3D graphite[133].

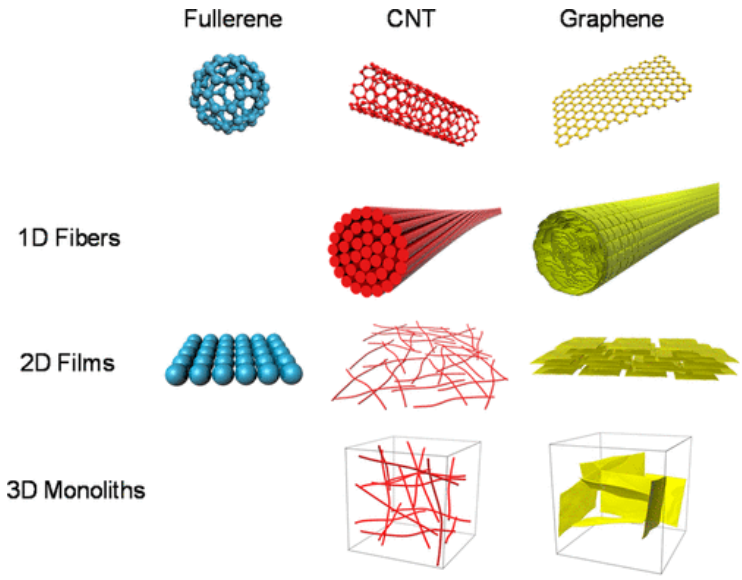

Figure 2.2.15 Structures of fullerene, CNTs, and graphene[134].

With high thermal conductivity[135], outstanding mechanical flexibility[136], high strength[137], and superior electrical conductivity[138], graphene is widely used in implantable biosensors. Graphene can be successfully integrated into cambered devices from the extremely thin layer. For example, Onoe et al.[139] fabricated an implantable tube-shaped blood pressure sensor by combining graphene and a transmitter coil with a polydimethylsiloxane tube. They could effectively monitor femoral arterial blood pressure by implanting a sensor attached to a catheter into the artery to monitor changes in the sensor impedance over time.

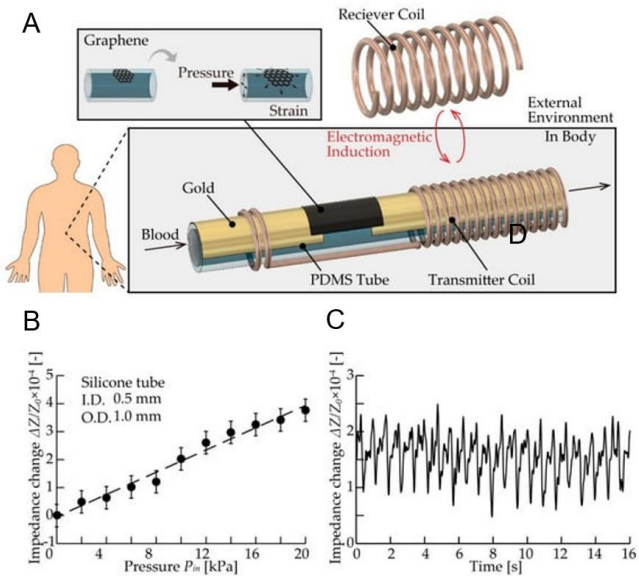

Figure 2.2.16 (A) Scheme of the wireless blood pressure sensor[139]. (B) The relationship between impedance change and blood pressure. (C) The change of impedance gained with time varied.

We can get carbon nanotubes (CNTs) by rolling graphene sheets into cylindrical tubes. CNTs include single-walled CNTs (SWCNTs) and multi-walled CNTs (MWCNTs). Both SWCNTs and MWCNTs can reach the size of a micrometric scale[140]. With a highly specific surface area[141] up to 850 $m^2 \cdot g^{-1}$, the CNTs have been widely used in biomedical areas. The tractable property of CNTs enables them to be easily modified with various functional groups like hydroxyl and carboxyl groups to satisfy different special needs[142]. Furthermore, the CNTs are proven to have sound chemical stability[143], which paves the way for long-term monitoring of implantable biosensors.

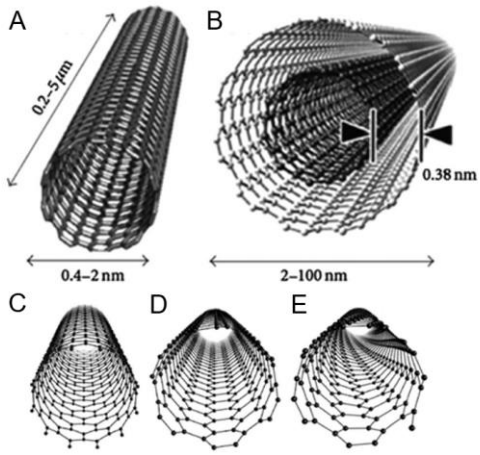

Figure 2.2.17 Diagram of (A) single-walled CNTs (SWCNTs); (B) multi-walled CNTs (MWCNTs); CNT configurations of (C) zigzag; (D) armchair; (E) chiral[140].

Benefiting from the merits mentioned above, CNTs are widely used in implantable biosensors. For example, Peng's group[144] utilized functionalized CNTs to realize the long-term monitoring of multiple indicators in vivo. They obtained the multiple functionalities by rotating different modified CNTs together into a bunch. The researchers also demonstrated the potential of real-time monitoring in vivo by injecting the single fiber into the rats and monitoring the dynamic change of glucose concentration.

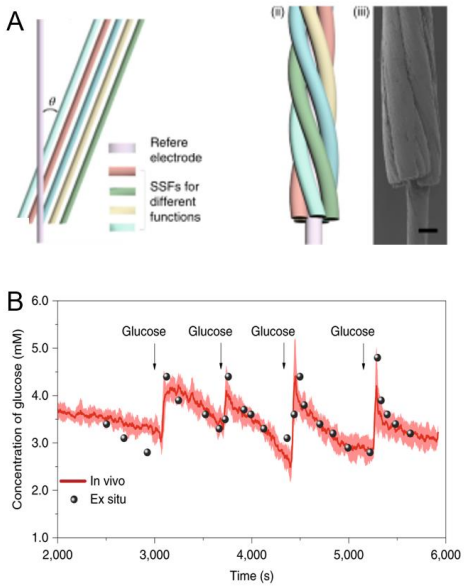

Figure 2.2.18 (A) The CNTs-based implantable biosensors (SSFs) with multiple monitoring functionalities. (B) The in vivo glucose sensing performance of the SSFs implanted in rats[144].

2.3 Fiber-Shaped Biosensors

2.3.1 Working Mechanism of Biosensors

The electrochemical biosensor comprises three essential counterparts: biological interface, converter, and signal transducer[14]. The biological interface, also called "biomolecular/bioagent," has high selectivity and reacts to indicators directly. The converter, sometimes integrated into the biological interface, transports the chemical reaction signals into electrical signals. Some standard chemical reaction signals include electron transfer[145], diffusion potential[146], and heat[147]. The reaction substrates vary with indicators such as DNA adapters[148], ions, molecules, or proteins.[149] The signal transducer works as a vehicle to transport the electrical signals to the eternal device for further collection and processing. The relationship between the measured electrical signal and the analyte concentration is proportional, including methods like amperometric and potentiometric.

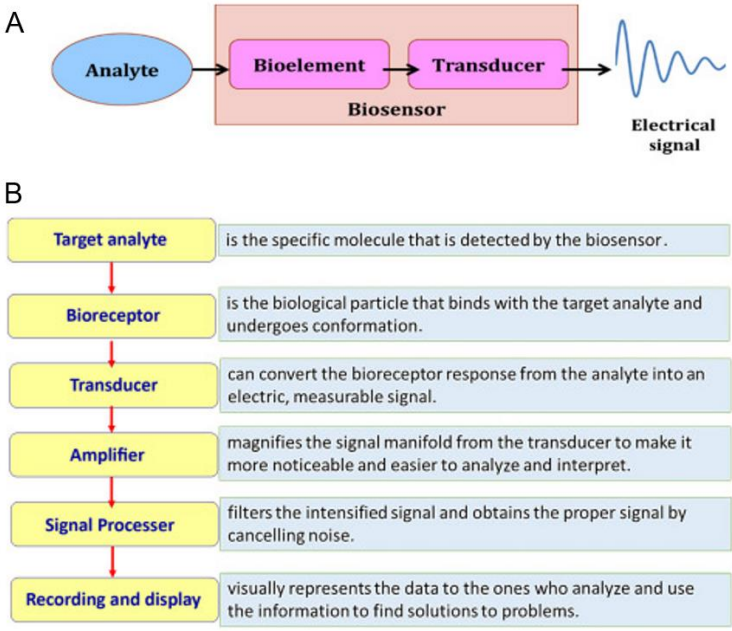

Figure 2.3.1 (A) Schematic representation of an electrochemical biosensor. (B) Component of biosensors[150].

2.3.2 Planar and Fiber-shaped Biosensors

Implantable electrochemical sensors have emerged as powerful tools for continuously monitoring various biomarkers in vivo, providing critical information for disease diagnosis and management. Traditional planar implantable sensors, typically constructed on flat substrates, have been extensively used for easy fabrication and straightforward design. These sensors often consist of a working electrode, a reference electrode, and a counter electrode, all necessary for the electrochemical reactions. They are designed to be minimally invasive and can be implanted under the skin or within tissue to detect analytes such as glucose, lactate, or oxygen.

However, despite their utility, planar sensors have limitations, particularly regarding their form factor and the extent of tissue integration. The relatively flat structure of these sensors can cause significant discomfort to patients and may lead to inflammatory

responses[151]. Moreover, the size of the implantation wound is directly related to the sensor's dimensions, which can be a concern for long-term implantation.

In contrast, fiber-shaped electrochemical biosensors offer a novel approach that addresses many of the shortcomings associated with planar sensors. These sensors are constructed using conductive fibers that can be woven[152] or knitted[153] into flexible and porous structures, allowing them to conform to the body's contours and move with the tissue, thereby reducing mechanical stress and the risk of inflammation. The fibrous nature of these sensors also enables a smaller insertion profile, leading to more minor wounds and potentially faster healing by minimizing the area of inflammation and tissue reaction.

One of the most significant advantages of fiber-shaped biosensors is their ability to penetrate deeper into tissues, providing access to a broader range of physiological environments and the ability to monitor analytes at different tissue depths. This is particularly beneficial for applications that require monitoring of analytes in organs or areas not easily accessible by planar sensors. Peng’s group[154] fabricated a carbon-based OECT biosensor capable of deep brain implantation for 7 days free from related traumas or tissue reactions.

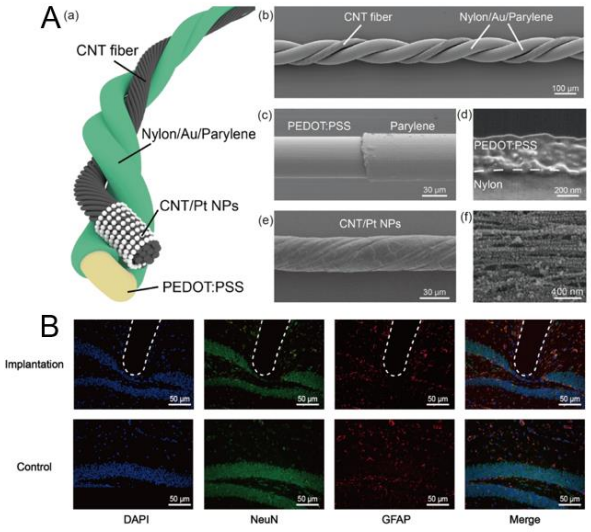

Figure 2.3.2 (A) The schematic view of the OECT biosensor. (B) Fluorescence images of coronal brain slices with implanted fiber-shaped OECTs for 7 d and the control group without implants[154].

Furthermore, fibers' high surface area-to-volume ratio enhances the sensitivity and response time. The increased surface area allows for a higher density of immobilized enzymes or recognition elements, which can lead to improved detection limits and faster signal transduction[155]. This is crucial for the timely detection of rapid changes in biomarker levels, which can indicate acute physiological events.

Mechanically, fiber-shaped biosensors exhibit superior properties due to their flexibility and resilience. They can withstand repeated bending and torsion without losing functionality, essential for biosensors intended to remain implanted for extended periods. This mechanical robustness also means fiber-shaped biosensors are less likely to break or malfunction due to physical stress, ensuring more reliable performance over time. An enzyme-free, implantable, bioactive-based fiber biosensor (MWP) was fabricated by Lin's group[156]. This PDMS-based fiber sensor exhibited high flexibility. The FEA results demonstrate that the strain is consistently smaller than the failure strain (~ 0.03%) even when the device was stretched to 12 mm.

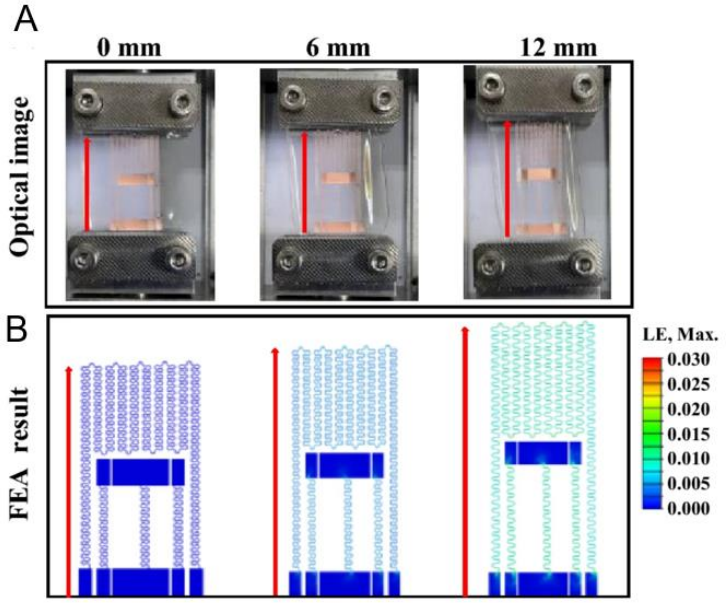

Figure 2.3.3 (A) The experimental photos and (B) FEA results of MWP at the distance of 0 mm, 6 mm, and 12 mm stretch[156].

In summary, while planar implantable electrochemical sensors have played a pivotal role in in vivo monitoring, fiber-shaped biosensors represent a significant advancement. Their flexible and minimally invasive nature, combined with the ability to provide deeper tissue integration and enhanced mechanical properties, positions them as a superior alternative for long-term, continuous monitoring of physiological parameters. As research in this area continues to evolve, fiber-shaped electrochemical biosensors are expected to become increasingly prevalent in clinical and personal health monitoring applications.

2.3.3 Fabrication Methods of Fiber-shaped Biosensors

The fabrication method is vital in determining the mechanical properties, sensing performance, and stability of fiber-shaped biosensors. Here, we introduce four main fabrication methods: wet-spinning, electrospinning, hot extrusion, and hot pressing.

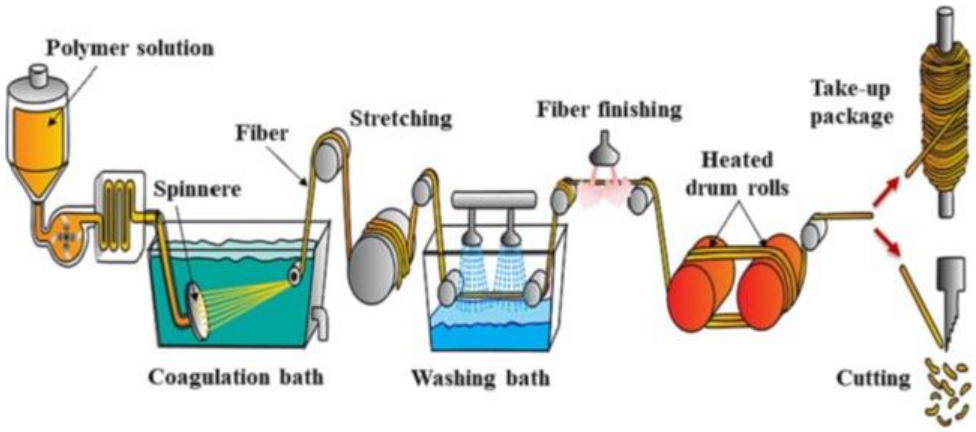

Figure 2.3.4 Schematic illustration of wet-spinning process[157].

Wet spinning: Wet spinning is a process in which a solution is extruded through a spinneret and then formed into a fiber in a coagulation bath[157]. This method is suitable for a variety of natural and synthetic polymers. During this process, fibers of uniform diameter can be prepared, ideal for producing large quantities of fibers. Wet spinning also allows functional materials, such as catalysts or biometric molecules, to be added during the fiber formation process. However, the process is relatively complex and requires specific solvents and coagulation baths, which impact the environment and the operator. The mechanical properties of fibers may be limited. A helical TPU-based strain sensor with high flexibility was fabricated in 2024 via a wet-spinning process[158]. Because of the internal water content, spun fibers have poor electrical conductivity.

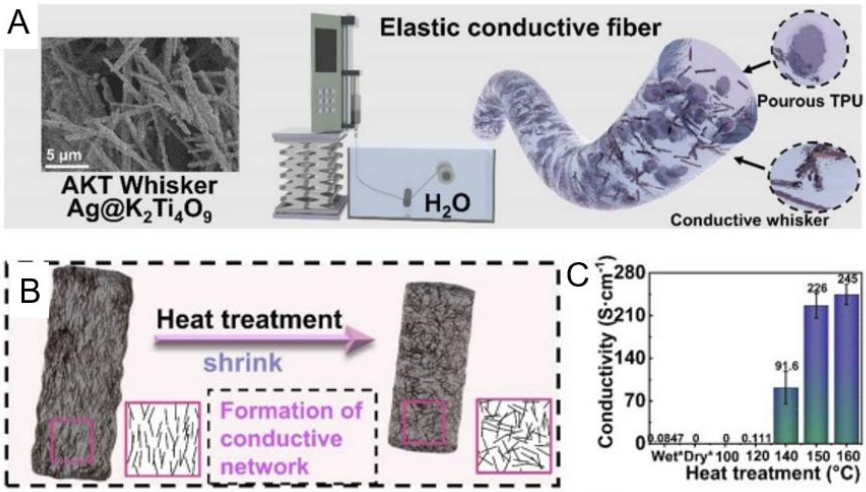

Figure 2.3.5 (A) The fabrication process and morphology of the TPU strain fiber sensor. (B) The effect of heat treatment on the structure of the TPU fiber. (C) The electrical conductivity under heat treatment for 30 minutes under different temperatures[157].

Electrospinning: Electrospinning is a technology that uses high voltage to spray a polymer solution or melt into a fine filament. By controlling the electric field, solution concentration, and other parameters, microfibers with diameters ranging from nanometers to micrometers can be prepared[159]. This method can prepare fibers with a very high specific surface area, which is ideal for use as biosensor substrates. Electrospun fibers can provide more active sites and enhance the sensor's sensitivity and response speed. However, the viscosity and conductivity of the solution must be higher, and the operation complexity is more significant. In addition, the use of high voltages also requires special safety measures. Zhang's group[160] fabricated silk nanofibrous fiber sensors for accurate blood pressure monitoring with long-term stability.

Hot extrusion: Hot extrusion is the process of heating the polymer above its melting point and then extruding it through the die of the extruder to form a fiber[161]. This simple, physical fabrication process enables continuous production and large-scale manufacturing. The diameter and shape of the fibers can be controlled by adjusting the

extrusion parameters. Besides, the mechanical property fabricated via hot extrusion is also better than the methods as mentioned above since this fabrication process does not significantly change the phase of materials. However, this hot method is not suitable for heat-sensitive materials, as high temperatures may damage the structure of bioactive molecules or other functional materials.

Hot pressing: Hot pressing is a method of heating and applying pressure to a material to form the desired shape. It is often used to prepare flat or thin film materials and also used to prepare fiber structures[162]. Hot pressing is more straightforward and suitable for rapid prototyping and small batch production, with relatively low equipment requirements compared to the other three methods. However, for fiber products, the ability to control the size and shape of the fiber is limited, thus not being as flexible as other methods.

Chapter 3 Methodology

In this section, the general methodology for the study is discussed. The project involves the fabrication of multi-channel liquid metal fibers by hot extrusion using a filament extruder, followed by injection and further coating. Methods for surface modification of substrates and fabrication of fibers will be elaborated. Notably, a single fiber with multiple separate conductive channels enabling mass production is developed to improve the functionality of the fiber-shaped biosensor. Finally, the instruments for mechanical and electrical characterization and relative biology experiments will be introduced.

3.1 Materials

All chemicals used in the experiment were used upon receipt without further purification unless specified. The major chemicals used in the experiment are listed as followed: styrene ethylene butylene styrene (SEBS, G1657, KRATON), thermoplastic polyurethane (TPU, 1185A, 1175A, BASF), carboxylated multiwalled carbon nanotubes (CNTs, Nanjing Xianfeng), polylactic acid (PLA, Solvay), polytetrafluoroethylene (PTFE, Xinwang plastic), Perfluoropolyethers (PFPE, Crytox), Eutectic Gallium Indium alloy (EGaIn, Dingguan), Chloroform (Sigma-Aldrich), Tetrahydrofuran (THF, Sigma-Aldrich), methanol (Sigma-Aldrich), potassium tetrakis (4-chlorophenyl) borate (KTFPB, Supelco), sodium tetraphenylborate (NaTPB, Supelco), 4-tert-butylcalix arene (sodium ionophore X, Sigma-Aldrich), valinomycin (potassium ionophore I, Sigma-Aldrich), polyvincyl chloride (PVC, Sigma-Aldrich), Polyvinyl butyral (PVB, Sigma-Aldrich), dioctyl sebacate (DOS, Sigma-Aldrich), sodium chloride (NaCl, Sigma-Aldrich), calcium chloride ($CaCl_2$, Sigma-Aldrich), potassium chloride (KCl, Sigma-Aldrich). Iron(III) chloride ($FeCl_3$ Sigma-Aldrich), potassium ferricyanide ($K_3[Fe(CN)_6]$, Sigma-Aldrich), hydrogen chloride (HCl,

Sigma-Aldrich), nickel(II) nitrate ($Ni(NO_3)_2$, Sigma-Aldrich), silver nitrate ($AgNO_3$, Sigma-Aldrich), potassium nitrate (KNO_3, Sigma-Aldrich), Serazine hydrochloride injection, Sutai 50, Benzoxazole hydrochloride injection, lodine volt disinfectant, 75% Alcohol disinfectant, Absolute ethanol, 95% Ethanol, Xylene.Hematoxylin dye, Eosin dye solution.

3.2 Fabrication

3.2.1 Fabrication of Multi-Channel Conductive Fiber

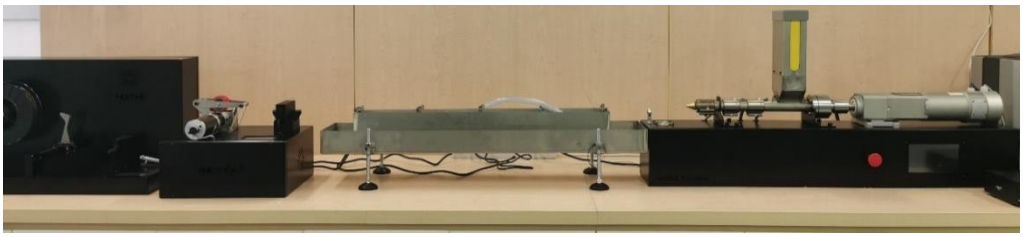

Figure 3.2.1 Optical images of Noztek XCalibur Filament Extruder.

The three-channel flexible fiber supports the electrodes and creates channels for liquid metal transmission. The material of the fiber is thermoplastic polyurethane 1185A, and the fibers are fabricated by using the filament extruder. The hot extrusion temperature gradient of the three chambers is set as 210ºC, 200ºC, and 195ºC, respectively. The fan speed is 25%, and the motor speed is 4 rpm. After adding the plastic particles TPU, the particles are heated and held in the cavity for five minutes to ensure the continuity of the extrusion material, and then the rotating motor is turned on. The nozzles are customized by vendors to obtain hollow fibers.

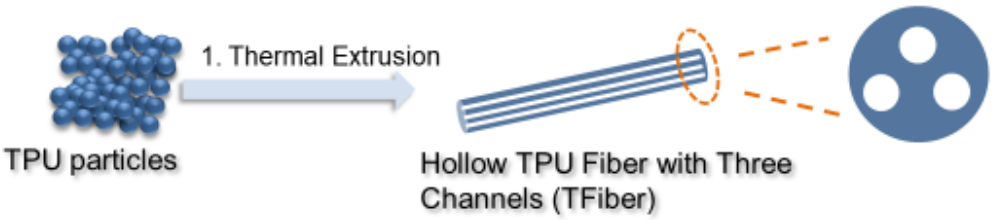

Figure 3.2.2 The schematic illustration of the hot extrusion process.

The hollow TPU fiber is protruded with scissors to create three VIAs to connect each channel, followed by injecting eutectic gallium-indium alloy (EGaIn) into the channels. For every channel 10cm long and 0.05cm in diameter, 0.12g EGaIn is injected into the channel using a 1 mL syringe after pre-stretching the as-made fibers. The consistency of instill is eligible to be verified by the naked eye and an Avometer. The EGaIn-filled conductive fiber fabricated is denoted as EFiber.

3.2.2 Fabrication of Three-Electrode Fiber

To prevent the leakage of EGaIn, 1 mL of glutinous PTFE/PFPE/CNTs interlayer is dip-coated onto the VIA. The three materials are added together via different weight ratios as follows. The cocktail is treated with ultrasonic for five minutes to diffuse the PTFE powder and CNTs into the PFPE oil, followed by stirring with a magnetic rotor for thirty minutes at 200 rpm until a glutinous cocktail is obtained.

	Weight (g)			
PFPE	2	2	3	5
PTFE	1	0.5	0.25	0.5
CNTs	0.10	0.15	0.15	0.35

Tabe 3.2.1 The weight value of different components for the interlayer.

The ion-to-electron transducer layer composed of PLA and CNTs is dip-coated onto the interlayer. The weight ratio of PLA and CNTs is presented as follows. The mixture is dissolved in chloroform/THF=3:1 solvent, wherein the THF works as a cosolvent for PLA. The solution was treated with ultrasonic for fifteen minutes to distribute CNTs evenly. To prevent the aggravation of CNTs, the solution is kept stirring at 250 rpm. For each VIA, 1 mL of the PLA/CNTs transducer solution is dip-coated onto the interlayer.

Group	**1**	**2**	**3**	**4**	**5**
PLA/CNTs w/w	2:1	4:1	6:1	8:1	10:1

Table 3.2.2 The weight value of PLA and CNTs for transducer solution.

After waiting 10 minutes for the transducer solution to dry, another two times of transducer dip coating are repeated to gain better electrical conductivity, followed by drying at room condition for three hours. Then, the transducer-interlayer-EGaIn fiber is successfully fabricated and denoted as TIEFiber.

3.2.3 Fabrication of Sensing Electrodes

The sodium ion, potassium ion, and glucose sensing working electrodes are fabricated in this project. The reference electrode was also made using the fiber for demonstration.

Sodium ion sensing working electrode: A Na^+-selective membrane was prepared by mixing 0.2% KTFPB, 0.7% 4-tert-butylcalix arene, 33% PVC, 66.1% DOS. Then, 1 g of this Na^+-selective membrane cocktail is dissolved in 3.3 mL THF. 20 μL of the cocktail is dipped on the transducer and left for drying in ambient conditions for two hours. The cocktail is sealed and stored at 4 ^oC for further use.

Potassium ion sensing working electrode: A K^+-selective membrane was prepared by mixing 2% valinomycin, 0.2% NaTPB, 32.7% PVC, and 64.7% DOS. Then, 100mg of this K^+-selective membrane was prepared by mixing it with 350 μL of cyclohexane. 20 μL of the cocktail is dipped on the transducer and left for drying in ambient conditions for two hours. The cocktail is sealed and stored at 4 ^oC for further use.

Glucose sensing working electrode: The glucose sensor is an enzyme-based electrode. 1wt% agarose and 1wt% chitosan are dissolved in 2% acrylic acid to form Aga/Chi emulsion. 1 mg glucose oxidase is dissolved in 100 μL 1X PBS (pH 7.2). The glucose oxidase solution is mixed with the Aga/Chi emulsion in a 1:2 (v:v) fraction to form the glucose oxidase cocktail. First, the encapsulated fiber is electrodeposited with Prussian Blue by immersing in a 2.5×10^{-3} M $FeCl_3$, 2.5×10^{-3} M $K_3[Fe(CN)_6]$, 0.1 M KCl, 0.1M HCl solution with cyclic voltammetry method by sweeping from 0 to 0.5V for three times at a scanning speed of 0.02 V/s with a commercial Ag/AgCl reference electrode and Pt counter electrode. After drying, The NiHCF stabilization layer is electrodeposited with cyclic voltammetry method by immersing the PB/CNT fiber into an aqueous solution of 1×10^{-3} M $Ni(NO_3)_2$, 0.5×10^{-3} M $K_3[Fe(CN)_6]$, 1 M KCl by sweeping from 0 to 0.8V at 0.1V/s at three times with a commercial Ag/AgCl reference electrode and Pt counter electrode. The as-made fiber is called Ni/PB/CNTs fiber. After drying up, 20 μL of the glucose oxidase cocktail is dipped onto the fiber to form the glucose sensing working electrode and dried at 4^oC. Before testing, the glucose sensing working electrode should be taken out into ambient condition 5 minutes ahead of time to melt the liquid metal.

Reference electrode: The fiber is firstly electrodeposited via cyclic voltammetry method with silver by immersing the encapsulated fiber into an aqueous solution of 5 mM $AgNO_3$ and 1M KNO_3 by sweeping from -0.9V to 0.9V at 0.1V/s for 14 cycles with two electrode system, where the fiber is the working electrode and the commercial silver electrode is both the counter electrode and the reference electrode. Then AgCl is

electrodeposited onto the Ag/CNTs fiber via cyclic voltammetry method by immersed into an aqueous solution of 0.1 M KCl and 0.01 M HCl by sweeping from -0.15 to 1.05 V at 0.05 V/s for two cycles with the commercial Ag/AgCl as both the reference and the counter electrode. To minimize the potential drift, 30 μL of a mixture composed of 79.1 mg polyvinyl butyral (PVB), 50 mg NaCl, and 0.2 mg CNTs dissolved in 1 mL methanol is dipped onto the reference electrode and left dry in ambient condition.

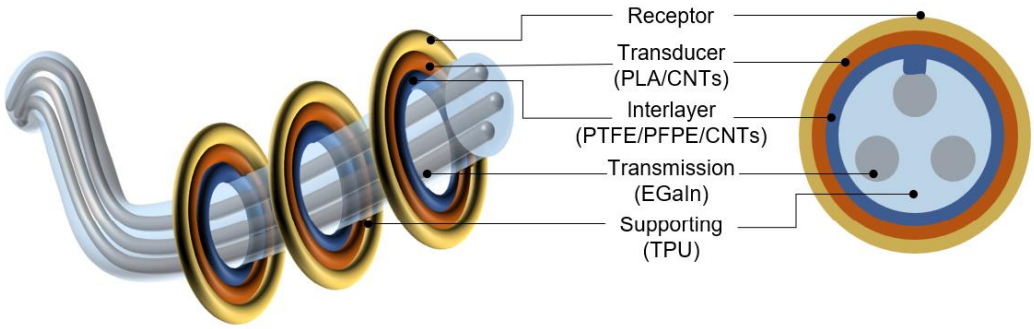

Figure 3.2.3 Schematic and composition of TIEFS. Insert at the right is a cross-sectional schematic view of TIEFS.

3.3 Characterization

The microstructures of the fibers were taken by Scanning Electron Microscope (MIRA, TESCAN Ltd., Czech Republic). The water contact angle was tested on the contact angle meter (SDC-350, Dongguan Shengding Precision Instrument Co., Ltd., China). The tensile and Young's modulus were tested on the Instron 5566 Universal Testing Machine (Instron, USA). The electrochemical properties were tested on the CHI 660 Electrochemistry Station (CH Instruments, Inc., USA). The animal test was conducted on an automatic tissue dehydrator, rotary slicing machine, automatic dyeing sealing machine, and forward fluorescence microscope.

Chapter 4 Fabrication and Characterization of EGaIn-Filled Fiber (EFiber)

4.1 Morphology of Hollow Fiber

Benefiting from the thermoplastic property of TPU, different diameters varying from 150 μm to 4 mm of flexible hollow fibers are fabricated by tuning the pulling-out speed during extrusion. The additional heating process before starting the extruder rotor ensures the consistent and even extrusion of the fibers. Figure 4.1.1 A shows the variable diameters of hollow fibers with three channels. The three channels are visibly separated, as shown in Figure 4.1.1 B, C.

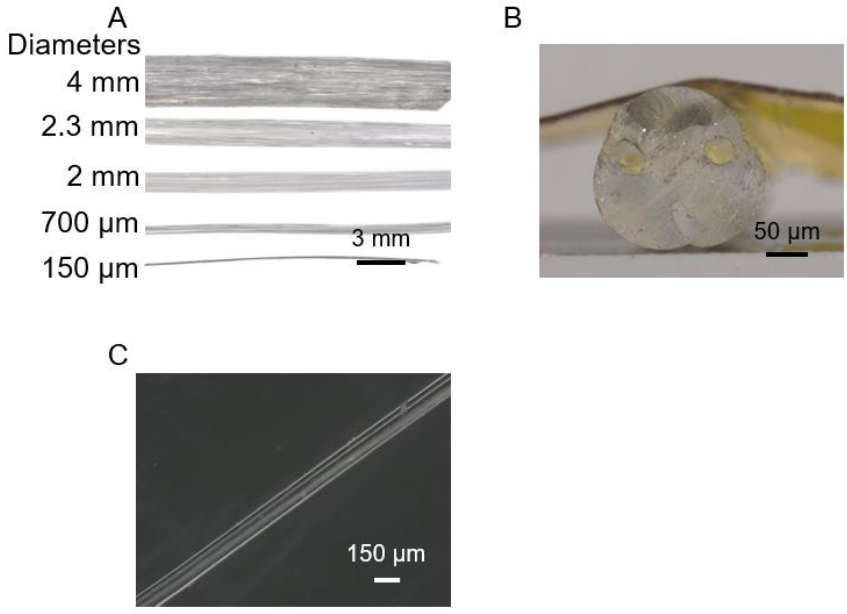

Figure 4.1.1 (A) Three-channel hollow TPU fibers with diameters from 2 mm to 150 μm. (B) Cross-sectional view of three-channel fiber. (C) Optical image of three-channel fiber.

4.2 Mechanical Properties of Hollow Fiber

Our investigation into the mechanical performance of the fibers, as illustrated in Figure 4.2.1 A, has yielded significant implications. For comparison, we also manufactured solid and hollow fibers using SEBS. The Young's modulus of the solid fiber, hollow SEBS fiber, and hollow TPU fiber are 12.582 MPa, 2.9342 MPa, and 0.01MPa, respectively. All three fibers can stretch over 800% of their original length. The substantial difference in Young's modulus among these samples is attributed to the presence of a channel. According to the information obtained from the vendor, the expected Young's modulus of SEBS and TPU are 2.4 MPa and 24.8 MPa. However, the one-channel SEBS fiber and three-channel TPU fiber exhibit the reverse Young's modulus result. The existence of a channel, which lies precisely in the middle of the cylindrical fiber, lessens the dosage of plastics. However, the calculated volume remains the same, which gives the chance to reduce Young's modulus. The hollow channel reduces the lining support of the fibers while providing a volumetric space for the walls. This design feature makes the fibers more prone to deformation with less strain, a crucial factor for the flexibility required to implant devices to avoid trauma to surrounding soft tissues.

The hysteresis loop areas as shown in Figure 4.2.1 B, C of hollow SEBS fiber and hollow TPU fiber are 1003.66 and 586.89, respectively. The smaller hysteresis loop area indicates the less energy dissipation capacity incurred by the internal friction of materials during deformation, which is consistent with the former assumption about the reduction of Young's modulus. Through the stress-strain loop, we can also conclude that after the first stretching cycle, the strain difference during the following stretching is negligible. Therefore, pre-stretching before applying this fiber is necessary to maintain its stable mechanical properties.

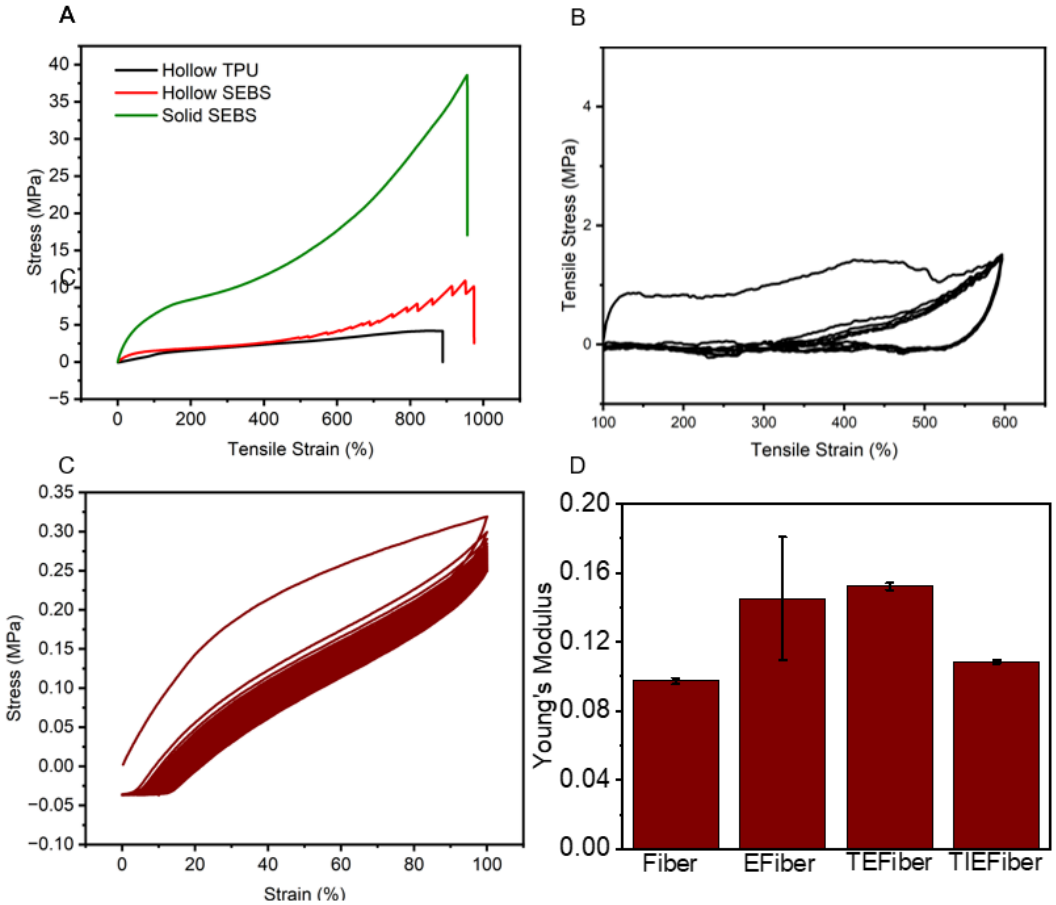

Figure 4.2.1 (A) Stress-strain comparison between hollow fibers made of TPU, SEBS, and solid fibers made of SEBS. (B) Stress-strain loop of SEBS. (C) Stress-strain loop of TPU (D) Young's modulus comparison of the bear hollow fiber (Fiber), the bear three-channel fiber with one channel filled with liquid metal (EFiber), transducer-EGaIn fiber (TEFiber), and transducer-interlayer-EGaIn fiber (TIEFiber).

To study the mechanical influence of the liquid metal, PLA/CNTs transducer layer, and PTFE/PFPE/CNTs interface on the fiber, we also calculated Young's modulus at 5% stretch of bear hollow fiber, the bear three-channel fiber with one channel filled with liquid metal, single LM fiber coated with transducer layer and single fiber coated with interface and transducer layer as depicted in Figure 4.2.1 D. The Young's modulus is 0.09739 MPa, 0.14518 MPa, 0.1521 MPa, and 0.10844 MPa, separately. Although both the injection of liquid metal and the PLA/CNTs-based transducer layer increased Young's modulus, the soft, glutinous PTFE/PFPE/CNTs interface lowered Young's

modulus. Therefore, we can infer that the whole process of interlayer-transducer fiber fabrication does not significantly affect Young's modulus of the fiber.

4.3 Electrical Property of EFiber

Liquid metal is prevalent in applying flexible electronics for high stretchability and conductivity, specifically since the ingenious creativity accomplished by Dr Michael. D. Dickey and his group[163], who first injected the liquid metal into the SEBS hollow fiber, said that the stretchability of liquid metal has been more widely disinterred in the fiber realm. Here, we opted for the eutectic gallium indium alloy (EGaIn) with a melting temperature of 16 ^{o}C and injected it into the hollow TPU fiber. The injection of EGaIn does not significantly affect the mechanical property of the fiber, as there is no chemical reaction or physical change. We then tested the electrical performance under stretching and bending. The result (Figure 4.3.1 A, B) shows that the LM-filled fiber is strain intensive to 124%, with a negligible resistance change. This stability in the resistance of the fiber, even under such high strain, instills confidence in the stability of the material. The conductivity is higher than that of silver and copper, which is under around 150% stretching. Even under 700% stretching, the fiber is still conductive, around 6 MS/m. The test concluded with the fallen-off of the test fixture and the length limitation of the wire.

Then, we conducted a fatigue-resistant test. As depicted in Figure 4.3.1 C, the three stages of stretching: 6-fold elongation, 8-fold elongation, and 10-fold elongation, all demonstrated a stable conductivity cycle under stretching, with minimal variation. This stability in the conductivity cycle provides a strong reassurance of the reliability of our results. Furthermore, the figure also illustrates that with longer stretching, the maximum conductivity of each cycle is increasing, which is in line with the hysteresis test result.

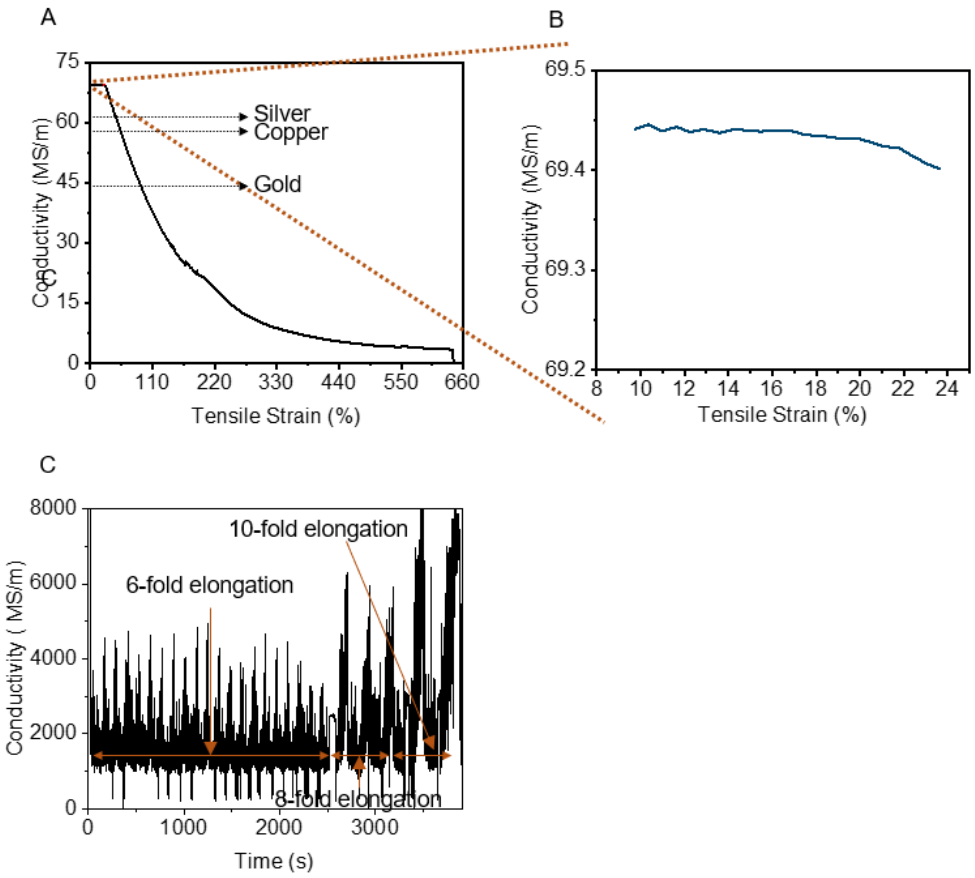

Figure 4.3.1 (A) Conductivity of the hollow TPU fiber under stretching to 700%. The end of the test for the test fixture is off, and the length of the wires is limited. (B) Zoomed-in image of the conductivity of the hollow TPU fiber under stretching to 125%. (C) The conductivity change under more than 2000 times of 6-fold elongation, hundreds of times of 8-fold elongation, and 500 times of 10-fold elongation.

Chapter 5 Fabrication and Characterization of Multifunctional Implantable Fiber-shaped Sensor

5.1 Structure of Fiber-shaped Sensor

5.1.1 Overview of Fiber-shaped Sensor

The transducer-interlayer-EGaIn fiber sensor consists of three electrodes: one reference electrode and two ion-selective working electrodes, as depicted in Figure 5.1.1 A and C. All three electrodes are composed of an interlayer and a transducer, as shown in Figure 5.1.1 B. The difference among the three electrodes is that sodium selective membrane and potassium selective membrane are coated on the transducer of the two working electrodes, respectively, and Ag/AgCl is electroplated on the transducer of the reference electrode, followed by coating PVB/NaCl to minimize the signal drift. For sodium and potassium sensing, The potential-response sensing performance is not significantly related to the area of electrodes[164], so for convenient operation, each electrode is fabricated as 6 mm long.

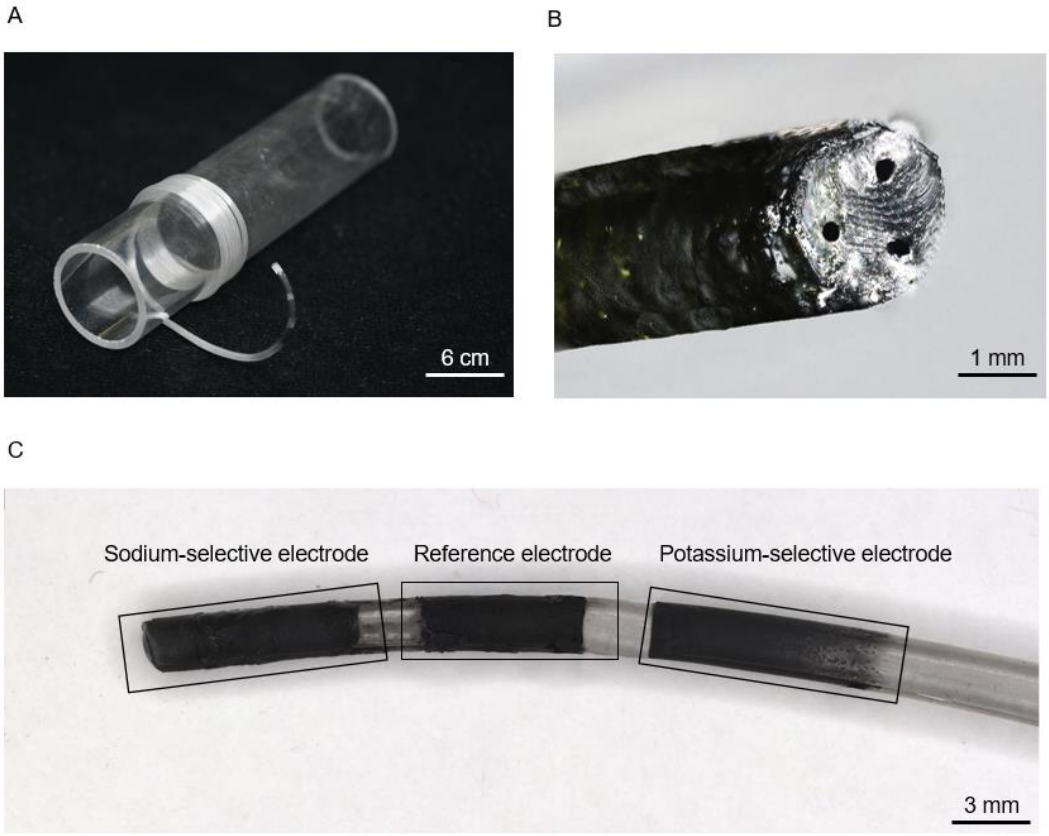

Figure 5.1.1 (A) The structure of TIEFS. (B) The cross-sectional view of TIEFS. (C) The overview of three electrodes on TIEFS.

.

5.1.2 Transducer Layer

Though the satisfying fluidic merit of the liquid metal, the corrosive and high surface tension of liquid metal indicate the pending of an encapsulation interface, which inhibits the leak of liquid metal while maintaining superior electrical conductivity. Typically, most researchers use glue to encapsulate and insert conductive wires like copper or silver[126, 165-167]. However, this prevalent method is not convenient for practical use since the mechanical mismatch between the rigid wire and the flexible fibers could cause electrical instability and even misconnection between the fiber and the terminal devices. Therefore, a flexible, electrical conductive encapsulation layer is pending to be developed.

Initially, we chose a mixture of PLA and carboxylated multi-walled carbon nanotubes. The carboxylation of CNTs provides opportunities to form hydrogen bonds and more potent van der Waals force with liquid metal, forming a stable three-dimensional conductive network that minimizes resistance change under stretching or bending. The PLA works as both the supporting bracket for CNTs and the glue-like material for CNTs to get better attachment to TPU fiber.

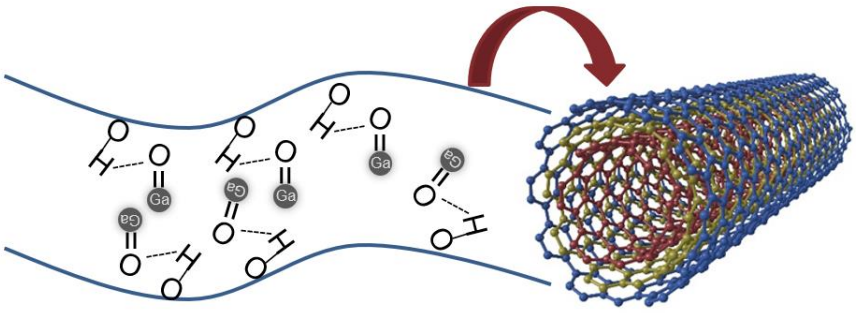

Figure 5.1.2 The three-dimensional conductive network. Blue lines on the left and the right circles indicate the carboxylated multi-walled carbon nanotubes. The gray rounds indicate liquid metal EGaIn.

We then compared the effect of the weight ratio of CNTs. According to the previous study[168], the conductive polymer composite (CPC) conductivity versus the content of CNTs relates to the filler percolation phenomena. When the concentration of filler particles in the matrix is below a certain threshold, the particles are randomly dispersed, and there is no continuous pathway for the desired property enhancement. However, as the filler concentration increases, a critical point is reached where the particles connect and form a percolating network. At this percolation threshold, the filler particles create a continuous pathway that enables the desired property to be significantly enhanced. Near the filler percolation, the complex process of tunneling effects may influence conductivity, thus obtaining higher sensitivity. The PLA formed numerous holes after the evaporation of the solution as shown in Figure 5.1.3 A, and CNTs should occupy the hole. With the increasing weight ratio of CNTs, the film's resistance is lower, consistent with the filler percolation theory. Then, we measured the hole and hole-to-

edge ratio of different films as shown in Figure 5.1.3 C, D. In the weight ratio range between 0.075 to 0.15, the hole and the hole-to-edge ratio increase to a small extent. In contrast, around 0.33, the hole diameter is much higher, and the hole-to-edge ratio is much less. Therefore, we infer that the sharp difference is because 0.33 is near the filler percolation; thus, the tunneling effect is dominant in resistance—the more PLA results in less possibility of electron transmission across the isolation layer.

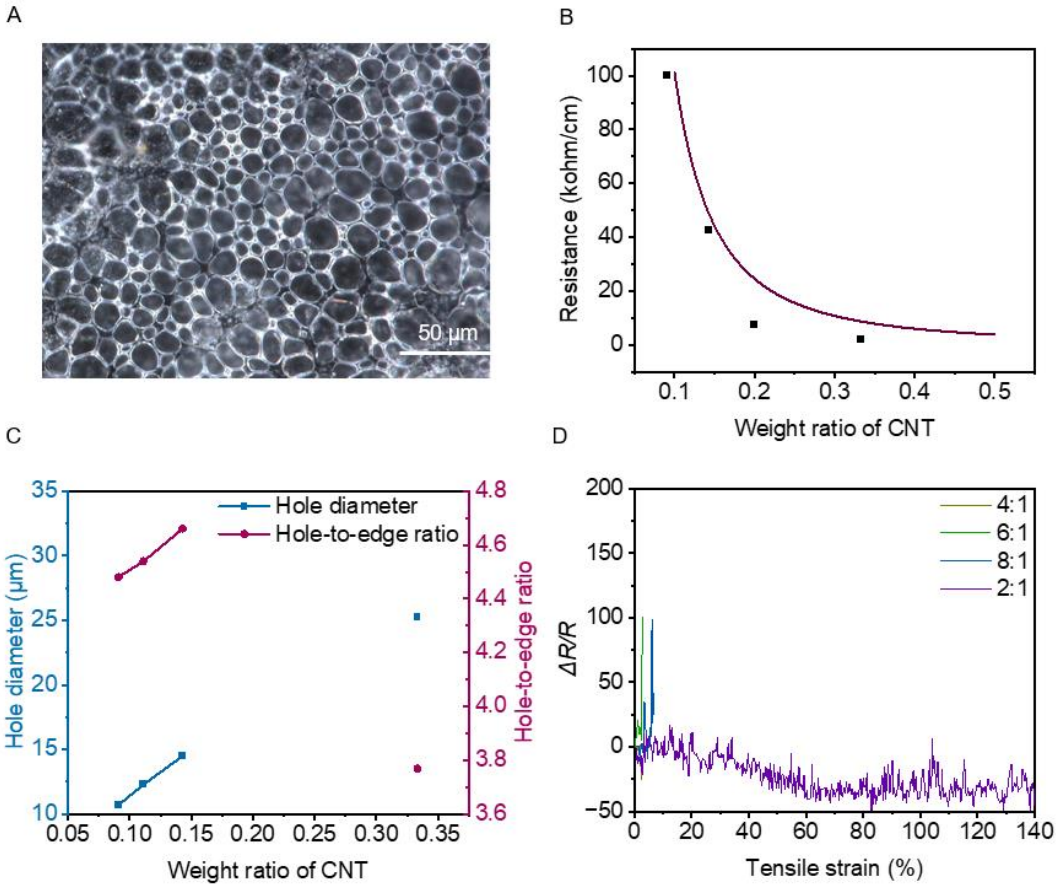

Figure 5.1.3 (A) The optical image of PLA/CNTs composite membrane. (B) The effect of the weight ratio of CNTs on the resistance. (C) The difference in hole diameter and the ratio of the distance from the hole to the edge of the membrane to the hole diameter among different weight ratios of CNTs, referred to as the 'hole-to-edge ratio difference '. (D) The resistance change under stretching of the TEFiber with different weight ratios of CNTs. 2:1, 4:1, 6:1, and 10:1 refer to the weight ratio of PLA to CNTs.

Then we investigated the electrical stability of the as prepared fibers under stretching. The liquid metal-filled fibers encapsulated with PLA/CNTs, composed of different weight ratios of CNTs, were subjected to stretching at a carefully controlled, uniform speed. Figure 5.1.3 highlights that the 2:1 weight ratio stands out, maintaining the most stable resistance even when stretched to 140%. In contrast, the other groups experienced sharp resistance changes within 10% strain, possibly due to the stable connection between the liquid metal and the CNTs. This reassures the reliability of our experimental setup and the consistency of our results.

We further investigated the effect on the functionality of different weight ratios of CNTs. For demonstration, the sodium selective membrane is dip-coated onto the encapsulated end of the transducer-EGaIn fiber (TEFiber), followed by testing the open circle voltage responding to different concentrations of NaCl solution relative to the Ag/AgCl reference electrode. Figure 5.1.4 shows the performance variation. Consistent with the percolation theory discussed before, the weight ratio of 2:1 behaves the best. We infer three probable reasons: higher charge transfer efficiency, which refers to the rate at which charge is transferred from the electrode to the electrolyte, higher signal-to-noise ratio, which is the ratio of the signal power to the noise power, and more active electrode surface process. Electrodes with lower resistance have higher charge transfer efficiency, which means that when the electrode surface reacts with sodium ions, electrons are more easily moved between the electrode and the electrolyte. Therefore, when the concentration of sodium ions in the solution changes, the potential change on the electrode surface will also be more rapid and easily observed, thus improving the sensitivity to sodium ions. Besides, electrodes with lower resistance produce lower thermal noise during measurement. Resistive components in electrodes and circuits generate thermal noise, which can affect the clarity of the measured signal. Lower thermal noise means a higher signal-to-noise ratio, which helps more accurately detect and respond to changes in sodium ion concentration. Furthermore, electrodes with more negligible resistance may have better electrochemical activity on their surface,

facilitating the ion exchange process on the sodium ion selective membrane. The higher the electrochemical activity of the electrode surface, the stronger the interaction between sodium ions and the selected film, thus increasing the sensitivity.

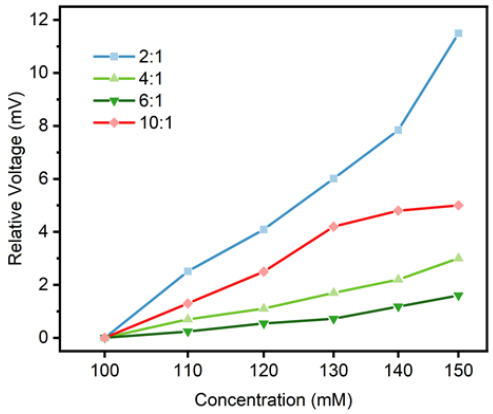

Figure 5.1.4 The sodium sensing performance of TEFS with different weight ratios of CNTs. 2:1, 4:1, 6:1, and 10:1 refer to the weight ratio of PLA to CNTs.

5.1.3 Interlayer

As formerly indicated (Figure 5.1.3 A), numerous holes form in the PLA/CNTs transducer layer. Despite the secure connection between the liquid metal and CNTs, the vast holes would allow water to suffuse across the membrane and thus enter and react with the liquid metal, causing liquid metal's irreversible oxidation and polarization. Therefore, the holes in the membrane pose a considerable challenge to the long-term stability of the TEFiber in aqueous conditions. Furthermore, even though we treat the transducer mixture with ultrasonic and stirring, the CNTs still exhibit extreme intention to aggregate, inhibiting the membrane's even coating and the electrical performance.

We added the second water-repelling encapsulation layer to tackle the challenges: PTFE/PFPE/CNTs interlayer between the transducer layer and liquid metal. PTFE (Polytetrafluoroethylene) is widely used for its extraordinary chemical inertness, and

PFPE (Perfluoropolyether) is a reliable lubricant. The mixture of these two hydrophobic materials exhibits a highly viscous and dense property, which is ideal for the water-repelling interface. The viscous mixture can form a physical isolation layer between CNTs, effectively preventing direct contact and aggregation between CNTs. This physical isolation layer can reduce van der Waals forces between CNTs, thereby reducing aggregation. Besides, the viscosity of the PTFE and PFPE mixture can increase the flow resistance of CNTs in the mixture, and this increased resistance can slow the movement and aggregation of CNTs. In addition, the viscous mixture can also redisperse the aggregated CNTs through its fluidity.

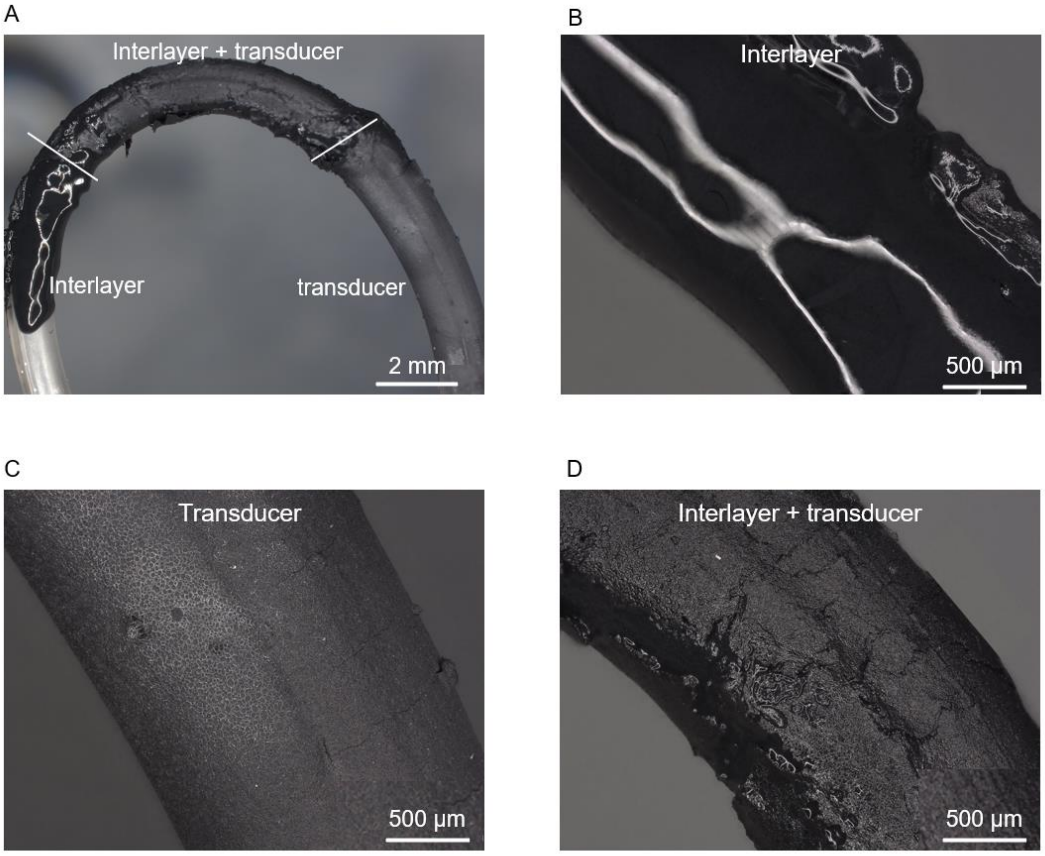

Figure 5.1.5 (A) The morphology comparison of the interlayer, transducer, and the combination of interlayer with transducer. (B) Zoomed-in morphology of interlayer. (C) Zoomed-in morphology of transducer. (D) Zoomed-in morphology of interlayer + transducer.

The need for implantable sensors that can maintain stability while under bending, due to the flexible nature of patients' tissues and organs, is a critical consideration. The stability of structure and interface among parts of devices holds great importance in realizing sensing stability. We compared the morphology of electrodes before and after bending the transducer-EGaIn fiber sensor (TEFS) and transducer-interlayer-EGaIn fiber sensor (TIEFS). The cracks in Figure 5.1.6 A come from the CNTs, which are easy to congregate, while the cracks grow larger in Figure 5.1.6 B, meaning there is an inconsistency of TEFS under deformation.

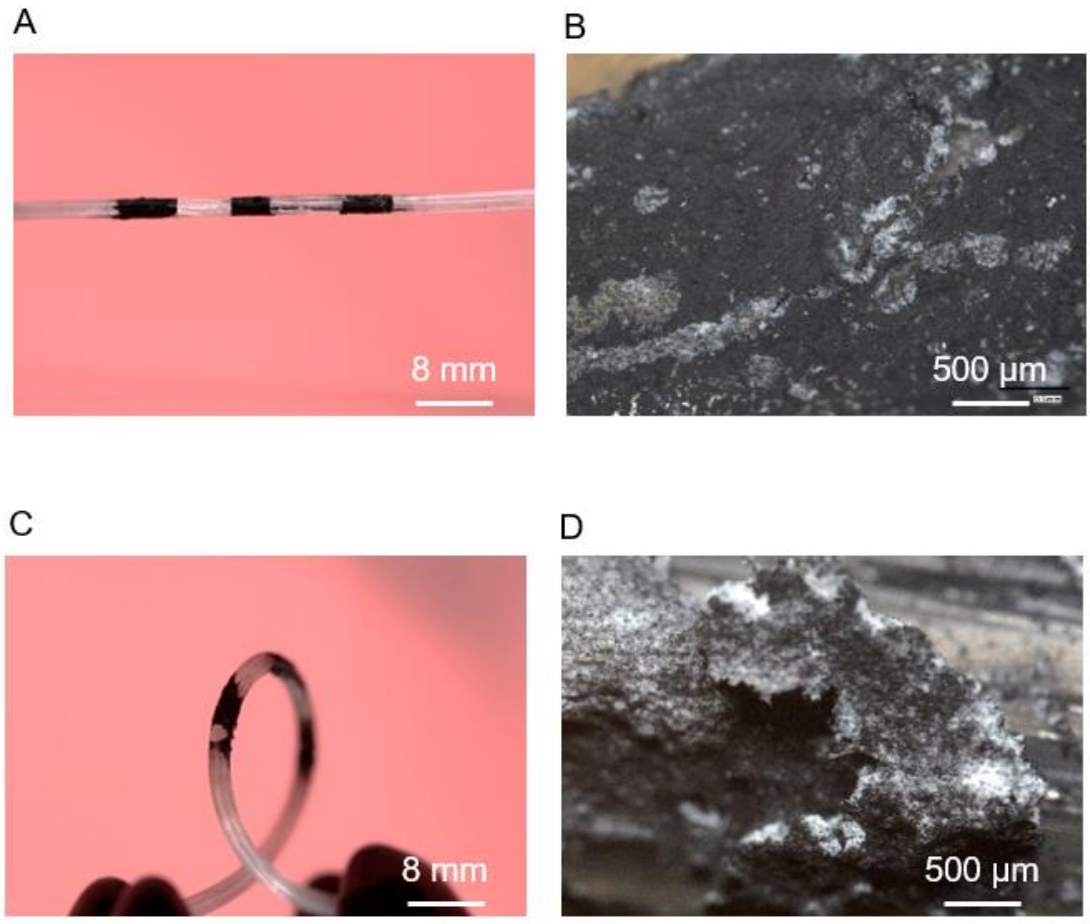

Figure 5.1.6 The bending test of TEFS. (A, B) Morphology of TEFS before bending. (C, D) Morphology of TEFS after bending.

On the contrary, the morphology of the electrodes of TIEFS remains consistent and unchanged before and after bending, as depicted in Figure 5.1.7. The addition of an

interface significantly reduced the formation of cracks and kept the original morphology after bending.

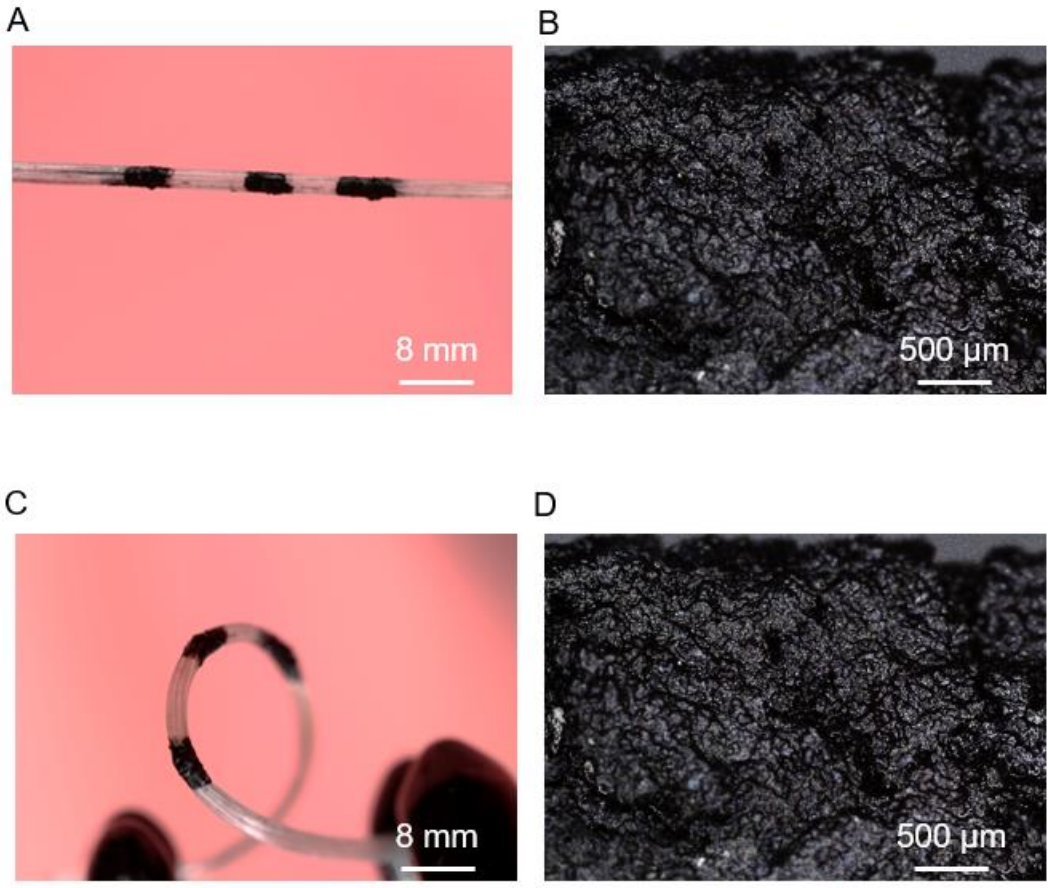

Figure 5.1.7 The bending test of TIEFS. (A, C) Morphology of TIEFS before bending. (B, D) Morphology of TIEFS after bending.

The anti-friction performance is vital for implantable devices because of the undeniable frictional process with organs or tissues during implantation. We also tested the anti-abrasion performance of TEFS (transducer-EGaIn fiber sensor) and TIEFS (transducer-interlayer-EGaIn fiber sensor). Under being scratched with sandpapers from #5000 to #80 three times each, the CNTs on the TEFS electrode fall off easily, even after being scratched using the finest sandpaper, as shown in Figure 5.1.8 A, B. However, the CNTs on the TIEFS electrode keep consistency even after being scratched by the roughest sandpaper, which can be observed from Figure 5.1.8 C, D —the anti-abrasion

performance of TIEFS benefits from the hierarchical structure of the wet interlayer and dry transducer. When being scratched, the PFPE in the interlayer is able to self-heal, and the oily interface allows CNTs to realign like skiing during deformation. This dynamic realign assures the electrochemical performance of TIEFS during deformation. Compared to TEFS in Figure 5.1.9 C, D, the resistance of TIEFS under bending and scratching keeps minimal change, which assures the functionality of TIEFS during implantation.

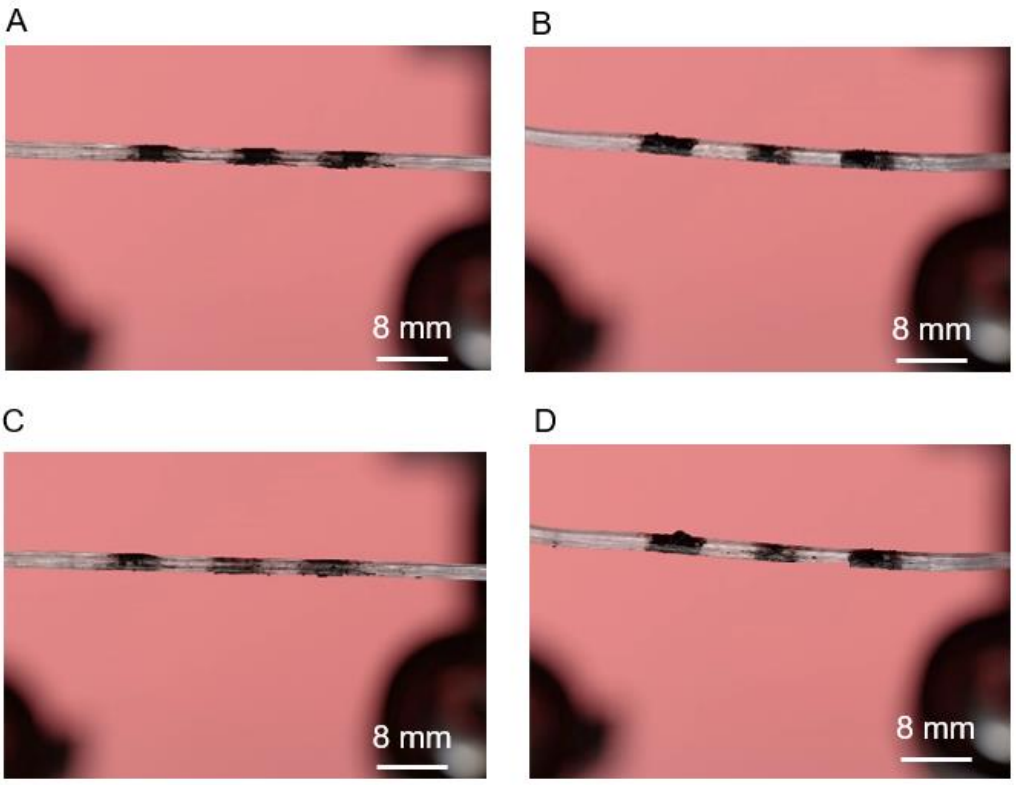

Figure 5.1.8 (A) The morphology of TEFS before scratching. (B) The morphology of TIEFS before scratching. (C) The morphology of TEFS after three times of scratching with #800 sand paper. (D) The morphology of TIEFS after three times of scratching with #800 sand paper.

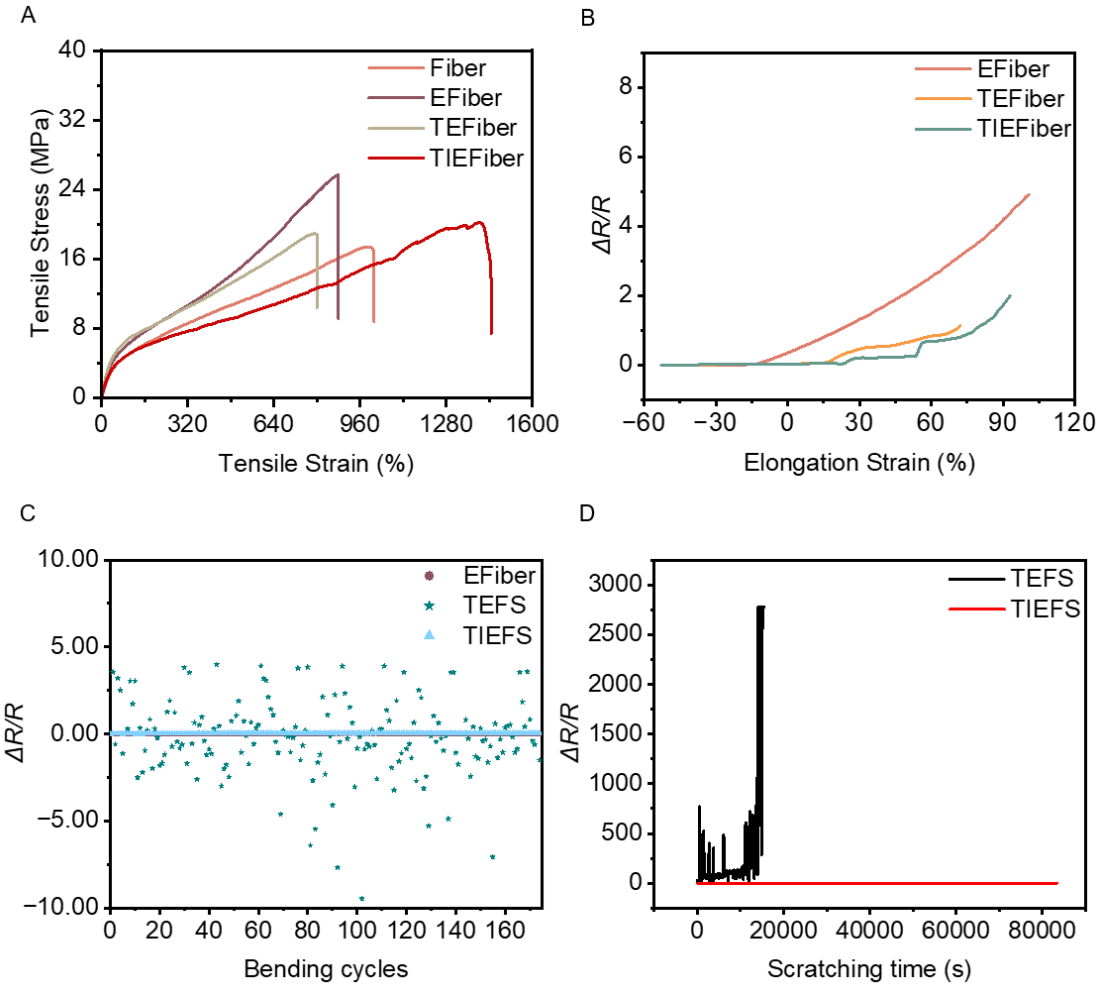

Figure 5.1.9 (A) The tensile strength of fiber, EFiber, TEFiber, and TIEFiber. (B) The resistance changes of ETFiber, TEFiber, and TIEFiber under bending and elongation. (C) The change of resistance of EFiber, TEFS, and TIEFS under bending. (D) The change of resistance of TEFS and TIEFS under scratching.

Based on the lubricant characteristic, the contact angle between the water and interlayer is smaller than that of the transducer layer, 96.210^{o} and 133.996^{o}, respectively. The contact angle between the water and transducer layer with interface acts as a middle value, 128.785^{o} between the above two. The coating remains hydrophobic, which is optimistic for preventing biofouling of in vivo implantation.

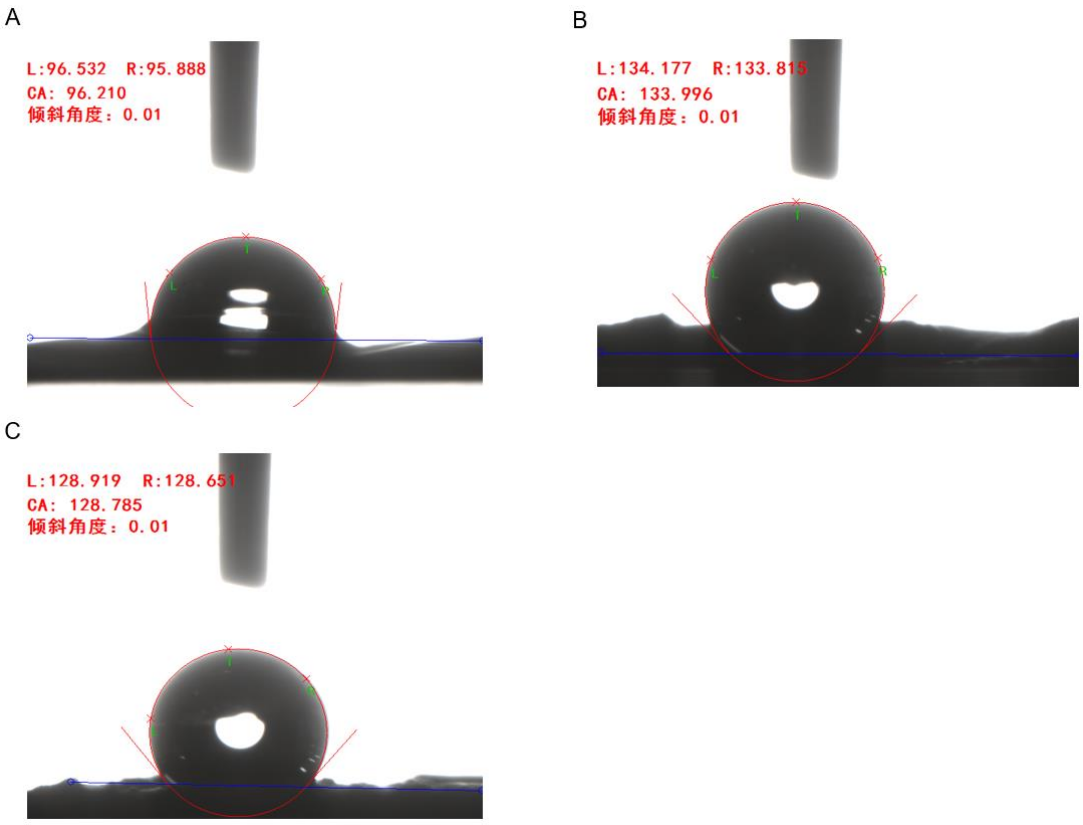

Figure 5.1.10 The contact angle between water and (A) interlayer; (B) transducer without interlayer; (C) transducer with interlayer.

5.2 Capacitive Performance of Transducer-Interlayer-EGaIn Fiber (TIEFiber)

CNTs have been found to have capacitive performance for years and have been applied to various sensing scenarios[169, 170]. Here, we also studied the capacitive performance of TIEFiber and IEFiber. The porous structure of the transducer gives water in solution access to a reaction with liquid metal, which results in a diagonal line of TEFiber in the CV test, showing no capacitive performance. However, the addition of an interlayer prohibits the passage of water into contact with liquid metal. Hence, the CV curve of TIEFiber (Figure 5.2.1 B) shows a square wave, presenting the capacitive performance. The two semicircles in the Nyquist plot of TIEFiber (Figure 5.2.1 C) indicate that there

is a resistor and two capacitors in series in the circuit and that the two capacitors are each in parallel with a resistor as shown in Figure 5.2.1 A (down). The drop in impedance at mid-frequency and high frequency in the Bode plot (Figure 5.2.1 D) and the two peaks of the phase angle at the response frequency also match this circuit. Therefore, we can infer that the TIEFiber consists of two separate capacitors.

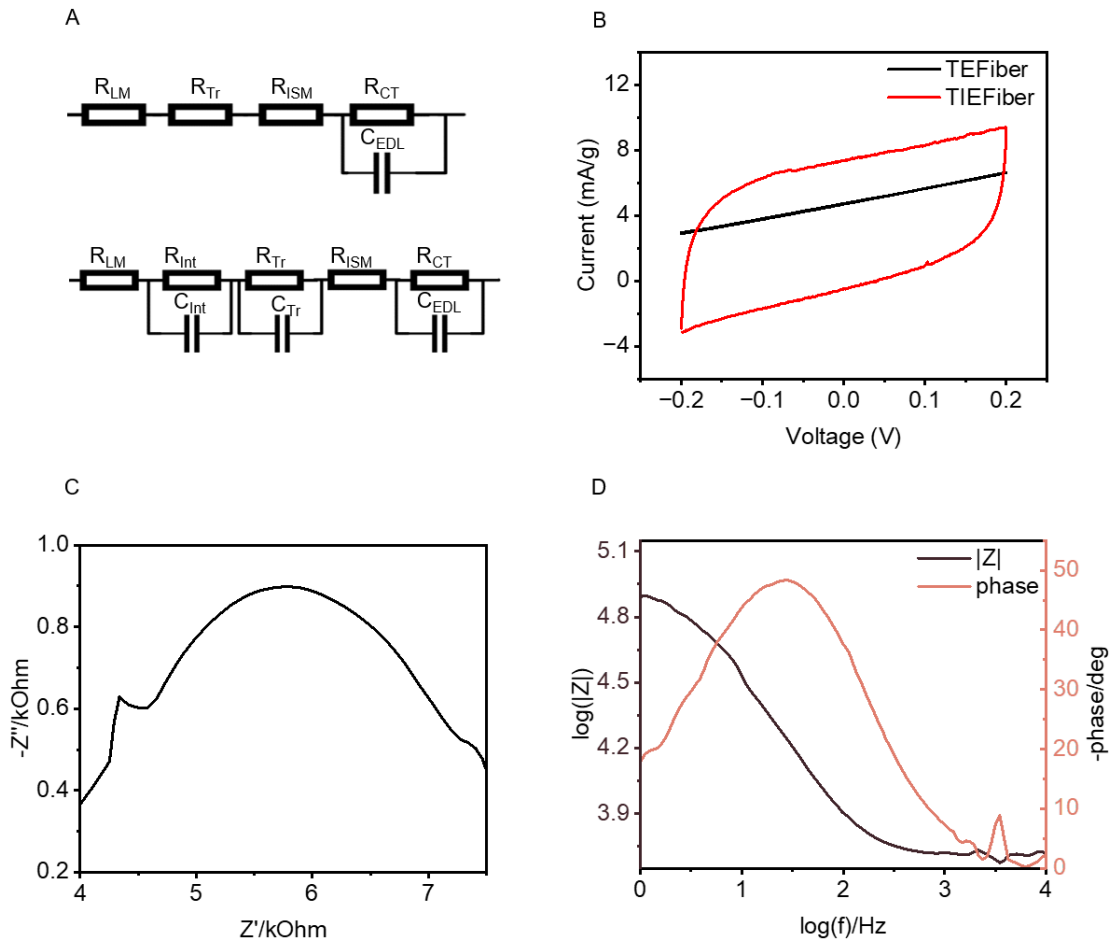

Figure 5.2.1 (A) The electrical circuit of TEFS (up) and TIEFS (down). R_{LM}: the resistance of liquid metal. R_{Tr}: the resistance of the transducer. R_{ISM}: the resistance of ion selective membrane. R_{CT}: the resistance of charge transfer. C_{EDL}: the capacitance of the electrical double layer. R_{Int}: the resistance of interlayer. C_{Int}: the capacitance of interlayer. (B) The CV curve of TEFiber and TIEFiber. (C) Nyquist plot of the electrical circuit of TIEFiber. (D) The Bode magnitude and phase angle plot of the electrical circuit of TIEFiber.

Our research has uncovered a novel aspect of TIEFiber performance. We found that CNTs, as the main contributors to the capacitive performance of TIEFiber, exhibit a unique behavior. We measured the capacitance of TIEFiber with different masses of CNTs, which means only changing the mass of the interlayer. When the mass of CNTs is less than 15mg, the capacitance value is directly proportional to the mass of CNTs. However, when the mass of CNTs exceeds 15mg, the capacitance value stabilizes at around 230μF. The capacitance of CNTs can be calculated as follows:

$$C = \frac{S}{d}\varepsilon$$

Where C refers to the capacitance of CNTs, S refers to the surface area of CNTs, d refers to the distance among CNTs, and ε refers to the permittivity of CNTs. The surface area of CNTs is proportional to the mass of CNTs. The increasing mass of CNTs leads to the growth of the capacitance of CNTs. However, when the mass of CNTs is greater than 15 mg, the distance among CNTs becomes large enough to offset the positive impact of the increase in mass, so the capacitance value remains roughly constant. We also measured the capacitance value with and without the transducer, which shows that adding the transducer increased the capacitance value to 10 folds. The reason is that compared to the interlayer, the mass ratio of CNTs in the transduction layer is more extensive, and the distance between CNTs is closer.

In an electrical circuit, the charge on the capacitor can be calculated as follows:

$$Q = CU$$

Where Q refers to the charge on the capacitor, C refers to the capacitance, and U refers to the voltage applied to the capacitor. In the electrical circuit of the TIEFS, depicted in Figure 5.2.1 A, when voltage is transferred from the ion-selective membrane (ISM) to the transducer, the high transducer capacitance in Figure 5.2.2 B results in a substantial

charge accumulation. This charge is subsequently transmitted to the interlayer, producing an amplified voltage output. Consequently, the voltage transferred from the ISM to the interlayer is significantly enhanced[171].

We conducted an open-circuit voltage test to validate our hypothesis. By coating the sodium ion-selective membrane onto the TIEFiber, we fabricated the sodium sensor TIEFS (transducer-interlayer-EGaIn fiber sensor), which demonstrated a response via open-circuit voltage. We also assessed the selectivity of TIEFS with varying masses of carbon nanotubes (CNTs). Our results show that when the CNTs mass was below 15 mg, sensitivity increased proportionally with the CNTs mass. However, when the CNT mass exceeded 15 mg, the sensitivity stabilized at approximately 220 mV/decade, aligning with the capacitance performance of the TIEFiber across different CNT masses. We chose 8 mg of CNTs in the following experiments for convenient operation.

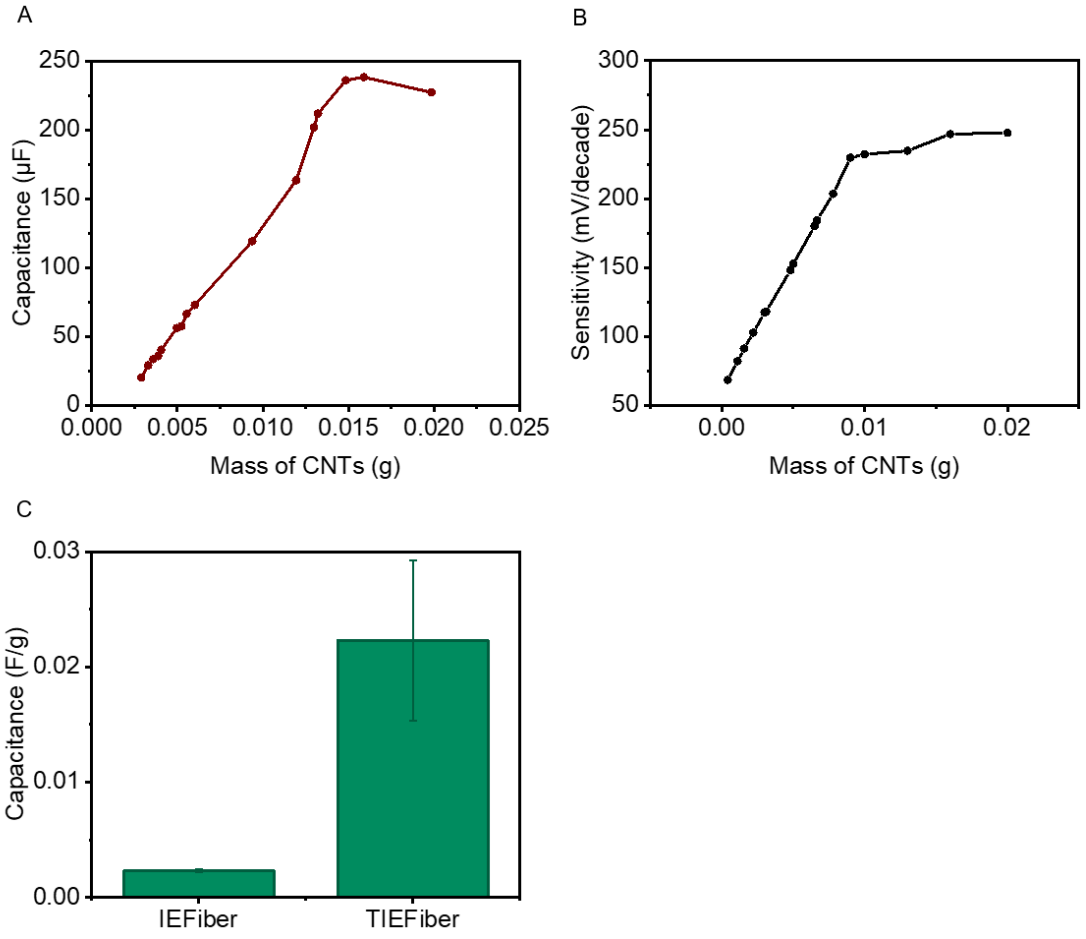

Figure 5.2.2 (A) The capacitance of TIEFiber with different masses of CNTs. (B) The sensitivity of sodium TIEFS with different masses of CNTs. (C) The capacitance value of IEFiber and TIEFiber.

5.3 Sensing Performance of Fiber-shaped Sensor (TIEFS)

We further investigated the sodium sensing performance of the TIEFS and compared the influence of interface on sodium sensing. Both fiber sensors exhibit a reliable linear response to the variation in sodium concentration, as depicted in Figure 5.3.1. The sensitivity of the two sensor types is 62 mV/decade and 147 mV/decade, respectively. Our results underscore the potential of an interface to enhance sensitivity.

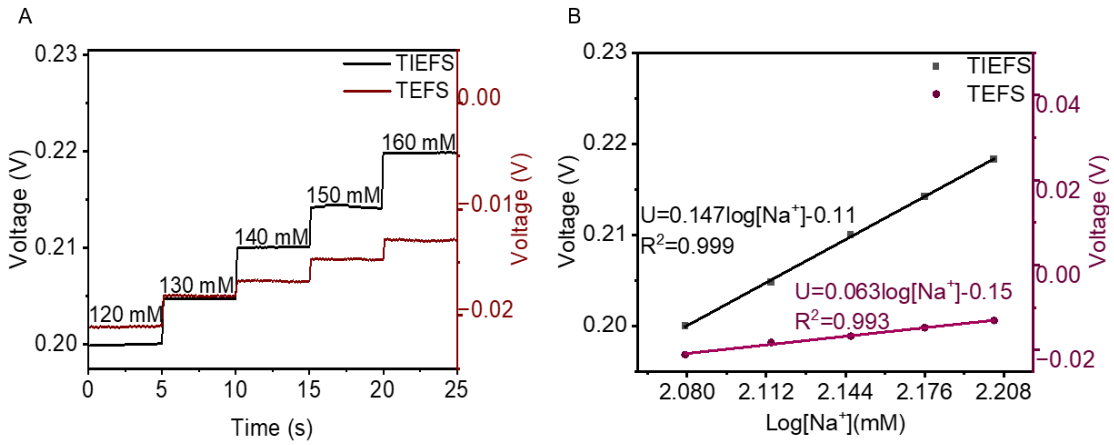

Figure 5.3.1 (A) The sensitivity of sodium TIEFS to sodium concentration ranged from 120 mM to 160 mM. (B) Corresponding calibration plot of sodium TIEFS.

We also probed the resolution of sodium TIEFS and potassium TIEFS, as shown in Figure 5.3.2, finding that the former is 500 μM, while the latter is 100 μM. The resolution of sodium TIEFS is 500 μM, while potassium TIEFS is 100 μM. The resolution of both sensors satisfies the requirements of clinical application.

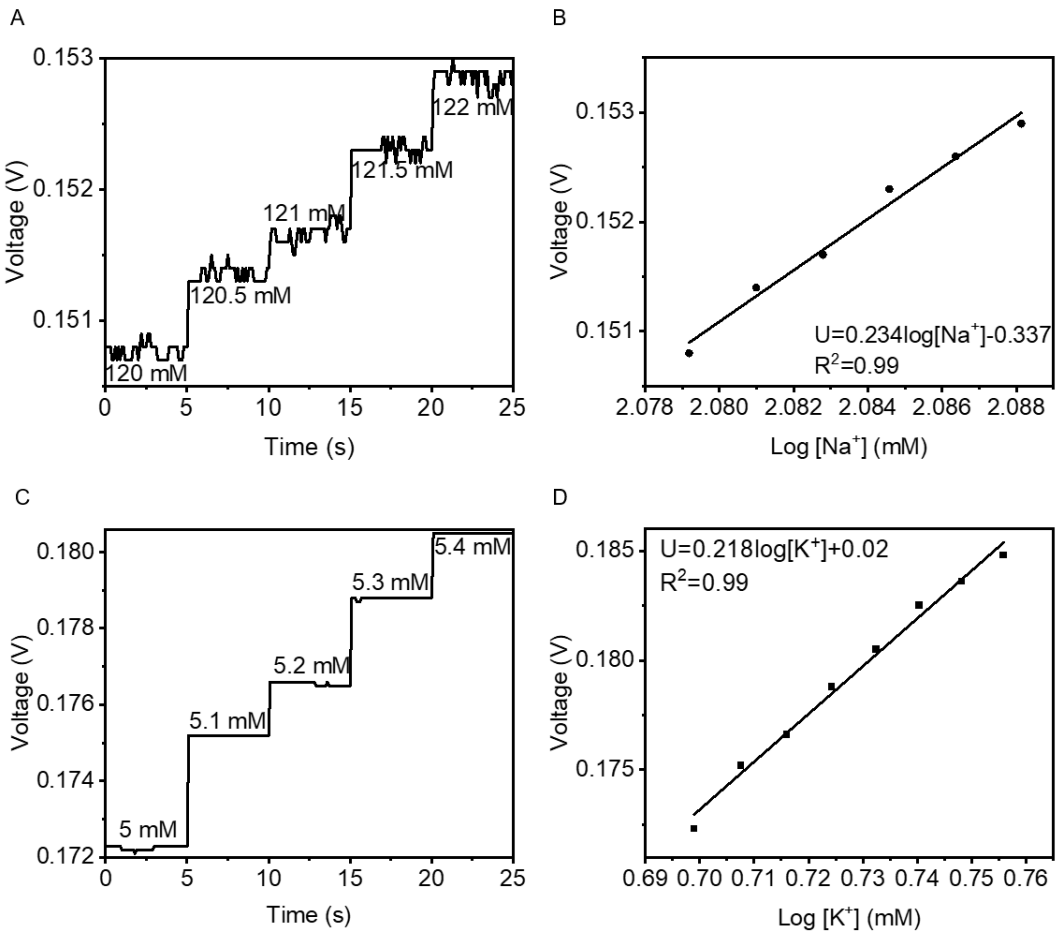

Figure 5.3.2 (A) The resolution of sodium TIEFS to sodium concentration ranged from 120 mM to 122 mM. (B) The corresponding calibration plot of sodium TIEFS. (C) The resolution of potassium TIEFS to potassium concentration ranged from 5 mM to 5.4 mM. (D) The corresponding calibration plot of potassium TIEFS.

Compared with other related research on sodium sensors using the open circle voltage method, as shown in Figure 5.3.3 A, we can find out that our TIEFS obtains a high sensitivity while keeping a relatively low device size. The sensitivity-amplification situation does not only exist on sodium sensors. We also fabricated glucose sensors that utilize amperometry as a testing method and compared the sensitivity between glucose TIEFS and glucose TEFS in Figure 5.3.3 C, D. Based on the exact size of the two kinds of fiber sensors, the sensitivity of the fiber sensors increased from 0.0001 μA/μM to 0.038 μA/μM because of the addition of the interface. This result proved that the universal fabrication method fits both voltage and current measures.

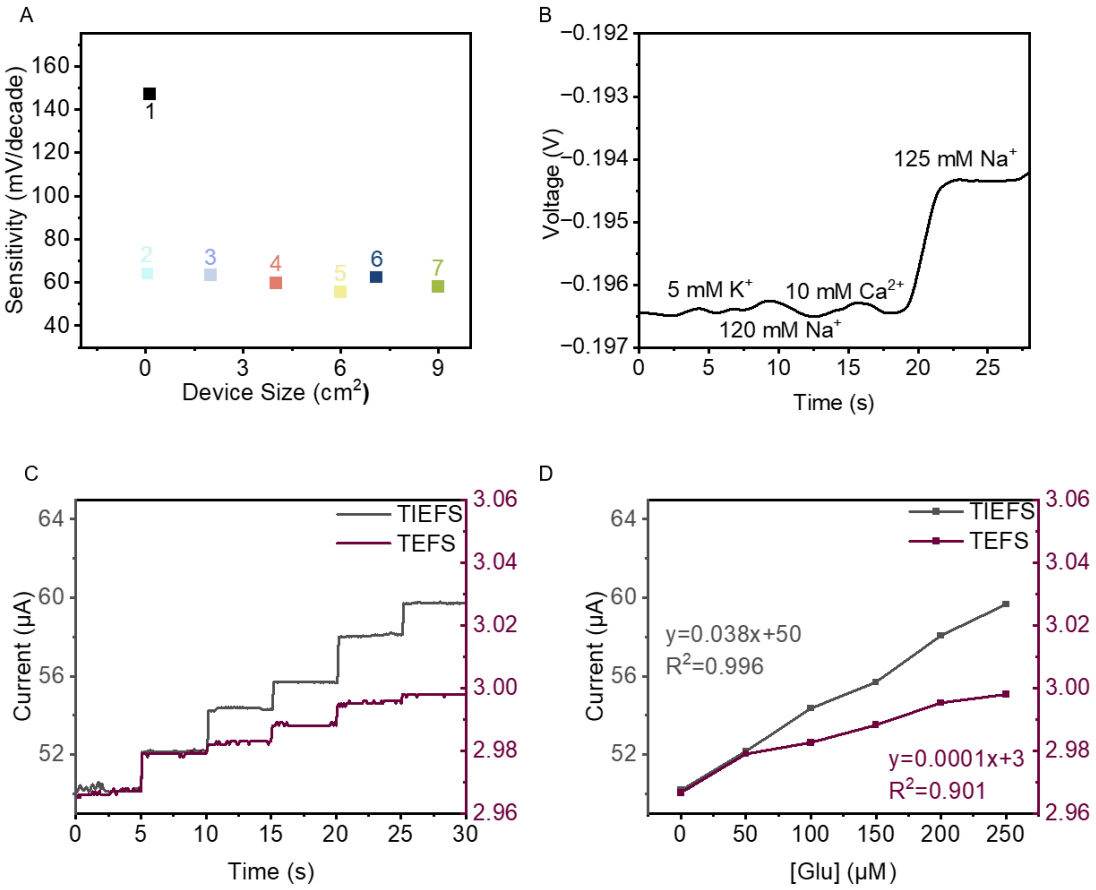

Figure 5.3.3 (A) The sodium sensor sensitivity of recent works. 1: our work. 2: ***Sci. Rep.,*** 2024, **14,** 11526[172]. 3: ***Electroanalysis,*** 2019, **31,** 239-245[173]. 4: ***Sens. Actuators B Chem.,*** 2021, **331,** 129416[174]. 5: ***Nat. Electron.,*** 022, **5,** 694–705[175]. 6: ***Anal. Chem.,*** 2020, **92,** 4647-4655[176]. 7: ***ACS Appl. Mater. Inter.,*** 2017, **9**, 35169-35177[177]. (B) The selectivity of sodium TIEFS. (C) The sensitivity of glucose TIEFS to glucose concentration ranged from 0 μM to 250 μM. (D) Corresponding calibration plot of glucose TIEFS.

We delved into the comprehensive evaluation of sodium TIEFS's properties, focusing on its reversible sensing performance, selectivity, repeatability, and reproducibility. These characteristics are crucial for the sensor's application in monitoring fluctuating ion levels in patients' bodies and for potential mass production. The sodium TIEFS demonstrates a highly favorable reversible sensing performance, essential for applications requiring continuous monitoring of sodium ion concentrations. As

depicted in Figure 5.3.3 B, the sodium TIEFS exhibits high selectivity against common interfering ions such as potassium and calcium. This selectivity is achieved through the ion selective membrane, which preferentially binds to sodium ions over other cations. Distinguishing sodium ions from potassium and calcium is vital in physiological environments, where these ions coexist and can potentially interfere with accurate sodium measurement. The sodium TIEFS's repeatability is illustrated in Figure 5.3.4 A, where consistent sensing performance is observed across multiple cycles of ion concentration changes. This repeatability indicates TIEFS's robustness and reliability in dynamic environments, such as those found in the human body. TIEFS's ability to maintain consistent performance despite fluctuations in ion levels underscores its potential for real-time monitoring applications. This characteristic is particularly valuable in clinical settings, where patients' ion levels can vary significantly due to physiological processes or medical interventions.

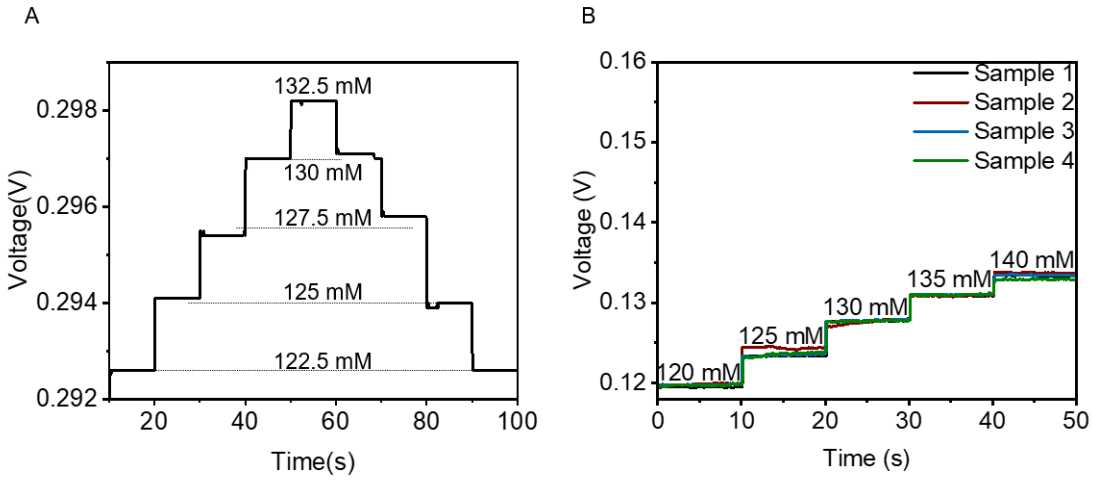

Figure 5.3.4 (A) The repeatability of sodium TIEFS to sodium concentration ranged from 122.5 mM to 132.5 mM. (B) The reproductivity of sodium TIEFS to sodium concentration ranged from 120 mM to 140 mM.

The reproducibility of the sodium TIEFS, as shown in Figure 5.3.4 B, highlights its potential for large-scale manufacturing. Reproducibility refers to the sensor's ability to

deliver consistent performance across different production batches. This property ensures that each sensor unit meets the same quality standards, which is essential for widespread clinical adoption. The reliable reproducibility of the sodium sensor is achieved through optimized fabrication processes and stringent quality control measures. This consistency facilitates mass production and ensures that TIEFS can be deployed in diverse healthcare settings without compromising performance.

We explored the critical aspect of sensing fidelity in sodium TIEFS when subjected to mechanical deformation. This evaluation is essential for understanding TIEFS's performance in real-world applications, particularly in dynamic environments requiring flexibility and durability. The ability of implantable sensors to maintain accurate sensing under deformation is a significant performance metric. To assess this, we conducted experiments to evaluate the sodium TIEFS's performance while bent. The sensor was subjected to incremental bending, with sodium concentration changes every 10 degrees, as depicted in Figure 5.3.5 A. The results demonstrated that the potential response of the sodium TIEFS remained consistent when the sodium concentration was held constant. This consistency indicates that the electrochemical properties of the sodium TIEFS are remarkably stable during deformation, underscoring its robustness and reliability for applications where the sensor may experience bending or flexing. In addition to stability under deformation, the sodium TIEFS exhibited a linear response to changes in sodium concentration. This linearity is crucial for accurately quantifying sodium levels in various scenarios, highlighting the sensor's potential for practical applications. The ability to provide a predictable and proportional response to concentration changes ensures that the sodium TIEFS can be effectively used in environments where precise monitoring of sodium levels is necessary, such as in medical diagnostics and patient monitoring.

To further evaluate the durability of the sodium TIEFS, we tested its sensing performance before and after undergoing multiple bending cycles—specifically, after

10, 50, and 100 bending iterations, as shown in Figure 5.3.5 B. The sensor maintained similar sensing performance after ten bending cycles, demonstrating the stability of its structure and electrochemical properties under initial deformation. This resilience indicates the sensor's robust design, which can withstand mechanical stress without compromising functionality. However, after 50 and 100 bending cycles, a slight degradation in sensing performance was observed. Despite this, the sodium TIEFS continued to deliver satisfactory responses, indicating that while prolonged mechanical stress may impact performance, the sensor retains functionality that remains useful for many applications. This finding suggests that the sodium TIEFS is well-suited for scenarios requiring moderate flexibility and durability, although further optimization may be needed for applications involving extensive mechanical deformation.

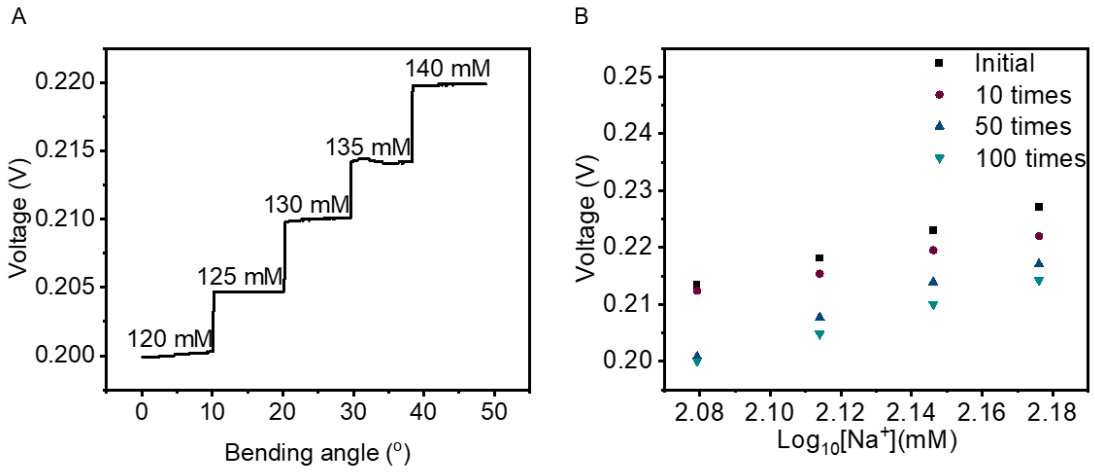

Figure 5.3.5 (A) The sensitivity of sodium TIEFS under bending to sodium concentration ranged from 120 mM to 140 mM. (B) The sensing performance of sodium TIEFS before and after 10, 50, and 100 bending times

We also evaluated the storage fidelity of TIEFS and its multi-dimensional performance relative to other existing technologies. The long-term stability of sodium TIEFS was rigorously compared with that of sodium TEFS, as illustrated in Figure 5.3.6 A. The sodium TEFS exhibited a higher noise ratio and potential drift over extended periods,

which can compromise the accuracy and reliability of ion measurements. In contrast, the sodium TIEFS, enhanced with an interface layer, demonstrated significantly reduced noise and stabilized potential signals. This improvement is attributed to the interface's excellent water resistance and stability, effectively mitigating environmental fluctuations and enhancing signal fidelity. The interface acts as a protective barrier, ensuring consistent sensor performance even under prolonged exposure to aqueous environments. To assess the long-term storage fidelity of sodium TIEFS, we conducted an experiment where the sensors were immersed in a sodium chloride solution for several days. The sensing performance was evaluated before and after 3 and 7 days of soaking, as shown in Figure 5.3.6 B. The results indicate that the sodium TIEFS maintained its sensing capabilities with minimal degradation over time. This stability is crucial for practical applications, where sensors may need to be stored for extended periods before use. The ability to retain performance after prolonged storage underscores the robustness of the TIEFS design and its suitability for real-world deployment.

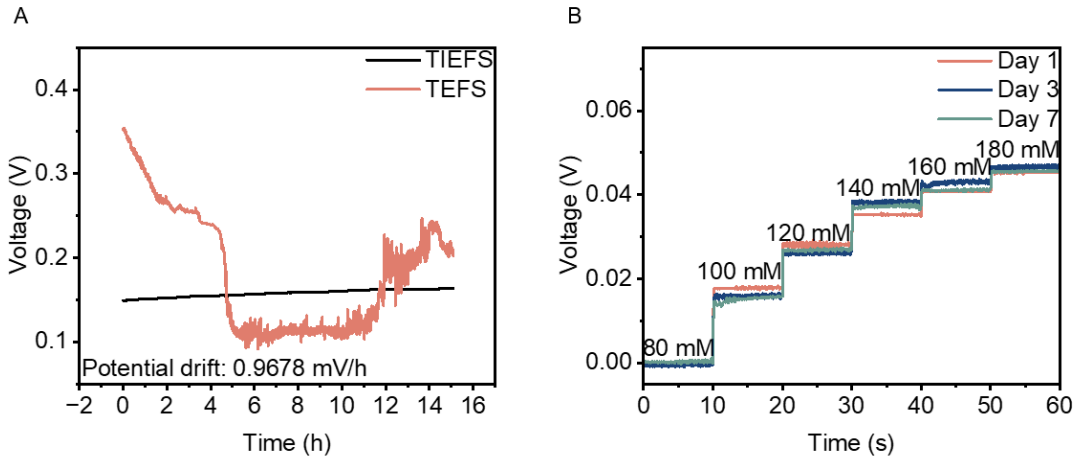

Figure 5.3.6 (A) The long-term sensing stability of sodium TIEFS and TEFS for 120 mM sodium aqueous solution in 15h. (B) The long-term sensing performance of sodium TIEFS before and after 3 and 7 days of soaking into sodium solution to sodium concentration ranged from 80 mM to 180 mM.

In addition to stability assessments, we conducted a comprehensive evaluation of the sodium TIEFS's performance across multiple dimensions, comparing it with other existing sensor technologies. Figure 5.3.7 presents this comparison, which includes metrics such as device size, Young's modulus, tensile strength, signal drift, resolution, sodium sensitivity, and glucose sensitivity. TIEFS demonstrated superior performance across all seven dimensions. Its compact size and favorable mechanical properties, such as Young's modulus and tensile strength, make it ideal for integration into flexible and wearable devices. Furthermore, TIEFS exhibited minimal signal drift and high resolution, ensuring precise and reliable measurements. The enhanced sodium and glucose sensitivity further highlight the sensor's versatility and potential for multi-analyte detection in complex biological environments.

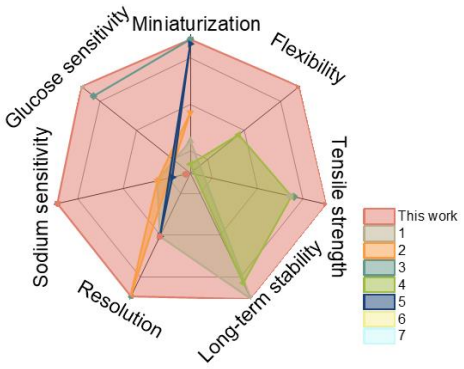

Figure 5.3.7 Sensor performance of recent works. 1: ***Electroanalysis,*** 2016, *28*, 1267-1275[178]. 2: ***ACS Sens***. 2020, 5, 2834–2842[179]. 3: ***Anal. Chem.*** 2019, 91, 6569–6576[180]. 4: ***Chem. Eng. J.*** 2023, 454, 140473[181]. 5: ***Adv. Funct. Mater.*** 2018, 28, 1804456[182]. 6: ***Adv. Funct. Mater,*** 2022, 32, 2200922[183]. [184]. 7: ***Anal. Chem.*** 2021, 93, 16222–16230[185].

5.4 Multi-functional Fiber-shaped Sensor (TIEFS)

Building upon the successful verification of single-functional TIEFS, we advanced our research by fabricating a three-electrode TIEFS system. This system comprises two

working electrodes—a sodium-selective electrode and a potassium-selective electrode—alongside a reference electrode. Integrating multiple electrodes within a single sensor unit aims to enhance its functionality by enabling simultaneous detection of multiple ions, which is crucial for comprehensive physiological monitoring.
As discussed in Chapter 2, the distance between electrodes significantly influences the electrochemical characteristics of multi-functional sensors. Variations in this distance can affect the sensor's impedance and overall performance. Besides, during implantation, friction, and deformation may alter the interelectrode spacing, potentially impacting the sensor's stability and accuracy.

To investigate this, we measured the impedance between the working electrodes and the reference electrode while varying the interelectrode distance from 2 mm to 12 mm, as illustrated in Figure 5.4.1 A. The results revealed minimal variation in impedance across different interelectrode distances, indicating that electrical crosstalk is negligible in the three-electrode TIEFS. This finding suggests that the sensor design effectively mitigates potential interference between electrodes, ensuring stable performance even when the physical configuration changes slightly during implantation.

We further evaluated the simultaneous sensing capabilities of the three-electrode TIEFS by conducting a dynamic test. In this experiment, we first altered the potassium concentration for the initial 70 seconds, followed by a change in sodium concentration for the subsequent 70 seconds, as depicted in Figure 5.4.1 B. During the first phase, the potassium-selective electrode responded to the concentration change, while the sodium-selective electrode's voltage remained constant. Conversely, in the latter 70 seconds, the sodium selective electrode exhibited a voltage change corresponding to the variation in sodium concentration, while the potassium electrode's voltage remained unchanged. Each electrode's distinct and independent response to its target ion demonstrates the sensor's ability to monitor multiple ions accurately and simultaneously without cross-

interference. Such performance is critical for real-time monitoring applications where multiple physiological parameters need to be tracked concurrently.

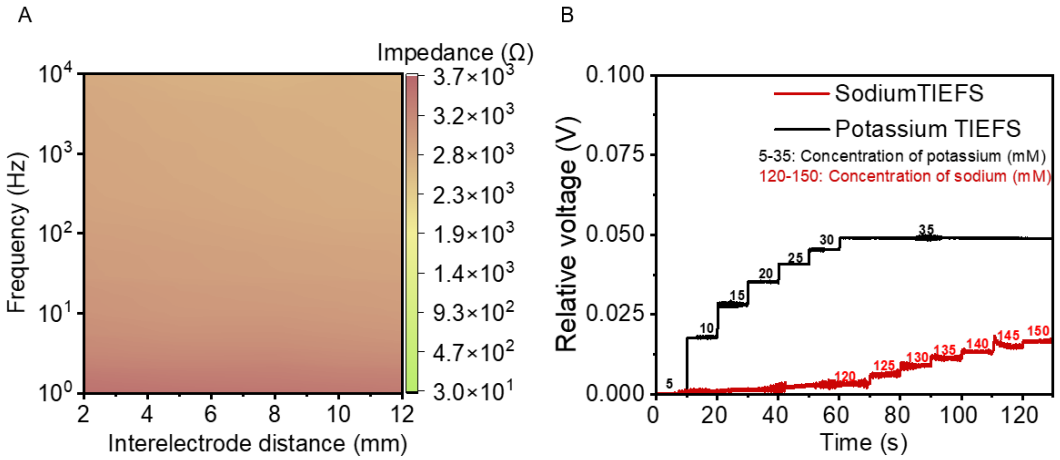

Figure 5.4.1 (A) The impedance change between the reference electrode and the working electrode with different 'interelectrode distances ', which refers to the distance between the two electrodes of sodium TIEFS. (B) The simultaneous sensing to sodium and potassium aqueous solution of TIEFS.

We present a comprehensive evaluation of TIEFS's biocompatibility, focusing on its interaction with biological tissues and their potential for safe implantation. This assessment is crucial for determining its suitability for long-term use in biomedical applications.

To assess the biocompatibility of TIEFS, we conducted an in vivo study by implanting the sensors into the muscle tissue of Sprague-Dawley (SD) rats for 7 days. Following the implantation period, the tissues were harvested and subjected to histological examination using Hematoxylin and Eosin (H&E) staining, as illustrated in Figure 5.4.2 A. The histological analysis revealed a minimal infiltration of polymorphonuclear leukocytes, lymphocytes, and plasma cells around the implant material. Additionally, a small number of giant cells and a more significant number of multinucleated giant cells were observed, as shown in Figure 5.4.2 D. These cells indicate a mild inflammatory

response, which is a common reaction to foreign materials. Furthermore, the formation of a small amount of new blood vessels was noted, suggesting a degree of tissue integration and healing around the implant site. Overall, the TIEFS exhibited a slight but acceptable reaction to the muscle tissue compared to the control sample, indicating a highly favorable biocompatibility profile, which bodes well for its potential in biomedical applications.

In addition to the in vivo assessment, we conducted in vitro tests to evaluate the cytotoxicity and hemolytic potential of TIEFS. The cell toxicity assay, depicted in Figure 5.4.2 B, demonstrated that TIEFS exhibited low cytotoxicity, indicating that the material does not adversely affect cell viability, which is critical for ensuring that the sensor does not induce harmful effects on surrounding tissues upon implantation. The hemolysis assay, shown in Figure 5.4.2 C, further supported the biocompatibility of TIEFS by demonstrating no significant hemolytic reaction. The absence of hemolysis indicates that the sensor material does not cause the destruction of red blood cells, which is essential for preventing adverse systemic effects when the sensor is in contact with blood.

The biocompatibility evaluation of TIEFS unequivocally indicates that the sensor is suitable and safe for implantation, with minimal adverse reactions observed in both in vivo and in vitro assessments. The slight inflammatory response and the formation of new blood vessels suggest that TIEFS can integrate with biological tissues without causing significant harm. The low cytotoxicity and lack of hemolytic activity further confirm the sensor's safety for biomedical applications.

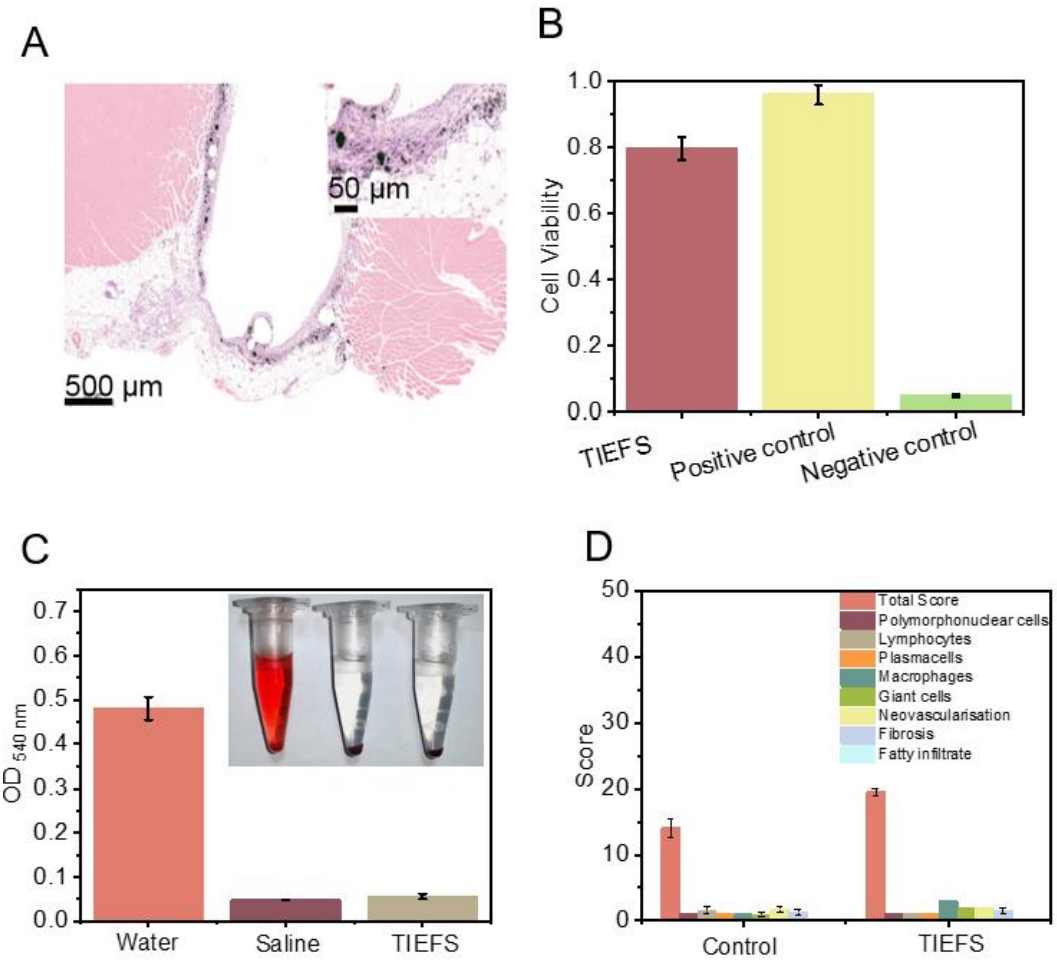

Figure 5.4.2 (A) The H&E stain of the implanted area of SD rats after 7 days of implantation. Insert image shows the area before implantation. (B) The MTT test of TIEFS. (C) The hemolysis assay of TIEFS. (H) The histological evaluation of SD rats' tissue after 7 days of implantation.

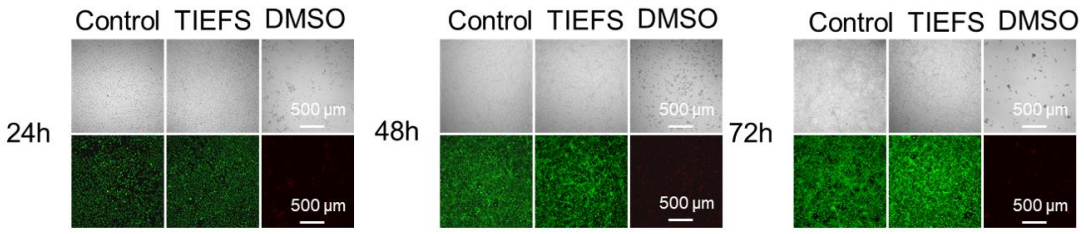

Figure 5.4.3 The cell toxicity test of TIEFS. Cell: NIH3T3.

Finally, we presented a comprehensive analysis of the long-term stability and practical application of multi-functional TIEFS in biological environments, specifically focusing

on their performance in blood samples from Sprague-Dawley (SD) rats and human cardiovascular patients.

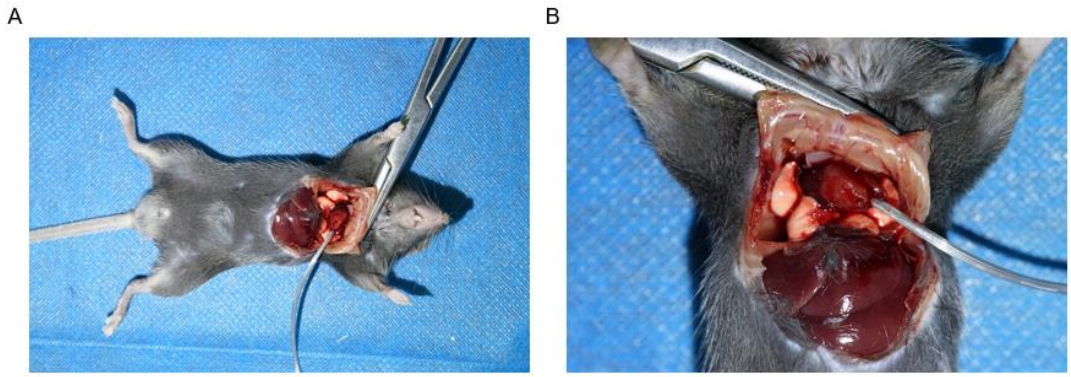

Figure 5.4.4 Multi-functional TIEFS is implanted into SD rats for sodium and potassium sensing.

To assess the long-term stability of the multi-functional TIEFS, we conducted tests in the blood of SD rats, as illustrated in Figure 5.4.4 A. The surface of the carbon nanotubes in the TIEFS is modified with carboxyl groups, which effectively inhibit protein adsorption. This modification is crucial as it prevents the fouling of the sensor surface, thereby maintaining the integrity and accuracy of the sensor signals over extended periods. The sodium and potassium TIEFS exhibited minimal signal drift during prolonged testing, demonstrating their stability and feasibility for application in blood environments. This stability is essential for reliable monitoring of ion concentrations in dynamic biological systems.

Following the successful demonstration of stability, we implanted the multi-functional TIEFS into SD rats for in vivo sensing, as depicted in Figure 5.4.3. Before implantation, the sensors were calibrated in an aqueous solution to ensure accuracy, as shown in Figures 5.4.4 B and C. The in vivo tests yielded reliable sensing results, with sodium concentrations measured at 160.67 mmol and potassium concentrations at 3.89 mmol. These values fall within the reference ranges for sodium (158-162 mmol) and potassium (3.8-4.3 mmol), confirming the sensor's accuracy and reliability in a living organism.

The ability to provide precise measurements in vivo highlights the potential of multi-functional TIEFS for real-time physiological monitoring.

To further validate the performance of the multi-functional TIEFS, we tested their ability to measure sodium and potassium concentrations in blood samples from nine cardiovascular patients in a hospital setting, as depicted in Figure 5.4.4 D and detailed in Table 5.4.1. The results obtained from the TIEFS were compared with those from commercial equipment, and the measurements were highly consistent. This consistency underscores the reliability and accuracy of the TIEFS, demonstrating their potential as a viable alternative to existing commercial technologies for blood ion analysis.

The multi-functional TIEFS exhibit excellent long-term stability and reliable performance in animal and human blood samples. The carboxyl group modification on the carbon nanotubes plays a critical role in preventing protein adsorption, ensuring stable sensor operation. The successful in vivo application in SD rats and the accurate measurement of ion concentrations in human blood samples highlight the potential of these sensors for clinical and diagnostic applications. Future research will further optimize the sensor design for enhanced durability and explore its integration into wearable and implantable devices for continuous health monitoring in diverse patient populations.

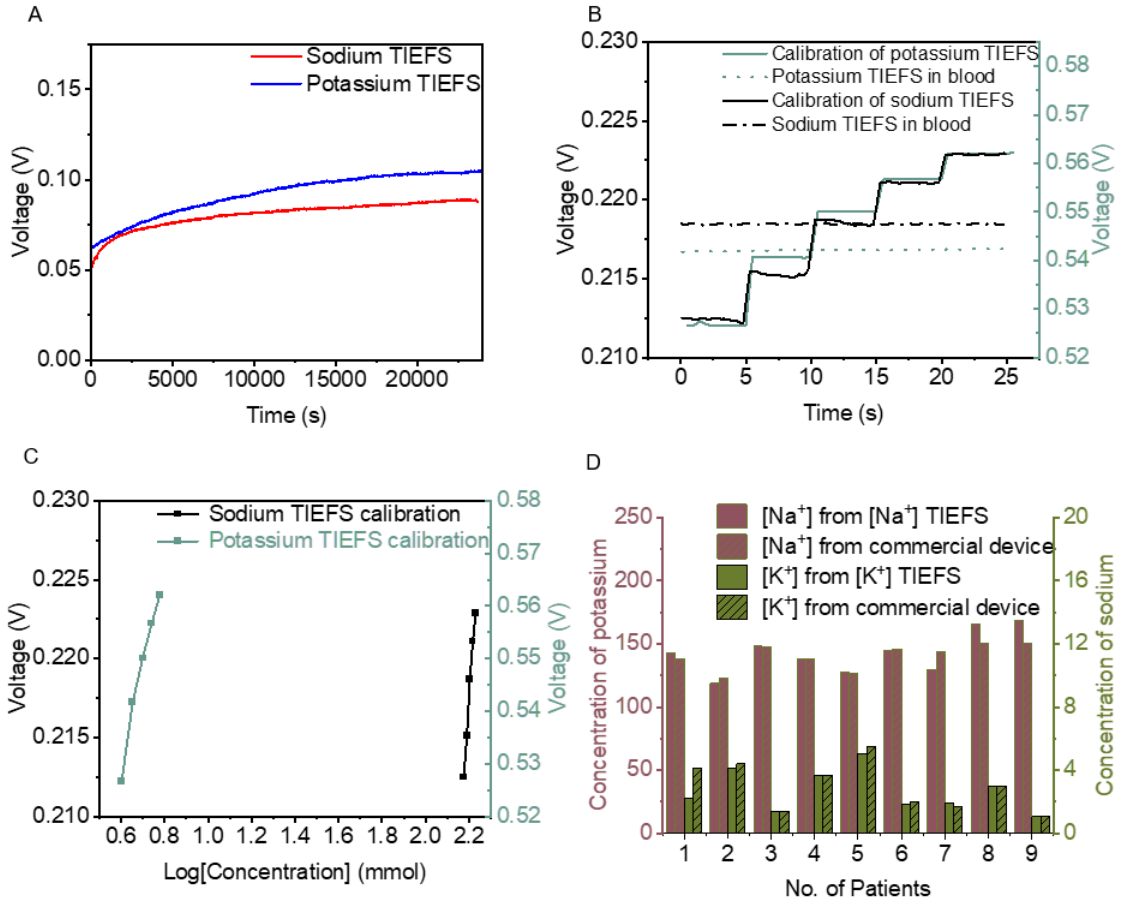

Figure 5.4.5 (A) Long-term simultaneous sensing of sodium TIEFS and potassium TIEFS in mice blood. (B) The simultaneous sensing of sodium and potassium to rats' blood of TIEFS. (C) Corresponding calibration plot of TIEFS. (D) The sensing results in 9 different human blood samples of TIEFS and commercial devices.

No. of Patient	**[Na^+] measured by [Na^+] TIEFS**	**[Na^+] measured by commercial device**	**[K^+] measured by [K^+] TIEFS**	**[K^+] measured by commercial device**
1	143.09448	138	2.20146	4.1
2	118.74429	123	4.11462	4.4
3	148.22011	148	1.37464	1.4

4	137.93957	138	3.67488	3.7
5	127.65389	127	5.05972	5.5
6	145.10038	146	1.80747	2
7	129.65382	144	1.92028	1.7
8	165.72357	150	2.99265	3
9	168.33961	150	1.05836	1.1

Table 5.4.1 The sensing result of sodium and potassium from multi-functional TIEFS and commercial equipment.

Chapter 6 Conclusion

We successfully fabricated a multi-functional flexible fiber-shaped blood biosensor TIEFS through hot extrusion in this project. The Eutectic Gallium-Indium (EGaIn) is an electrical transmission to enable flexibility. The active electrode materials are carboxylated multi-walled carbon nanotubes (CNTs) with sizeable active surface areas and high transmission rates. Through optimizing the mixture of polymer and CNTs, the biosensor TIEFS achieved extraordinary performance, including high sensitivity, resolution, long-term stability, and reliable sensing fidelity under deformation. These characteristics not only demonstrate the considerable potential of TIEFS in clinical application but also pave the way for accurate real-time blood analysis, inspiring a hopeful future for biosensor technology.

In Chapter 4, we investigated the morphology, mechanical, and electrical properties of EGaIn-filled fibers (EFiber). The low Young's modulus (0.1 MPa) of EFiber demonstrated outstanding flexibility. Besides, introducing the oily glutinous interlayer significantly increased the anti-abrasion capability and structural and electrical consistency under bending. EFiber is resistance insensitive to 124% strain. The outstanding electrical and morphological fidelity of EFiber during deformation ensured the stability of its application in dynamic environments.

In Chapter 5, we focused on the capacitive and sensing performance of the transducer-interlayer-EGaIn fiber sensor (TIEFS), which has a high sodium sensitivity of 147 mV/decade, showcasing its exceptional response to the sodium concentration change. The resolution for sodium TIEFS and potassium TIEFS is 500 μm and 100 μm, respectively, demonstrating the accuracy in sensing. Besides, the sodium TIEFS exhibits a minimal electrical signal drift for hours with 0.9678 mV/h, ensuring reliable long-term monitoring. Finally, we successfully verified the sensing performance in the

SD rats model and human blood samples, further demonstrating the feasibility of multi-functional TIEFS in clinical applications.

In conclusion, the multi-functional, implantable fiber-shaped blood gas sensor, denoted as TIEFS, was successfully fabricated with high sensitivity and fidelity in electrical and structural performance. However, the reproductivity is limited for hand-made processes in electrode fabrication, enlarging the fabrication cost. In addition, the functionality of TIEFS is only limited to electrochemical sensing. This underscores the need for future research and development in the field. The fiber-shaped sensors' fabrication method and functionality should be investigated, with a focus on improving reproductivity and expanding functionality. The morphology of the fibers can be controlled more precisely through laser cutting and photolithography. The long-term implantation biocompatibility of fiber device should be further investigated with the consideration of maintaining functionality integrity, Through integration with functional materials such as ferromagnetic and self-healing materials, the fiber-shaped sensors are desired to be capable of dynamic motion and induced deformation, broadening the application realm of fiber-shaped sensors and potentially revolutionizing the field of sensor technology. Finally, the fiber sensor is estimated to be incorporated with wireless communication and power devices, such as NFC, to enable portable operation.

References

(1) Tao, H.; Hwang, S.-W.; Marelli, B.; An, B.; Moreau, J. E.; Yang, M.; Brenckle, M. A.; Kim, S.; Kaplan, D. L.; Rogers, J. A. Silk-based resorbable electronic devices for remotely controlled therapy and in vivo infection abatement. *Proceedings of the National Academy of Sciences* **2014**, *111* (49), 17385-17389.

(2) Costa, P. D.; Rodrigues, P. P.; Reis, A. H.; Costa-Pereira, A. A Review on Remote Monitoring Technology Applied to Implantable Electronic Cardiovascular Devices. *Telemedicine Journal and E-Health* **2010**, *16* (10), 1042-1050.

(3) Bennett, T.; Kjellstrom, B.; Taepke, R.; Ryden, L.; Implantable, H. Development of implantable devices for continuous ambulatory monitoring of central hemodynamic values in heart failure patients. *Pace-Pacing and Clinical Electrophysiology* **2005**, *28* (6), 573-584.

(4) Tjulkins, F.; Nguyen, A. T. T.; Andreassen, E.; Hoff, L.; Grymyr, O. J.; Halvorsen, P. S.; Imenes, K. An Implantable Accelerometer-Based Heart-Monitoring Device With Improved Positional Stability. *Journal of Medical Devices-Transactions of the Asme* **2016**, *10* (4).

(5) Zeng, K.; Shi, X.; Tang, C.; Liu, T.; Peng, H. Design, fabrication and assembly considerations for electronic systems made of fibre devices. *Nature Reviews Materials* **2023**, *8* (8), 552-561, Article.

(6) Luo, Y.; Abidian, M. R.; Ahn, J.-H.; Akinwande, D.; Andrews, A. M.; Antonietti, M.; Bao, Z.; Berggren, M.; Berkey, C. A.; Bettinger, C. J.; et al. Technology Roadmap for Flexible Sensors. *ACS Nano* **2023**, *17* (6), 5211-5295.

(7) Uppada, V.; Gokara, M.; Rasineni, G. K. Diagnosis and therapy with CRISPR advanced CRISPR based tools for point of care diagnostics and early therapies. *Gene* **2018**, *656*, 22-29.

(8) Hall, N. C.; Povoski, S. P.; Murrey, D. A.; Knopp, M. V.; Martin, E. W. Bringing advanced medical imaging into the operative arena could revolutionize the surgical care of cancer patients. *Expert Review of Medical Devices* **2008**, *5* (6), 663-667.

(9) Ziegenfuß, T.; Zander, R. Understanding blood gas analysis. *Intensive Care Med* **2019**, *45* (11), 1684-1685.

(10) Day, T. K. Blood gas analysis. *Veterinary Clinics: Small Animal Practice* **2002**, *32* (5), 1031-1048.

(11) Rybak, D.; Su, Y.-C.; Li, Y.; Ding, B.; Lv, X.; Li, Z.; Yeh, Y.-C.; Nakielski, P.; Rinoldi, C.; Pierini, F. Evolution of nanostructured skin patches towards multifunctional wearable platforms for biomedical applications. *Nanoscale* **2023**, *15* (18), 8044-8083.

(12) Lu, D.; Li, S.; Yang, Q.; Arafa, H. M.; Xu, Y.; Yan, Y.; Ostojich, D.; Bai, W.; Guo, H.; Wu, C.; et al. Implantable, wireless, self-fixing thermal sensors for continuous measurements of microvascular blood flow in flaps and organ grafts. *Biosensors and Bioelectronics* **2022**, *206*, 114145.

(13) Stein, P. D.; Goldhaber, S. Z.; Henry, J. W.; Miller, A. C. Arterial blood gas analysis in the assessment of suspected acute pulmonary embolism. *Chest* **1996**, *109* (1), 78-81.

(14) Karim, F.; Fakhruddin, A. N. M. Recent advances in the development of biosensor for phenol: A review. *Reviews in Environmental Science and Biotechnology* **2012**, *11* (3), 261-274, Review.

(15) SEVERINGHAUS, J. W.; ASTRUP, P.; MURRAY, J. F. Blood Gas Analysis and Critical Care Medicine. *American Journal of Respiratory and Critical Care Medicine* **1998**, *157* (4), S114-S122.

(16) Management of Life-Threatening Poliomyelitis: Copenhagen. 1952–1056, with a Survey of Autopsy Findings in 115 Cases. *Medical Journal of Australia* **1957**, *1*.

(17) Fiddian-Green, R. Gastric intramucosal pH, tissue oxygenation and acid-base balance. *BJA: British Journal of Anaesthesia* **1995**, *74* (5), 591-606.

(18) Gattinoni, L.; Pesenti, A.; Matthay, M. Understanding blood gas analysis. *Intensive Care Medicine* **2018**, *44* (1), 91-93.

(19) Gattinoni, L.; Pesenti, A.; Matthay, M. Understanding blood gas analysis. *Intensive Care Med* **2018**, *44* (1), 91-93.

(20) Boemke, W.; Krebs, M. O.; Rossaint, R. [Blood gas analysis]. *Anaesthesist* **2004**, *53* (5), 471-492; quiz 493-474. .

(21) Jordan, B.; Mitchell, C.; Anderson, A.; Farkas, N.; Batrla, R. The clinical and health economic value of clinical laboratory diagnostics. *Ejifcc* **2015**, *26* (1), 47.

(22) Allardet-Servent, J.; Lebsir, M.; Dubroca, C.; Fabrigoule, M.; Jordana, S.; Signouret, T.; Castanier, M.; Thomas, G.; Soundaravelou, R.; Lepidi, A. Point-of-care versus central laboratory measurements of hemoglobin, hematocrit, glucose, bicarbonate and electrolytes: a prospective observational study in critically ill patients. *PLoS One* **2017**, *12* (1), e0169593.

(23) Uyanik, M.; Sertoglu, E.; Kayadibi, H.; Tapan, S.; Serdar, M. A.; Bilgi, C.; Kurt, I. Comparison of blood gas, electrolyte and metabolite results measured with two different blood gas analyzers and a core laboratory analyzer. *Scandinavian journal of clinical and laboratory investigation* **2015**, *75* (2), 97-105.

(24) Leino, A.; Kurvinen, K. Interchangeability of blood gas, electrolyte and metabolite results measured with point-of-care, blood gas and core laboratory analyzers. *Clinical chemistry and laboratory medicine* **2011**, *49* (7), 1187-1191.

(25) Casagranda, I. Point-of-care testing in critical care: the clinician's point of view. *Clinical chemistry and laboratory medicine* **2010**, *48* (7), 931-934.

(26) Nichols, J. H. Management of point-of-care testing. *Blood Gas News* **1999**, *8* (2).

(27) Karon, B. S.; Scott, R.; Burritt, M. F.; Santrach, P. J. Comparison of lactate values between point-of-care and central laboratory analyzers. *American journal of clinical pathology* **2007**, *128* (1), 168-171.

(28) Mion, M. M.; Bragato, G.; Zaninotto, M.; Alessandroni, J.; Bernardini, S.; Plebani, M. Analytical performance evaluation of the new GEM® Premier™ 5000 analyzer in comparison to the GEM® Premier™ 4000 and the RapidPoint® 405 systems. *Clinica Chimica Acta* **2018**, *486*, 313-319.

(29) Prause, G.; Ratzenhofer-Comenda, B.; Smolle-Jüttner, F.; Heydar-Fadai, J.; Wildner, G.; Spernbauer, P.; Smolle, J.; Hetz, H. Comparison of lactate or BE during

out-of-hospital cardiac arrest to determine metabolic acidosis. *Resuscitation* **2001**, *51* (3), 297-300.

(30) Schober, P.; Bossers, S. M.; Koolwijk, J.; Terra, M.; Schwarte, L. A. Prehospital coagulation measurement by a portable blood analyzer in a helicopter emergency medical service (HEMS). *The American Journal of Emergency Medicine* **2021**, *46*, 137-140.

(31) Corral Torres, E.; Hernández-Tejedor, A.; Suárez Bustamante, R.; de Elías Hernández, R.; Casado Flórez, I.; San Juan Linares, A. Prognostic value of venous blood analysis at the start of CPR in non-traumatic out-of-hospital cardiac arrest: association with ROSC and the neurological outcome. *Critical Care* **2020**, *24*, 1-8.

(32) Harve-Rytsälä, H.; Ångerman, S.; Kirves, H.; Nurmi, J. Arterial and end-tidal carbon dioxide partial pressure difference during prehospital anaesthesia in critically ill patients. *Acta Anaesthesiologica Scandinavica* **2021**, *65* (4), 534-539.

(33) Nadim, G.; Laursen, C. B.; Pietersen, P. I.; Wittrock, D.; Sørensen, M. K.; Nielsen, L. B.; Rasmussen, C.-H.; Christensen, H. M.; Helmerik, S.; Jørgensen, G. Prehospital emergency medical technicians can perform ultrasonography and blood analysis in prehospital evaluation of patients with chronic obstructive pulmonary disease: a feasibility study. *BMC Health Services Research* **2021**, *21*, 1-12.

(34) Rief, M.; Eichinger, M.; Eichlseder, M.; Pichler, A.; Prause, G.; Bornemann-Cimenti, H.; Zajic, P. Utilization of Multi-Parameter Blood Gas Analysis in Prehospital Emergency Medicine—A Scoping Review. *The Journal of Emergency Medicine* **2024**.

(35) Rodger, M. A.; CARRIER, M.; Jones, G. N.; RASULI, P.; RAYMOND, F. O.; DJUNAEDI, H.; WELLS, P. S. Diagnostic value of arterial blood gas measurement in suspected pulmonary embolism. *American journal of respiratory and critical care medicine* **2000**, *162* (6), 2105-2108.

(36) Prause, G.; Hetz, H.; Doppler, R. Preclinical blood gas analysis. 1. The value of preclinical blood gas analysis. *Der Anaesthesist* **1998**, *47* (5), 400-405.

(37) Prasad, H.; Vempalli, N.; Agrawal, N.; Ajun, U.; Salam, A.; Subhra Datta, S.; Singhal, A.; Ranjan, N.; Shabeeba Sherin, P.; Sundareshan, G. Correlation and

agreement between arterial and venous blood gas analysis in patients with hypotension—an emergency department-based cross-sectional study. *International Journal of Emergency Medicine* **2023**, *16* (1), 18.

(38) Miller, R. D.; Eriksson, L. I.; Fleisher, L. A.; Wiener-Kronish, J. P.; Cohen, N. H.; Young, W. L. *Miller's anesthesia e-book*; Elsevier Health Sciences **2014**.

(39) Larkin, B. G.; Zimmanck, R. J. Interpreting Arterial Blood Gases Successfully. *Aorn j* **2015**, *102* (4), 343-354; quiz 355-347.

(40) Cowley, N. J.; Owen, A.; Bion, J. F. Interpreting arterial blood gas results. *Bmj* **2013**, *346*, f16.

(41) Eggins, B. Chemical Sensors and Biosensors John Wiley & Sons. Ltd **2002**.

(42) Eggins, B. R. *Chemical sensors and biosensors*; John Wiley & Sons **2008**.

(43) D'Orazio, P. Biosensors in clinical chemistry. *Clinica chimica acta* **2003**, *334* (1-2), 41-69.

(44) Schöning, M. J.; Poghossian, A. Recent advances in biologically sensitive field-effect transistors (BioFETs). *Analyst* **2002**, *127* (9), 1137-1151.

(45) Chaubey, A.; Malhotra, B. Mediated biosensors. *Biosensors and bioelectronics* **2002**, *17* (6-7), 441-456.

(46) Mirsky, V. M.; Riepl, M.; Wolfbeis, O. S. Capacitive monitoring of protein immobilization and antigen–antibody reactions on monomolecular alkylthiol films on gold electrodes. *Biosensors and Bioelectronics* **1997**, *12* (9-10), 977-989.

(47) Guiseppi-Elie, A.; Lingerfelt, L. Impedimetric detection of DNA hybridization: towards near-patient DNA diagnostics. *Immobilisation of DNA on Chips I* **2005**, 161-186.

(48) Mehrvar, M.; Abdi, M. Recent developments, characteristics, and potential applications of electrochemical biosensors. *Analytical sciences* **2004**, *20* (8), 1113-1126.

(49) Ali, M. B.; Korpan, Y.; Gonchar, M.; El'Skaya, A.; Maaref, M. A.; Jaffrezic-Renault, N.; Martelet, C. Formaldehyde assay by capacitance versus voltage and impedance measurements using bi-layer bio-recognition membrane. *Biosensors and Bioelectronics* **2006**, *22* (5), 575-581.

(50) Ronkainen, N. J.; Halsall, H. B.; Heineman, W. R. Electrochemical biosensors. *Chemical Society Reviews* **2010**, *39* (5), 1747-1763.

(51) Clark, L. C.; Lyons, C. Electrode systems for continuous monitoring in cardiovascular surgery. *Annals of the New York Academy of sciences* **1962**, *102* (1), 29-45.

(52) Qin, Y.; Howlader, M. M. R.; Deen, M. J.; Haddara, Y. M.; Selvaganapathy, P. R. Polymer integration for packaging of implantable sensors. *Sensors and Actuators B: Chemical* **2014**, *202*, 758-778.

(53) Blau, A.; Murr, A.; Wolff, S.; Sernagor, E.; Medini, P.; Iurilli, G.; Ziegler, C.; Benfenati, F. Flexible, all-polymer microelectrode arrays for the capture of cardiac and neuronal signals. *Biomaterials* **2011**, *32* (7), 1778-1786.

(54) Hwang, S.-W.; Tao, H.; Kim, D.-H.; Cheng, H.; Song, J.-K.; Rill, E.; Brenckle, M. A.; Panilaitis, B.; Won, S. M.; Kim, Y.-S. A physically transient form of silicon electronics. *Science* **2012**, *337* (6102), 1640-1644.

(55) Kochkodan, V.; Hilal, N. A comprehensive review on surface modified polymer membranes for biofouling mitigation. *Desalination* **2015**, *356*, 187-207.

(56) Bazaka, K.; Jacob, M. V. Implantable devices: issues and challenges. *Electronics* **2012**, *2* (1), 1-34.

(57) Vaddiraju, S.; Tomazos, I.; Burgess, D. J.; Jain, F. C.; Papadimitrakopoulos, F. Emerging synergy between nanotechnology and implantable biosensors: a review. *Biosensors and Bioelectronics* **2010**, *25* (7), 1553-1565.

(58) Jeerapan, I.; Poorahong, S. Review—Flexible and Stretchable Electrochemical Sensing Systems: Materials, Energy Sources, and Integrations. *Journal of The Electrochemical Society* **2020**, *167* (3), 037573.

(59) Clausen, I.; Glott, T. Development of Clinically Relevant Implantable Pressure Sensors: Perspectives and Challenges. *Sensors* **2014**, *14* (9), 17686-17702.

(60) Arshady, R. Polymeric biomaterials: chemistry, concepts, criteria. *Introduction to polymeric biomaterials: the polymeric biomaterials series. London: Citus Books* **2003**, 1-62.

(61) Schoen, F.; Anderson, J. Host response to biomaterials and their evaluation. *Biomaterials science: an introduction to materials in medicine, 2nd. San Diego: Elsevier* **2004**, 293-296.

(62) Morais, J. M.; Papadimitrakopoulos, F.; Burgess, D. J. Biomaterials/tissue interactions: possible solutions to overcome foreign body response. *The AAPS journal* **2010**, *12*, 188-196.

(63) Anderson, J. M. Biological responses to materials. *Annual review of materials research* **2001**, *31* (1), 81-110.

(64) Jenny, C.; Anderson, J. Adsorbed serum proteins responsible for surface dependent human macrophage behaviour. *J Biomed Mater* **2000**, *49* (4), 435-447.

(65) Keselowsky, B. G.; Bridges, A. W.; Burns, K. L.; Tate, C. C.; Babensee, J. E.; LaPlaca, M. C.; García, A. J. Role of plasma fibronectin in the foreign body response to biomaterials. *Biomaterials* **2007**, *28* (25), 3626-3631.

(66) Anderson, J. M.; Rodriguez, A.; Chang, D. T. Foreign body reaction to biomaterials. In *Seminars in immunology* **2008**; Elsevier: Vol. 20, pp 86-100.

(67) McNally, A. K.; Jones, J. A.; MacEwan, S. R.; Colton, E.; Anderson, J. M. Vitronectin is a critical protein adhesion substrate for IL-4-induced foreign body giant cell formation. *Journal of Biomedical Materials Research Part A: An Official Journal of The Society for Biomaterials, The Japanese Society for Biomaterials, and The Australian Society for Biomaterials and the Korean Society for Biomaterials* **2008**, *86* (2), 535-543.

(68) Haas, A. The phagosome: compartment with a license to kill. *Traffic* **2007**, *8* (4), 311-330.

(69) Song, E.; Ouyang, N.; Hörbelt, M.; Antus, B.; Wang, M.; Exton, M. S. Influence of alternatively and classically activated macrophages on fibrogenic activities of human fibroblasts. *Cellular immunology* **2000**, *204* (1), 19-28.

(70) Niu, Q.; Chen, J.; Fan, S.; Yao, X.; Gu, Y.; Hsiao, B. S.; Wei, H.; Zhang, Y. Silk nanoribbon films with enriched silk II structure and enhanced piezoelectricity for self-powered implantable and wearable devices. *Nano Today* **2024**, *56*, 102228.

(71) Li, J.; Mei, H.; Zheng, W.; Pan, P.; Sun, X. J.; Li, F.; Guo, F.; Zhou, H. M.; Ma, J. Y.; Xu, X. X.; et al. A novel hydrogen peroxide biosensor based on hemoglobin-collagen-CNTs composite nanofibers. *Colloids and Surfaces B: Biointerfaces* **2014**, *118*, 77-82.

(72) Sid, S.; Mor, R. S.; Kishore, A.; Sharanagat, V. S. Bio-sourced polymers as alternatives to conventional food packaging materials: A review. *Trends in Food Science & Technology* **2021**, *115*, 87-104.

(73) Pires, P. C.; Mascarenhas-Melo, F.; Pedrosa, K.; Lopes, D.; Lopes, J.; Macário-Soares, A.; Peixoto, D.; Giram, P. S.; Veiga, F.; Paiva-Santos, A. C. Polymer-based biomaterials for pharmaceutical and biomedical applications: A focus on topical drug administration. *European Polymer Journal* **2023**, *187*, 111868.

(74) Davachi, S. M.; Kaffashi, B. Polylactic acid in medicine. *Polymer-Plastics Technology and Engineering* **2015**, *54* (9), 944-967.

(75) Dulay, S.; Rivas, L.; Miserere, S.; Pla, L.; Berdún, S.; Parra, J.; Eixarch, E.; Gratacós, E.; Illa, M.; Mir, M.; et al. in vivo Monitoring with micro-implantable hypoxia sensor based on tissue acidosis. *Talanta* **2021**, *226*, 122045.

(76) Pattanayak, I.; Alex, Y.; Mohanty, S. Advancing strategies towards the development of tissue engineering scaffolds: a review. *Journal of Materials Science* **2023**, *58* (32), 12847-12898.

(77) Fu, S.; Zhang, P. Surface modification of polylactic acid (PLA) and polyglycolic acid (PGA) monofilaments via the cold plasma method for acupoint catgut-embedding therapy applications. *Textile research journal* **2019**, *89* (18), 3839-3849.

(78) Núñez, E.; Ferrando, C.; Malmström, E.; Claesson, H.; Werner, P.-E.; Gedde, U. Crystal structure, melting behaviour and equilibrium melting point of star polyesters with crystallisable poly (ε-caprolactone) arms. *Polymer* **2004**, *45* (15), 5251-5263.

(79) Bartnikowski, M.; Dargaville, T. R.; Ivanovski, S.; Hutmacher, D. W. Degradation mechanisms of polycaprolactone in the context of chemistry, geometry and environment. *Progress in Polymer Science* **2019**, *96*, 1-20.

(80) Agarwal, S.; Speyerer, C. Degradable blends of semi-crystalline and amorphous branched poly (caprolactone): Effect of microstructure on blend properties. *Polymer* **2010**, *51* (5), 1024-1032.

(81) Blanquer, S.; Garric, X.; Coudane, J. PCL-Isocyanate: A New, Degradable Macromolecular Synthon for the Synthesis of Polymeric Bioconjugates. *Macromolecular Chemistry and Physics* **2009**, *210* (20), 1691-1696.

(82) Kováčová, M.; Vykydalová, A.; Špitálský, Z. Polycaprolactone with glass beads for 3D printing filaments. *Processes* **2023**, *11* (2), 395.

(83) Zavřel, F.; Novák, M.; Kroupová, J.; Beveridge, C.; Štěpánek, F.; Ruphuy, G. Development of Hot-Melt Extrusion Method to Produce Hydroxyapatite/Polycaprolactone Composite Filaments. *Advanced Engineering Materials* **2022**, *24* (3), 2100820.

(84) Kim, H.-S.; Yang, S. M.; Jang, T.-M.; Oh, N.; Kim, H.-S.; Hwang, S.-W. Bioresorbable Silicon Nanomembranes and Iron Catalyst Nanoparticles for Flexible, Transient Electrochemical Dopamine Monitors. *Advanced Healthcare Materials* **2018**, *7* (24), 1801071.

(85) Steinbüchel, A. Non-biodegradable biopolymers from renewable resources: perspectives and impacts. *Current opinion in biotechnology* **2005**, *16* (6), 607-613.

(86) Lin, Q. Synthetic Non-Biodegradable Polymers. In *Introduction to Biomaterials*, World Scientific **2006**; pp 172-186.

(87) Herbert, R.; Elsisy, M.; Rigo, B.; Lim, H.-R.; Kim, H.; Choi, C.; Kim, S.; Ye, S.-H.; Wagner, W. R.; Chun, Y.; et al. Fully implantable batteryless soft platforms with printed nanomaterial-based arterial stiffness sensors for wireless continuous monitoring of restenosis in real time. *Nano Today* **2022**, *46*, 101557.

(88) Xu, S.; Xie, L.; Yu, X.; Xiong, Y.; Tang, H. Synthesis and characterization of phenyl polysiloxane modified polyurea/polyurethanes. *Journal of Polymer Science Part A: Polymer Chemistry* **2015**, *53* (15), 1794-1805.

(89) Hao, X.; Jeffery, J. L.; Le, T. P.; McFarland, G.; Johnson, G.; Mulder, R. J.; Garrett, Q.; Manns, F.; Nankivil, D.; Arrieta, E. High refractive index polysiloxane as injectable, in situ curable accommodating intraocular lens. *Biomaterials* **2012**, *33* (23), 5659-5671.

(90) Furukawa, N.; Yuasa, M.; Yamada, Y.; Kimura, Y. Synthesis and properties of novel thermosetting polysiloxane-block-polyimides with vinyl functionality. *Polymer* **1998**, *39* (13), 2941-2949.

(91) Zhou, S.; Ding, X.; Wu, L. Fabrication of ambient-curable superhydrophobic fluoropolysiloxane/TiO2 nanocomposite coatings with good mechanical properties and durability. *Progress in organic coatings* **2013**, *76* (4), 563-570.

(92) Ardhaoui, M.; Naciri, M.; Mullen, T.; Brugha, C.; Keenan, A. K.; Al-Rubeai, M.; Dowling, D. P. Evaluation of cell behaviour on atmospheric plasma deposited siloxane and fluorosiloxane coatings. *Journal of Adhesion Science and Technology* **2010**, *24* (5), 889-903.

(93) Sharma, S.; Sudhakara, P.; Singh, J.; Mr, S.; Siengchin, S. Fabrication of novel polymer composites from leather waste fibers and recycled poly (ethylene-vinyl-acetate) for value-added products. *Sustainability* **2023**, *15* (5), 4333.

(94) Major, I.; Lastakchi, S.; Dalton, M.; McConville, C. Implantable drug delivery systems. In *Engineering Drug Delivery Systems*, Elsevier **2020**; pp 111-146.

(95) Wen, X.-W.; Pei, S.-P.; Li, H.; Ai, F.; Chen, H.; Li, K.-Y.; Wang, Q.; Zhang, Y.-M. Study on an antifouling and blood compatible poly (ethylene–vinyl acetate) material with fluorinated surface structure. *Journal of materials science* **2010**, *45*, 2788-2797.

(96) Teoh, G.; Klanrit, P.; Kasimatis, M.; Seifalian, A. in development of artificial organs. *Minerva medica* **2015**, *106*, 17-33.

(97) Duran, M. M.; Moro, G.; Zhang, Y.; Islam, A. 3D printing of silicone and polyurethane elastomers for medical device application: A review. *Advances in Industrial and Manufacturing Engineering* **2023**, 100125.

(98) Elsner, J. J.; McKeon, B. P. Orthopedic application of polycarbonate urethanes: a review. *Techniques in Orthopaedics* **2017**, *32* (3), 132-140.

(99) Cherng, J. Y.; Hou, T. Y.; Shih, M. F.; Talsma, H.; Hennink, W. E. Polyurethane-based drug delivery systems. *International journal of pharmaceutics* **2013**, *450* (1-2), 145-162.

(100) Gostev, A. A.; Karpenko, A. A.; Laktionov, P. P. Polyurethanes in cardiovascular prosthetics. *Polymer Bulletin* **2018**, *75*, 4311-4325.

(101) Fathi-Karkan, S.; Banimohamad-Shotorbani, B.; Saghati, S.; Rahbarghazi, R.; Davaran, S. A critical review of fibrous polyurethane-based vascular tissue engineering scaffolds. *Journal of Biological Engineering* **2022**, *16* (1), 6.

(102) Yu, B.; Long, N.; Moussy, Y.; Moussy, F. A long-term flexible minimally-invasive implantable glucose biosensor based on an epoxy-enhanced polyurethane membrane. *Biosensors and Bioelectronics* **2006**, *21* (12), 2275-2282.

(103) Hwa, K.-Y.; Subramani, B. Immobilization of glucose oxidase on gold surface for applications in implantable biosensors. *Journal of Medical and Bioengineering Vol* **2015**, *4* (4).

(104) Cordeiro, C.; Sias, A.; Koster, T.; Westerink, B.; Cremers, T. In vivo "real-time" monitoring of glucose in the brain with an amperometric enzyme-based biosensor based on gold coated tungsten (W-Au) microelectrodes. *Sensors and Actuators B: Chemical* **2018**, *263*, 605-613.

(105) Wassum, K. M.; Tolosa, V. M.; Wang, J.; Walker, E.; Monbouquette, H. G.; Maidment, N. T. Silicon wafer-based platinum microelectrode array biosensor for near real-time measurement of glutamate in vivo. *Sensors* **2008**, *8* (8), 5023-5036.

(106) Lin, L.; Xue, R.; Nie, S. Surface-enhanced Raman scattering (SERS) nanoparticles for biodiagnostics, bioimaging, and spectroscopy-guided cancer surgery. In *Encyclopedia of Nanomaterials (First Edition)*, Yin, Y., Lu, Y., Xia, Y. Eds.; Elsevier **2023**; pp 340-355.

(107) Maddocks, G. M.; Daniele, M. A. Chemical Sensors: Wearable Sensors. In *Encyclopedia of Sensors and Biosensors (First Edition)*, Narayan, R. Ed.; Elsevier **2023**; pp 260-280.

(108) Bollella, P.; Sharma, S.; Cass, A. E. G.; Tasca, F.; Antiochia, R. Minimally Invasive Glucose Monitoring Using a Highly Porous Gold Microneedles-Based Biosensor: Characterization and Application in Artificial Interstitial Fluid. *Catalysts* **2019**, *9* (7), 580.

(109) Bollella, P.; Sharma, S.; Cass, A. E.; Tasca, F.; Antiochia, R. Minimally invasive glucose monitoring using a highly porous gold microneedles-based biosensor: Characterization and application in artificial interstitial fluid. *Catalysts* **2019**, *9* (7), 580.

(110) Brunette, D. M.; Tengvall, P.; Textor, M.; Thomsen, P.; Ratner, B. D. A perspective on titanium biocompatibility. *Titanium in Medicine: material science, surface science, engineering, biological responses and medical applications* **2001**, 1-12.

(111) Bidaux, J.-E.; Closuit, C.; Rodriguez-Arbaizar, M.; Zufferey, D.; Carreno-Morelli, E. Metal injection moulding of low modulus Ti–Nb alloys for biomedical applications. *Powder Metallurgy* **2013**, *56* (4), 263-266.

(112) Quinn, R. K.; Armstrong, N. R. Electrochemical and surface analytical characterization of titanium and titanium hydride thin film electrode oxidation. *Journal of the Electrochemical Society* **1978**, *125* (11), 1790.

(113) Green, R. B.; Topsakal, E. Biocompatible Antennas for Implantable Biosensor Systems. In *2019 International Workshop on Antenna Technology (iWAT)* **2019**; pp 70-72.

(114) Ahamed, M.; AlSalhi, M. S.; Siddiqui, M. Silver nanoparticle applications and human health. *Clinica chimica acta* **2010**, *411* (23-24), 1841-1848.

(115) Huang, H.; Lai, W.; Cui, M.; Liang, L.; Lin, Y.; Fang, Q.; Liu, Y.; Xie, L. An Evaluation of Blood Compatibility of Silver Nanoparticles. *Scientific Reports* **2016**, *6* (1), 25518.

(116) Herbert, R.; Mishra, S.; Lim, H.-R.; Yoo, H.; Yeo, W.-H. Fully Printed, Wireless, Stretchable Implantable Biosystem toward Batteryless, Real-Time Monitoring of Cerebral Aneurysm Hemodynamics. *Advanced Science* **2019**, *6* (18), 1901034.

(117) Yang, Q.; Atanasov, P.; Wilkins, E. A novel amperometric transducer design for needle-type implantable biosensor applications. *Electroanalysis* **1997**, *9* (16), 1252-1256.

(118) Matusiewicz, H.; Richter, M. Local release of metal ions from endovascular metallic implants in the human biological specimens: An overview of in vivo clinical implications. *World Journal of Advanced Research and Reviews* **2021**, *11* (1), 091-102.

(119) Barhoum, A.; Sadak, O.; Ramirez, I. A.; Iverson, N. Stimuli-bioresponsive hydrogels as new generation materials for implantable, wearable, and disposable biosensors for medical diagnostics: Principles, opportunities, and challenges. *Advances in Colloid and Interface Science* **2023**, *317*, 102920.

(120) Zhang, M.; Wang, X.; Huang, Z.; Rao, W. Liquid Metal Based Flexible and Implantable Biosensors. *Biosensors* **2020**, *10* (11), 170.

(121) Chen, S.; Wang, H.-Z.; Zhao, R.-Q.; Rao, W.; Liu, J. Liquid metal composites. *Matter* **2020**, *2* (6), 1446-1480.

(122) Zhang, M.; Yao, S.; Rao, W.; Liu, J. Transformable soft liquid metal micro/nanomaterials. *Materials Science and Engineering: R: Reports* **2019**, *138*, 1-35.

(123) Chen, S.; Zhao, R.; Sun, X.; Wang, H.; Li, L.; Liu, J. Toxicity and biocompatibility of liquid metals. *Advanced Healthcare Materials* **2023**, *12* (3), 2201924.

(124) Liu, F.; Yu, Y.; Yi, L.; Liu, J. Liquid metal as reconnection agent for peripheral nerve injury. *Science bulletin* **2016**, *61*, 939-947.

(125) Yi, L.; Jin, C.; Wang, L.; Liu, J. Liquid-solid phase transition alloy as reversible and rapid molding bone cement. *Biomaterials* **2014**, *35* (37), 9789-9801.

(126) Dickey, M. D. Stretchable and Soft Electronics using Liquid Metals. *Advanced Materials* **2017**, *29* (27), 1606425.

(127) Zhuang, Q.; Yao, K.; Wu, M.; Lei, Z.; Chen, F.; Li, J.; Mei, Q.; Zhou, Y.; Huang, Q.; Zhao, X.; et al. Wafer-patterned, permeable, and stretchable liquid metal microelectrodes for implantable bioelectronics with chronic biocompatibility. *Science Advances* **2023**, *9* (22), eadg8602.

(128) Eivazzadeh-Keihan, R.; Bahojb Noruzi, E.; Chidar, E.; Jafari, M.; Davoodi, F.; Kashtiaray, A.; Ghafori Gorab, M.; Masoud Hashemi, S.; Javanshir, S.; Ahangari Cohan, R.; et al. Applications of carbon-based conductive nanomaterials in biosensors. *Chemical Engineering Journal* **2022**, *442*, 136183.

(129) Pashazadeh-Panahi, P.; Hasanzadeh, M.; Eivazzadeh-Keihan, R. A novel optical probe based on d-penicillamine-functionalized graphene quantum dots: Preparation and application as signal amplification element to minoring of ions in human biofluid. *Journal of Molecular Recognition* **2020**, *33* (5), e2828.

(130) Wu, Z.; Wang, Y.; Liu, X.; Lv, C.; Li, Y.; Wei, D.; Liu, Z. Carbon-nanomaterial-based flexible batteries for wearable electronics. *Advanced materials* **2019**, *31* (9), 1800716.

(131) Eivazzadeh-Keihan, R.; Maleki, A.; De La Guardia, M.; Bani, M. S.; Chenab, K. K.; Pashazadeh-Panahi, P.; Baradaran, B.; Mokhtarzadeh, A.; Hamblin, M. R. Carbon based nanomaterials for tissue engineering of bone: Building new bone on small black scaffolds: A review. *Journal of advanced research* **2019**, *18*, 185-201.

(132) Liu, Z.; Robinson, J. T.; Tabakman, S. M.; Yang, K.; Dai, H. Carbon materials for drug delivery & cancer therapy. *Materials today* **2011**, *14* (7-8), 316-323.

(133) Mwakikunga, B. W.; Hillie, K. T. Graphene synthesis, catalysis with transition metals and their interactions by laser photolysis. InTech **2011**.

(134) Li, Z.; Liu, Z.; Sun, H.; Gao, C. Superstructured Assembly of Nanocarbons: Fullerenes, Nanotubes, and Graphene. *Chemical Reviews* **2015**, *115* (15), 7046-7117.

(135) Balandin, A. A. Thermal properties of graphene and nanostructured carbon materials. *Nature materials* **2011**, *10* (8), 569-581.

(136) Yang, H.; Xue, T.; Li, F.; Liu, W.; Song, Y. Graphene: diversified flexible 2D material for wearable vital signs monitoring. *Advanced Materials Technologies* **2019**, *4* (2), 1800574.

(137) Lee, C.; Wei, X.; Kysar, J. W.; Hone, J. Measurement of the elastic properties and intrinsic strength of monolayer graphene. *science* **2008**, *321* (5887), 385-388.

(138) Weiss, N. O.; Zhou, H.; Liao, L.; Liu, Y.; Jiang, S.; Huang, Y.; Duan, X. Graphene: an emerging electronic material. *Advanced materials* **2012**, *24* (43), 5782-5825.

(139) Inoue, N.; Koya, Y.; Miki, N.; Onoe, H. Graphene-Based Wireless Tube-Shaped Pressure Sensor for In Vivo Blood Pressure Monitoring. *Micromachines* **2019**, *10* (2), 139.

(140) de Menezes, B. R. C.; Rodrigues, K. F.; da Silva Fonseca, B. C.; Ribas, R. G.; do Amaral Montanheiro, T. L.; Thim, G. P. Recent advances in the use of carbon nanotubes as smart biomaterials. *Journal of Materials Chemistry B* **2019**, *7* (9), 1343-1360.

(141) Peigney, A.; Laurent, C.; Flahaut, E.; Bacsa, R.; Rousset, A. Specific surface area of carbon nanotubes and bundles of carbon nanotubes. *Carbon* **2001**, *39* (4), 507-514.

(142) Yun, Y.; Dong, Z.; Shanov, V.; Heineman, W. R.; Halsall, H. B.; Bhattacharya, A.; Conforti, L.; Narayan, R. K.; Ball, W. S.; Schulz, M. J. Nanotube electrodes and biosensors. *Nano Today* **2007**, *2* (6), 30-37.

(143) Chen, M.; Qin, X.; Zeng, G. Biodegradation of Carbon Nanotubes, Graphene, and Their Derivatives. *Trends Biotechnol* **2017**, *35* (9), 836-846.

(144) Wang, L.; Xie, S.; Wang, Z.; Liu, F.; Yang, Y.; Tang, C.; Wu, X.; Liu, P.; Li, Y.; Saiyin, H.; et al. Functionalized helical fibre bundles of carbon nanotubes as electrochemical sensors for long-term in vivo monitoring of multiple disease biomarkers. *Nature Biomedical Engineering* **2020**, *4* (2), 159-171.

(145) Luong, J. H. T.; Mulchandani, A.; Guilbault, G. G. Developments and applications of biosensors. *Trends in Biotechnology* **1988**, *6* (12), 310-316.

(146) Newman, J. D.; Turner, A. P. F. Home blood glucose biosensors: a commercial perspective. *Biosensors and Bioelectronics* **2005**, *20* (12), 2435-2453.

(147) Kissinger, P. T. Biosensors—a perspective. *Biosensors and Bioelectronics* **2005**, *20* (12), 2512-2516.

(148) Cheng, N.; Du, D.; Wang, X.; Liu, D.; Xu, W.; Luo, Y.; Lin, Y. Recent Advances in Biosensors for Detecting Cancer-Derived Exosomes. *Trends in Biotechnology* **2019**, *37* (11), 1236-1254, Review.

(149) Pisoschi, A. Potentiometric Biosensors: Concept and Analytical Applications-An Editorial. *Biochemistry & Analytical Biochemistry* **2016**, *5*.

(150) Karunakaran, R.; Keskin, M. Chapter 11 - Biosensors: components, mechanisms, and applications. In *Analytical Techniques in Biosciences*, Egbuna, C., Patrick-Iwuanyanwu, K. C., Shah, M. A., Ifemeje, J. C., Rasul, A. Eds.; Academic Press **2022**; pp 179-190.

(151) Rodrigues, D.; Barbosa, A. I.; Rebelo, R.; Kwon, I. K.; Reis, R. L.; Correlo, V. M. Skin-integrated wearable systems and implantable biosensors: A comprehensive review. *Biosensors* **2020**, *10* (7), Review.

(152) Fang, Y.; Feng, J.; Shi, X.; Yang, Y.; Wang, J.; Sun, X.; Li, W.; Sun, X.; Peng, H. Coaxial fiber organic electrochemical transistor with high transconductance. *Nano Research* **2023**, *16* (9), 11885-11892, Article.

(153) Paradiso, R.; Caldani, L.; Pacelli, M. Knitted Electronic Textiles. In *Wearable Sensors: Fundamentals, Implementation and Applications* **2014**; pp 153-174.

(154) Wu, X.; Feng, J.; Deng, J.; Cui, Z.; Wang, L.; Xie, S.; Chen, C.; Tang, C.; Han, Z.; Yu, H.; et al. Fiber-shaped organic electrochemical transistors for biochemical detections with high sensitivity and stability. *Science China Chemistry* **2020**, *63* (9), 1281-1288.

(155) Yaqoob, A. A.; Ibrahim, M. N. M.; Rodríguez-Couto, S. Development and modification of materials to build cost-effective anodes for microbial fuel cells (MFCs): An overview. *Biochemical Engineering Journal* **2020**, *164*, 107779.

(156) Xie, M.; Yao, G.; Gan, X.; Zhang, C.; Zhang, T.; Wang, Q.; Li, X.; Zhou, C.; Zhao, K.; Gao, M.; et al. Non-Enzyme, Temperature Calibrating, and Bioactive Fiber-based Flexible Sensors for Dopamine and Lactic Acid Detection. *Advanced Fiber Materials* **2024**, *6* (2), 501-511.

(157) Rohani Shirvan, A.; Nouri, A.; Sutti, A. A perspective on the wet spinning process and its advancements in biomedical sciences. *European Polymer Journal* **2022**, *181*, Review.

(158) Gao, Q.; Chen, Z.; Liu, C.; Wang, Y.; Zhu, J.; Gao, C. Helical TPU/Ag@K2Ti4O9 fibers with shape memory performance for highly stretchable and sensitive strain sensors. *Journal of Alloys and Compounds* **2024**, *980*, 173547.

(159) Chen, X.; Wang, J.; Zhang, J.; Lin, H.; Tian, M.; Li, M.; Tian, Y. Development and application of electrospun fiber-based multifunctional sensors. *Chemical Engineering Journal* **2024**, *486*, Review.

(160) Wang, S.; Xiao, J.; Liu, H.; Zhang, L. Silk nanofibrous iontronic sensors for accurate blood pressure monitoring. *Chemical Engineering Journal* **2023**, *453*, 139815.

(161) Saerens, L.; Vervaet, C.; Remon, J. P.; De Beer, T. Process monitoring and visualization solutions for hot-melt extrusion: A review. *Journal of Pharmacy and Pharmacology* **2014**, *66* (2), 180-203, Review.

(162) Nguyen, H.; Kaas, A.; Kinnunen, P.; Carvelli, V.; Monticelli, C.; Yliniemi, J.; Illikainen, M. Fiber reinforced alkali-activated stone wool composites fabricated by hot-pressing technique. *Materials and Design* **2020**, *186*, Article.

(163) Zhu, S.; So, J.-H.; Mays, R.; Desai, S.; Barnes, W. R.; Pourdeyhimi, B.; Dickey, M. D. Ultrastretchable Fibers with Metallic Conductivity Using a Liquid Metal Alloy Core. *Advanced Functional Materials* **2013**, *23* (18), 2308-2314.

(164) Wardak, C.; Pietrzak, K.; Morawska, K.; Grabarczyk, M. Ion-Selective Electrodes with Solid Contact Based on Composite Materials: A Review. *Sensors* **2023**, *23* (13), 5839.

(165) Wang, H.; Li, R.; Cao, Y.; Chen, S.; Yuan, B.; Zhu, X.; Cheng, J.; Duan, M.; Liu, J. Liquid Metal Fibers. *Advanced Fiber Materials* **2022**, *4* (5), 987-1004.

(166) Dong, C.; Leber, A.; Das Gupta, T.; Chandran, R.; Volpi, M.; Qu, Y.; Nguyen-Dang, T.; Bartolomei, N.; Yan, W.; Sorin, F. High-efficiency super-elastic liquid metal based triboelectric fibers and textiles. *Nature Communications* **2020**, *11* (1), 3537.

(167) Yu, X.; Fan, W.; Liu, Y.; Dong, K.; Wang, S.; Chen, W.; Zhang, Y.; Lu, L.; Liu, H.; Zhang, Y. A One-Step Fabricated Sheath-Core Stretchable Fiber Based on Liquid Metal with Superior Electric Conductivity for Wearable Sensors and Heaters. *Advanced Materials Technologies* **2022**, *7* (7), 2101618.

(168) Mohd Radzuan, N. A.; Sulong, A. B.; Sahari, J. A review of electrical conductivity models for conductive polymer composite. *International Journal of Hydrogen Energy* **2017**, *42* (14), 9262-9273.

(169) Sun, G.; Zhou, J.; Yu, F.; Zhang, Y.; Pang, J. H. L.; Zheng, L. Electrochemical capacitive properties of CNT fibers spun from vertically aligned CNT arrays. *Journal of Solid State Electrochemistry* **2012**, *16* (5), 1775-1780.

(170) Chen, Y.; Meng, F.; Li, M.; Liu, J. Novel capacitive sensor: Fabrication from carbon nanotube arrays and sensing property characterization. *Sensors and Actuators B: Chemical* **2009**, *140* (2), 396-401.

(171) Vanamo, U.; Hupa, E.; Yrjänä, V.; Bobacka, J. New Signal Readout Principle for Solid-Contact Ion-Selective Electrodes. *Analytical Chemistry* **2016**, *88* (8), 4369-4374.

(172) Jalal, N. R.; Madrakian, T.; Ahmadi, M.; Afkhami, A.; Khalili, S.; Bahrami, M.; Roshanaei, M. Wireless wearable potentiometric sensor for simultaneous determination of pH, sodium and potassium in human sweat. *Scientific Reports* **2024**, *14* (1), 11526.

(173) Sempionatto, J. R.; Martin, A.; García-Carmona, L.; Barfidokht, A.; Kurniawan, J. F.; Moreto, J. R.; Tang, G.; Shin, A.; Liu, X.; Escarpa, A.; et al. Skin-worn Soft Microfluidic Potentiometric Detection System. *Electroanalysis* **2019**, *31* (2), 239-245.

(174) Peng, T.; Sui, Z.; Huang, Z.; Xie, J.; Wen, K.; Zhang, Y.; Huang, W.; Mi, W.; Peng, K.; Dai, X.; et al. Point-of-care test system for detection of immunoglobulin-G and -M against nucleocapsid protein and spike glycoprotein of SARS-CoV-2. *Sens Actuators B Chem* **2021**, *331*, 129415.

(175) Yin, L.; Cao, M.; Kim, K. N.; Lin, M.; Moon, J.-M.; Sempionatto, J. R.; Yu, J.; Liu, R.; Wicker, C.; Trifonov, A.; et al. A stretchable epidermal sweat sensing platform with an integrated printed battery and electrochromic display. *Nature Electronics* **2022**, *5* (10), 694-705.

(176) Zhai, Q.; Yap, L. W.; Wang, R.; Gong, S.; Guo, Z.; Liu, Y.; Lyu, Q.; Wang, J.; Simon, G. P.; Cheng, W. Vertically Aligned Gold Nanowires as Stretchable and Wearable Epidermal Ion-Selective Electrode for Noninvasive Multiplexed Sweat Analysis. *Anal Chem* **2020**, *92* (6), 4647-4655.

(177) Roy, S.; David-Pur, M.; Hanein, Y. Carbon Nanotube-Based Ion Selective Sensors for Wearable Applications. *ACS Appl Mater Interfaces* **2017**, *9* (40), 35169-35177.

(178) Parrilla, M.; Ferré, J.; Guinovart, T.; Andrade, F. J. Wearable Potentiometric Sensors Based on Commercial Carbon Fibres for Monitoring Sodium in Sweat. *Electroanalysis* **2016**, *28* (6), 1267-1275.

(179) Xu, J.; Zhang, Z.; Gan, S.; Gao, H.; Kong, H.; Song, Z.; Ge, X.; Bao, Y.; Niu, L. Highly Stretchable Fiber-Based Potentiometric Ion Sensors for Multichannel Real-Time Analysis of Human Sweat. *ACS Sensors* **2020**, *5* (9), 2834-2842.

(180) Zhao, Y.; Zhai, Q.; Dong, D.; An, T.; Gong, S.; Shi, Q.; Cheng, W. Highly Stretchable and Strain-Insensitive Fiber-Based Wearable Electrochemical Biosensor to Monitor Glucose in the Sweat. *Analytical Chemistry* **2019**, *91* (10), 6569-6576.

(181) Mo, L.; Ma, X.; Fan, L.; Xin, J. H.; Yu, H. Weavable, large-scaled, rapid response, long-term stable electrochemical fabric sensor integrated into clothing for monitoring potassium ions in sweat. *Chemical Engineering Journal* **2023**, *454*, 140473.

(182) Wang, L.; Wang, L.; Zhang, Y.; Pan, J.; Li, S.; Sun, X.; Zhang, B.; Peng, H. Weaving Sensing Fibers into Electrochemical Fabric for Real-Time Health Monitoring. *Advanced Functional Materials* **2018**, *28* (42), 1804456.

(183) Wang, L.; Lu, J.; Li, Q.; Li, L.; He, E.; Jiao, Y.; Ye, T.; Zhang, Y. A Core–Sheath Sensing Yarn-Based Electrochemical Fabric System for Powerful Sweat Capture and Stable Sensing. *Advanced Functional Materials* **2022**, *32* (23), 2200922.

(184) Rostampour, M.; Lawrence Jr, D. J.; Hamid, Z.; Darensbourg, J.; Calvo-Marzal, P.; Chumbimuni-Torres, K. Y. Highly Reproducible Flexible Ion-selective Electrodes for the Detection of Sodium and Potassium in Artificial Sweat. *Electroanalysis* **2023**, *35* (3), e202200121.

(185) Shu, Y.; Su, T.; Lu, Q.; Shang, Z.; Xu, Q.; Hu, X. Highly Stretchable Wearable Electrochemical Sensor Based on Ni-Co MOF Nanosheet-Decorated Ag/rGO/PU Fiber for Continuous Sweat Glucose Detection. *Anal Chem* **2021**, *93* (48), 16222-16230.